

Biochemical and spectroscopic insights into peculiar active site structures and biosynthesis of O₂-tolerant [NiFe]-hydrogenases

vorgelegt von

M. Sc. Anne-Christine Schulz

an der Fakultät II – Mathematik und Naturwissenschaften
der Technischen Universität Berlin zur Erlangung des akademischen
Grades

Doktor der Naturwissenschaften

- Dr.rer.nat. -

genehmigte Dissertation

Promotionsausschuss:

Vorsitzender: Prof. Dr. Martin Lerch

Gutachter: Prof. Dr. Gary Sawers

Gutachter: Prof. Dr. Peter Hildebrandt

Gutachter: Dr. Oliver Lenz

Tag der wissenschaftlichen Aussprache: 23. November 2020

Berlin 2021

Publications

Schulz, A-C; Frielingsdorf, S; Pommerening, P; Lauterbach, L; Bistoni, G; Neese, F; Oestreich M.; Lenz O; (2020): Formyltetrahydrofolate decarbonylase synthesizes the active site CO ligand of O₂-tolerant [NiFe] hydrogenase. In *J Am Chem Soc* 142 (3), pp. 1457–1464. DOI: 10.1021/jacs.9b11506.

Kulka, C J; Schulz, A-C; Lorent, C; Wahlefeld, S; Schulz, C; Wiemann, C; Wrathall, S L D; Procacci, B; Greetham, G M; Stein, M; Lauterbach, L; Hunt, N T; Lenz, O; Horch, M; Zebger, I; (expected 2020): Deciphering the role of the bidentate glutamate coordination in the active site of the [NiFe] hydrogenase from *Hydrogenophilus thermoluteolus*. *In preparation*

First author

Acknowledgments

The work presented in this thesis could not have been carried out without the support of the following people to whom I want to express my thanks.

First of all, I would like to thank Dr. Oliver Lenz and Dr. Stefan Frielingsdorf for the supervision and support and the possibility to work on the maturation of [NiFe]-hydrogenases.

I thank all co-investigators which contributed to this work in particular:

Catharina Kulka, Charlotte Wiemann, Dr. Giorgio Caserta, Dr. Ingo Zebger and Prof. Dr. Peter Hildebrandt for all the spectroscopy included in this thesis. Prof. Dr. Holger Dobbek and Dr. Berta Martins for the possibility to perform crystallization trials. Dr. Phillip Pommerening for the help with the stinky synthesis of formyl-CoA and Prof. Dr. Martin Oestreich for providing access to his lab. Jasmin Kutzke and Prof. Dr. Silke Leimkühler for metal quantification and Siad Wolff and Prof. Dr. Christian Limberg who provided the synthetic Fe complex.

I want also to thank the whole MVL group and especially the AG Lenz for the nice atmosphere and many cold beers at Schleusenkrug.

The biggest thank goes to Giorgio, my family in Eisenach, and my Marburger family, who are always there for me.

Abstract

[NiFe]-hydrogenases are metalloenzymes catalyzing the reversible cleavage of H₂ into two H⁺ and two e⁻. They are particularly interesting for clean and sustainable H₂-based energy conversion approaches or the H₂-driven regeneration of nucleotide cofactors. Their active site consists of a NiFe(CN)₂(CO) moiety coordinated to the protein by four strictly conserved cysteine residues. Two of them serve as terminal ligands to the Ni and two are bridging ligands coordinating both, the Ni and Fe. The Fe is additionally equipped with one carbon monoxide (CO) and two cyanide (CN⁻) ligands. The maturation of the NiFe(CN)₂(CO) active site involves at least six auxiliary proteins, namely HypA-F. A seventh Hyp protein, HypX, is required for aerobic CO ligand biosynthesis. Although, the biosynthesis of [NiFe]-hydrogenases has been studied extensively, many details of their maturation still remain elusive.

Because of its O₂-tolerance and thermostability, the soluble, NAD⁺-reducing [NiFe]-hydrogenases from *Hydrogenophilus thermoluteolus* (HtSH) is of special biotechnological interest. Previous studies unveiled unusual structural and spectroscopic properties of the oxidized enzyme. Here, we present evidence by protein biochemistry in combination with infrared spectroscopy that the peculiar active site structure is causative for the unusual spectroscopic properties and probably related to a novel O₂ protection mechanism.

The second part of this thesis focused on the maturation of [NiFe]-hydrogenases, especially the assembly of the Fe(CN)₂(CO) moiety. Therefore, purified HypCD was biochemically and spectroscopically investigated and apo-HypCD was used in *in vitro* maturation experiments. The preliminary results presented here, help to address open questions regarding the Fe(CN)₂(CO) moiety assembly process, the order of ligand attachment as well as the coordination and characterization of the Fe(CN)₂(CO) moiety and its transfer to the hydrogenase apo-large subunit.

Furthermore, a comprehensive biochemical characterization of HypX revealed detailed insight into the mechanism of aerobic CO ligand synthesis. In the proposed mechanism, the formyl group of N¹⁰-formyl-THF is first transferred to Coenzyme A (CoA) producing formyl-CoA, which, in the second step, becomes decarbonylated to form CoA and CO.

Zusammenfassung

[NiFe]-Hydrogenasen sind Metalloenzyme, welche die reversible Umwandlung von H_2 in zwei H^+ und zwei e^- katalysieren. Dies macht sie besonders interessant für saubere und nachhaltige H_2 -basierte Energieumwandlungsansätze oder die H_2 -getriebene Regeneration von Nukleotid-Cofaktoren. Ihr aktives Zentrum besteht aus einem $NiFe(CN)_2(CO)$ Cofaktor, der über vier strikt konservierte Cysteinreste an das Protein koordiniert ist. Zwei von ihnen dienen als terminale Liganden des Ni und die anderen beiden sind verbrückende Liganden, die sowohl das Ni als auch das Fe koordinieren. Das Fe ist zusätzlich mit einem Kohlenstoffmonoxid- (CO) und zwei Cyanid-Liganden ausgestattet. An der Reifung des $NiFe(CN)_2(CO)$ Zentrums sind mindestens sechs Hilfsproteine beteiligt, die Proteine HypA-F. Ein siebtes Hyp-Protein, HypX, wird für die aerobe Synthese des CO Liganden benötigt. Obwohl die Reifung der [NiFe]-Hydrogenasen intensiv untersucht wird, sind viele Details noch nicht bekannt.

Aufgrund ihrer O_2 -Toleranz und ihrer Thermostabilität ist die lösliche, NAD^+ -reduzierende [NiFe]-Hydrogenase aus *Hydrogenophilus thermoluteolus* (HtSH) von besonderem biotechnologischen Interesse. Frühere Studien zeigten ungewöhnliche strukturelle und spektroskopische Eigenschaften des oxidierten Enzyms. Hier präsentieren wir Beweise dafür, dass sowohl die ungewöhnliche Struktur des aktiven Zentrums als auch das beispiellose spektroskopische Merkmal demselben Zustand entsprechen, der einen neuartigen O_2 -Schutzmechanismus darstellen könnte.

Der zweite Teil der Arbeit befasste sich mit der Reifung der [NiFe]-Hydrogenasen, insbesondere mit der Assemblierung der $Fe(CN)_2(CO)$ Einheit. Hierfür wurde gereinigtes HypCD biochemisch und spektroskopisch untersucht und apo-HypCD wurde für *in vitro* Maturationsversuche verwendet. Die hier gezeigten vorläufigen Ergebnisse helfen bei der Beantwortung offener Fragen bezüglich des Mechanismus und der Reihenfolge der Ligandenbindung, der Koordination und Charakterisierung des Vorläufer-Fe und der $Fe(CN)_2(CO)$ Einheit und dessen Transfer in die große Untereinheit der Hydrogenase.

Darüber hinaus ergab eine umfassende biochemische Charakterisierung von HypX detaillierte Einblicke in den Mechanismus der aeroben CO-Ligandensynthese. Bei dem vorgeschlagenen Mechanismus wird die Formylgruppe von N^{10} -Formyl-THF zuerst auf Coenzym A (CoA) übertragen, wodurch Formyl-CoA erzeugt wird, das in einem zweiten Schritt unter Bildung von CoA und CO decarboxyliert wird.

Table of Contents

Abbreviation	5
1. Introduction.....	9
1.1. [NiFe]-hydrogenases.....	10
1.1.1. Classification.....	10
1.1.2. Active site	11
1.1.3. Catalytic cycle.....	11
1.1.4. Substrate and product transport	14
1.1.5. NAD ⁺ -reducing soluble hydrogenase from <i>H. thermoluteolus</i>	15
1.2. Maturation of [NiFe]-hydrogenases.....	18
1.2.1. HypCD serves as scaffold for the Fe(CN) ₂ (CO) synthesis	20
1.2.2. Cyanide ligand synthesis and transfer.....	23
1.2.3. HypX – CO ligand synthesis under aerobic conditions	25
1.3. Aim of the study.....	26
2. Materials and Methods.....	29
2.1. Strains, plasmids, and oligonucleotides	29
2.2. Bacterial cultivation conditions	33
2.2.1. <i>R. eutropha</i>	33
2.2.2. <i>E. coli</i>	35
2.2.3. Conservation of bacterial strains	36
2.3. Polymerase chain reaction (PCR)	36
2.4. Determination of DNA concentrations	36
2.5. Agarose gel electrophoresis	36
2.6. Restriction of DNA	37
2.7. Dephosphorylation and Phosphorylation of DNA fragments	37
2.8. Ligation of DNA fragments	37
2.9. Gibson assembly	38

2.10.	Site-directed mutagenesis	38
2.11.	DNA sequencing	39
2.12.	Plasmid preparation	39
2.13.	Plasmid transfer	39
2.13.1.	Preparation of competent cells	39
2.13.2.	Transformation	40
2.13.3.	Conjugation	40
2.14.	Protein purification	41
2.14.1.	HypX	41
2.14.2.	<i>HtSH</i>	42
2.14.3.	HypCD	43
2.14.4.	HypE and HypF	43
2.15.	Determination of protein concentrations	44
2.16.	SDS-PAGE	44
2.17.	Coomassie staining	45
2.18.	Western blot	45
2.19.	Metal determination	46
2.20.	Determination of HypX activity	47
2.21.	Determination of <i>HtSH</i> activity	47
2.22.	Chemical synthesis of formyl-CoA	48
2.23.	Quantification of CoA and formyl-CoA	49
2.24.	Fourier-transform infrared spectroscopy (FTIR)	50
2.25.	Resonance Raman Spectroscopy	50
2.26.	UV-Vis spectroscopy	50
2.27.	Crystallization trials with Strep- <i>HtHypX</i>	51
2.28.	Cleavage of MBP- <i>HtHypX</i> fusion protein with factor Xa	51
2.29.	Determination of ATPase activity of HypE, HypF and HypCD	51
2.30.	Reconstitution of HypCD with (PPh ₄)[Fe(CO) ₂ (CN) ₂ (μ-pdt)K] complex	52

2.31.	Reconstitution of HypCD with Fe	53
2.32.	Chemical <i>in vitro</i> assembly of the Fe(CN) ₂ (CO) moiety with KCN and CO.....	53
3.	Results	55
3.1.	<i>HtSH</i> – a thermostable NAD ⁺ -reducing [NiFe]-hydrogenase from <i>H. thermoluteolus</i>	55
3.1.1.	The oxidized active site species at 1993 cm ⁻¹ accumulates upon O ₂ exposure .	56
3.1.2.	The CO stretching frequency at 1993 cm ⁻¹ reflects an active site configuration with Glu32 coordinating the Ni	58
3.2.	HypCD – the central scaffold for Fe(CN) ₂ (CO) moiety assembly	63
3.2.1.	Spectroscopic characterization of <i>E. coli</i> HypCD.....	63
3.2.2.	ATPase activity of HypCD	71
3.2.3.	Chemical maturation of HypCD	73
3.2.3.1.	Reconstitution of apo-HypCD with Fe.....	73
3.2.3.2.	Treatment of apo-HypCD(Fe) with KCN and CO gas	73
3.2.3.3.	Reconstitution of apo-HypCD with a chemical mimic of the Fe(CN) ₂ (CO) complex	78
3.2.4.	Enzymatic <i>in vitro</i> assembly of the Fe(CN) ₂ (CO) moiety	79
3.2.4.1.	Purification of functional active HypE and HypF	80
3.2.5.	Transfer of the Fe(CN) ₂ (CO) moiety to the [NiFe]-hydrogenase large subunit	84
3.3.	HypX synthesizes the active site CO ligand in O ₂ -tolerant [NiFe]-hydrogenases	86
3.3.1.	MBP-HypX is functional <i>in vivo</i>	86
3.3.2.	MBP-HypX produces CO <i>in vitro</i>	87
3.3.3.	Coenzyme A is required for HypX activity and HypX stabilization	91
3.3.4.	Formyl-CoA is a reaction intermediate	92
3.3.5.	Glu449 is essential for HypX activity	93
3.3.6.	Thermostable HypX from <i>H. thermoluteolus</i> (<i>HtHypX</i>).....	96
4.	Discussion	107
4.1.	<i>HtSH</i> – a thermostable NAD ⁺ -reducing [NiFe]-hydrogenase	107

4.1.1.	The CO stretching vibration at 1993 cm^{-1} corresponds to an active site structure with the Glu32 carboxyl group coordinating the Ni	107
4.1.2.	The Ni-Glu configuration might represent a novel O_2 protection mechanism	108
4.2.	Synthesis of the $\text{Fe}(\text{CN})_2(\text{CO})$ moiety	111
4.2.1.	HypCD - the scaffold for $\text{Fe}(\text{CN})_2(\text{CO})$ moiety synthesis	112
4.2.1.1.	Chemical maturation of apo-HypCD as a tool to investigate the $\text{Fe}(\text{CN})_2(\text{CO})$ moiety	112
4.2.1.2.	Transfer of the $\text{Fe}(\text{CN})_2(\text{CO})$ moiety.....	114
4.2.1.3.	The recently discovered ATPase activity is independent of the $\text{Fe}(\text{CN})_2(\text{CO})$ moiety and seems to depend on reducing purification conditions	115
4.2.2.	HypX catalyzes the aerobic CO ligand synthesis.....	115
5.	References.....	121
6.	Table of Tables.....	135
7.	Table of Figures	137
8.	Appendix.....	139

Abbreviation

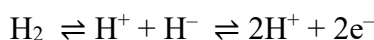
E°'	redox potential relative to standard hydrogen electrode
μ	micro (10 ⁻⁶)
4'-PP	4'-phosphopantetheine
A	Ampere
AC	affinity chromatography
ADP	adenosine diphosphate
AMP	adenosine monophosphate
APS	ammonium peroxodisulfate
ATP	adenosine triphosphate
bp	base pairs
BSA	bovine serum albumin
BV	bed volumes
CCD	charge coupled device
CIP	alkaline Phosphatase, Calf Intestinal
cm	centimeter (10 ⁻²)
CoA	coenzyme A
CP	carbamoyl phosphate
Da	Dalton
deoxyHb	deoxyhemoglobin
DMSO	dimethyl sulfoxide
DNA	deoxyribonucleic acid
dNTPs	deoxyribose nucleoside triphosphate
DTNB	5,5'-dithiobis-(2-nitrobenzoic acid)
DTT	dithiothreitol
EDTA	ethylenediaminetetraacetic acid
EPR	electron paramagnetic resonance
F	Faraday
FDH	<i>N</i> ¹⁰ -formyl-THF dehydrogenases
FGN	fructose-glycerol minimal medium
FMN	flavin mononucleotide
FN	fructose minimal medium

FTIR	Fourier-transform infrared spectroscopy
FTR	ferredoxin:thioredoxin reductase
g	gram
GMP	guanosine monophosphate
h	hour
HbCO	carboxyhemoglobin
ICP-OES	inductively coupled plasma optical emission spectrometry
IPTG	isopropyl β -d-1-thiogalactopyranoside
IR	infrared
ITC	isothermal titration calorimetry
K	Kelvin
LB	lysogeny broth
LDH	lactate dehydrogenase
m	milli (10^{-3})
M	molar (mol/L)
MBH	membrane-bound hydrogenase
MBP	maltose binding protein
MCT	mercury cadmium telluride
min	minute
MOPS	3-(<i>N</i> -morpholino)propanesulfonic acid
n	nano (10^{-9})
NAD/NADH	nicotinamide adenine dinucleotide
NADP/NADPH	nicotinamide adenine dinucleotide phosphate
NaDT	sodium dithionite
NB	nutrient broth
Ni-NTA	Ni-nitrilotriacetic acid
NMR	nuclear magnetic resonance
NRVS	nuclear resonance vibrational spectroscopy
OD	optical density
PAGE	polyacrylamide gel electrophoresis
PCR	polymerase chain reaction
PEG	polyethylene glycol
PEP	phosphoenyl pyruvate
PK	pyruvate kinase

PP _i	pyrophosphate
RH	regulatory hydrogenase
Rpm	rounds per minute
RR	resonance Raman
s	second
SAM	<i>S</i> -adenosyl methionine
SDS	sodium dodecyl sulfate
SEC	size-exclusion chromatography
SH	soluble hydrogenase
SOC	super optimal broth with catabolite repression
TCA	trichloroacetic acid
TCEP	tris(2-carboxyethyl)phosphine
TEMED	tetramethylethylenediamine
TGYEP	tryptone, yeast extract, glucose, KPO ₄ buffer
THF	tetrahydrofolate
TNB ⁻	2-nitro-5-thiobenzoate
U	Unit (μmol/min)
UV	ultraviolet
V	volt
Vis	visible
W	Watt
x g	g-force

1. Introduction

Hydrogenases are a diverse group of biotechnologically relevant metalloenzymes catalyzing the reversible cleavage of molecular hydrogen into two protons and two electrons according to the following reaction:



H_2 production and H_2 consumption processes catalyzed by hydrogenases play a key role in the global hydrogen cycle and are intimately linked to nitrogen and carbon cycles (Schwartz et al. 2013). Hydrogenases are found in a wide variety of microorganisms, including archaea and bacteria and some lower eukaryotes (Vignais and Billoud 2007; Vignais et al. 2001; Tamagnini et al. 2002; Thauer et al. 2010; Tamagnini et al. 2007). Their primary functions are to generate cellular energy by H_2 oxidation or to dispose excess reducing equivalents by H_2 production. According to their metal content in the active site, they are grouped into the three phylogenetically unrelated classes of [Fe]-, [FeFe]- and [NiFe]-hydrogenases. Interestingly, the function of all three enzymes does not rely on just the metal atoms embedded in a protein shell. They require unprecedented, diatomic, Fe ligands for catalysis. The mono-iron site of [Fe]-hydrogenase is equipped with two carbon monoxide (CO) ligands, while the di-iron site of [FeFe]-hydrogenases carries three CO and two cyanide (CN^-) groups. The active site Fe of [NiFe]-hydrogenases also ligates two CN^- ligands but only one CO ligand. All three active sites have an open coordination site at which binding and activation of H_2 take place (**Figure 1**) (Lubitz et al. 2014; Böck et al. 2006).

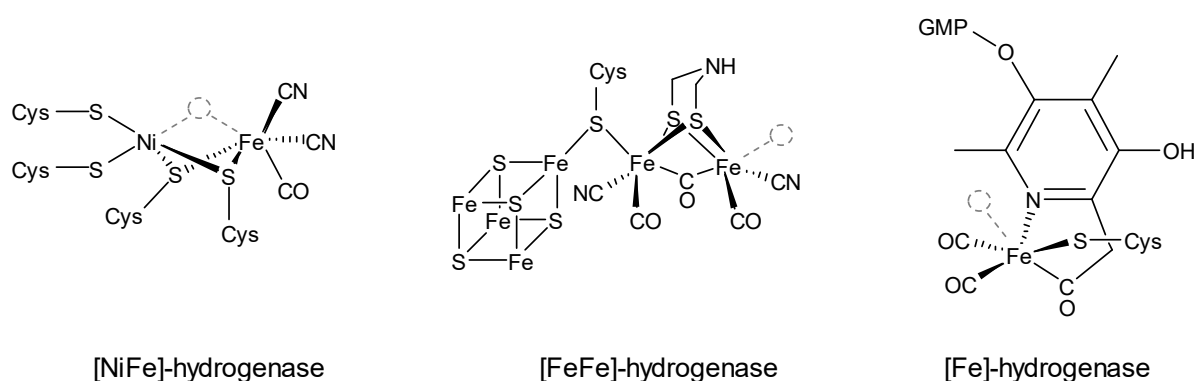


Figure 1. Schematic representation of the active sites of [NiFe]-, [FeFe]- and [Fe]-hydrogenase. The dashed circle indicates the open coordination site. GMP stands for guanosine monophosphate.

While hydrogenases of the [Fe] and [FeFe] class are synthesized exclusively under strictly anoxic conditions, several [NiFe]-hydrogenases are synthesized under oxic conditions and, moreover, are able to sustain H₂ oxidation activity in the presence of O₂ (Cammack et al. 2001).

1.1. [NiFe]-hydrogenases

1.1.1. Classification

The class of [NiFe]-hydrogenases is further divided into four groups depending on the phylogeny, biochemical characteristics, function and cellular localization of the enzyme (Vignais and Billoud 2007; Constant et al. 2011; Greening et al. 2015).

Group 1 contains membrane-associated H₂ uptake hydrogenases. These membrane-bound hydrogenases (MBH) are attached to either the cytoplasmic or the periplasmic side of the cytoplasmic membrane. They are linked to the quinone pool of the respiratory chain via specific electron-acceptors (e.g. cytochrome *b*) anchored in the membrane. Electrons derived from the oxidation of H₂ are used to generate a proton-motive force to produce energy. Terminal electron acceptors can be, e.g., CO₂, SO₄²⁻, NO₃⁻, Fe(III) oxides, and O₂ (Vignais and Billoud 2007; Lukey et al. 2010; Pandelia et al. 2012; Laurinavichene and Tsygankov 2001).

Group 2 contains cytoplasmic hydrogenases and is sub-divided into two subgroups. Group 2a includes, among others, cyanobacterial uptake hydrogenases that oxidize H₂ endogenously produced by N₂ fixation. Group 2b contains H₂-sensing regulatory hydrogenases (RHs). They regulate the gene expression of energy-conserving hydrogenases in response to the availability of H₂.

Group 3 comprises bidirectional heteromultimeric cytoplasmic hydrogenases. Hydrogenases of this group possess, in addition to the heterodimeric hydrogenase module (see below), further subunits able to bind cofactors, such as F₄₂₀, NAD⁺ or NADP⁺. Group 3 hydrogenases are further divided into four subgroups: group 3a – F₄₂₀-reducing hydrogenases, group 3b – bifunctional (NADPH-coupled) hydrogenases, group 3c – methyl-viologen-reducing hydrogenases, group 3d – bidirectional NAD(P)-linked hydrogenases. Hydrogenases of group 3d consist of the heterodimeric hydrogenase module and a NAD(P)⁺-reductase module that binds NAD(P)⁺/NAD(P)H. They couple H₂ oxidation or proton reduction with the reduction of NAD(P)⁺ or oxidation of NAD(P)H, respectively. One recently characterized member of this

group, which was used in this study, is the NAD⁺-reducing soluble [NiFe]-hydrogenase from *Hydrogenophilus thermoluteolus* TH-1 (*HtSH*) (Preissler et al. 2018b; Shomura et al. 2017).

Membrane-bound, H₂-evolving hydrogenases make up the group 4 of [NiFe]-hydrogenases. They display a complex architecture and reduce protons to dispose reducing equivalents generated by the anaerobic oxidation of C₁ compounds, such as CO or formate.

1.1.2. Active site

[NiFe]-hydrogenases are modular enzymes with a catalytic hydrogenase module comprising a large subunit, hosting the bimetallic active site, and a small subunit, harboring one or more FeS clusters. The architecture of the active site is almost identical among [NiFe]-hydrogenases (Lubitz et al. 2014). The catalytic center is deeply buried in the large subunit and coordinated to the protein via four invariant cysteine residues. Two of them serve as terminal ligands coordinating the Ni ion and two are bridging ligands coordinating both the Ni and the Fe ion. A third coordination site in the bridging position between Ni and Fe serves as substrate binding site. The Fe ion is additionally equipped with one CO and two CN⁻ ligands (**Figure 1**). They stabilize the Fe ion in a low-spin Fe(II) state (Kubas 2007) and presumably facilitate the activation of H₂ at the Ni ion (Bruschi et al. 2014). The presence of the CO and CN⁻ ligands was first revealed by IR spectroscopic studies (Happe et al. 1997; Bagley et al. 1995; Pierik et al. 1999; Bagley et al. 1994; Volbeda et al. 1996).

1.1.3. Catalytic cycle

During H₂ conversion, the active site passes through several intermediate states. They mainly differ by the nature of the third bridging ligand and the oxidation state of the Ni ion while the Fe ion maintains the Fe(II) oxidation state throughout the catalytic cycle. Furthermore, the protein matrix shows no significant conformational changes, which is in accord with a high turnover frequency. To understand the mechanism of [NiFe]-hydrogenases it is important to gain detailed information about the intermediate states. The investigation of these intermediate states via X-ray crystallography is very challenging due to the difficulty to detect hydrogen species. However, they can be observed using spectroscopic methods, such as infrared (IR) and electron paramagnetic resonance (EPR) spectroscopy.

Introduction

EPR spectroscopy can be used to detect the FeS clusters of [NiFe]-hydrogenases as well as the bimetallic active site. However, only paramagnetic states are EPR-active and give a signal. During catalysis, the Fe ion remains in an EPR-silent, low-spin Fe(II) state, whereas the Ni ion changes between EPR-active (paramagnetic) and EPR-silent (diamagnetic) states. The oxidation states Ni(I) and Ni(III) are EPR-active, Ni(II) is EPR-silent.

In addition to EPR, IR spectroscopy plays a central role in the characterization of the NiFe active site. It is used to monitor the stretching vibrations of the CO and CN⁻ ligands, which appear in an otherwise featureless region of the IR spectrum of proteins. Signals in the range of 2040 – 2100 cm⁻¹ correspond to CN⁻ ligands and signals in the range of 1900 – 1970 cm⁻¹ typically correspond to CO ligands. The frequencies of these bands are very sensitive to redox changes and therefore can be used to determine the intermediate state of the active site.

Introduction

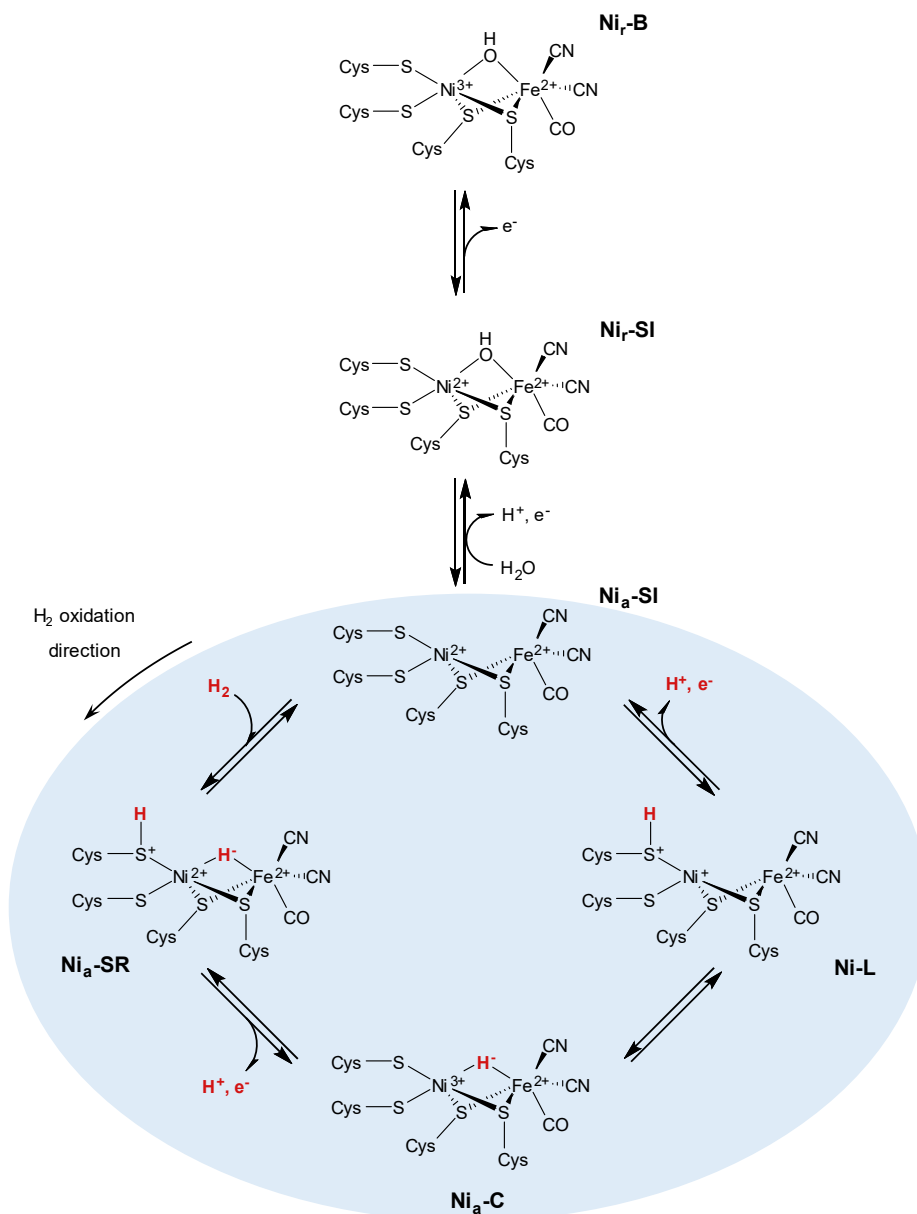


Figure 2. Catalytic cycle of [NiFe]-hydrogenases. Highlighted in blue are the proposed intermediate states of the catalytic cycle. Additionally, two inactive states, Ni_r-SI and Ni_r-B are shown.

A scheme of the currently proposed catalytic cycle of [NiFe]-hydrogenases is shown in **Figure 2**. Concerning the direction of H₂ oxidation, the cycle starts with the Ni_a-SI state in which a bridging position between Ni and Fe is vacant. This state is proposed to bind the substrate H₂. Cleavage of H₂ leads to the Ni_a-SR state with a hydride (H⁻) in the bridging position and a protonated (H⁺) sulfur of a terminal cysteine ligand. Both, the bridging H⁻ and the protonated cysteine have been identified in the crystal structure of the [NiFe]-hydrogenase of *Desulfovibrio vulgaris* Miyazaki at 0.89 Å resolution (Ogata et al. 2015b). The bridging H⁻ was also observed by nuclear resonance vibrational spectroscopy (NRVS) (Ogata et al. 2015a).

Introduction

Removal of one H^+ and one e^- leads to the oxidation to Ni(III) in the EPR-active Ni_a-C state, while the H^- remains as bridging ligand. H^+ and e^- rearrangements lead to the conversion of Ni_a-C to Ni_a-L . In the Ni_a-L state, Ni is reduced to the EPR-active Ni(I), and the H^- is oxidized to a H^+ which becomes attached to the terminal cysteine, as recently verified by Fourier transform infrared (FTIR) spectroscopy (Tai et al. 2019). Subsequent removal of one H^+ and one e^- leads then to the formation of Ni_a-SI (Fig. 2).

Beside the catalytically active states, there are three prominent inactive states, named Ni_u-A , Ni_r-B and Ni_r-SI , which are observed under oxidizing conditions. In the Ni_r-SI state, an OH^- ligand occupies the bridging position, and Ni resides in the Ni(II) state. The Ni_u-A and Ni_r-B harbor a Ni(III) species and are therefore detectable by EPR spectroscopy. Although hydrogenases in the “resting” states are catalytically inactive, they be reactivated by chemical reduction or reduction with H_2 , resulting in the formation of the Ni_a-SI state. Activation of the Ni_u-A state requires longer activation times, whereas the Ni_r-B and Ni_r-SI states are activated within seconds. Furthermore, the Ni_u-A state is usually absent in O_2 -tolerant [NiFe]-hydrogenases (Pandelia et al. 2010; Saggiu et al. 2009; Saggiu et al. 2010; Guiral M. et al. 2006).

1.1.4. Substrate and product transport

The oxidation of H_2 leads to the production of two H^+ and two e^- , which need to be transferred to the protein surface via dedicated pathways. The substrate, H_2 , is transported to the active site through hydrophobic gas channels. Several gas channels leading to the active site have been identified experimentally with xenon-, krypton- and oxygen-derivatized structures (Fontecilla-Camps et al. 2009; Montet et al. 1997; Kalms et al. 2018; Kalms et al. 2016). Electron transfer is facilitated by a chain of FeS clusters with inter-cluster distances of approximately 12 Å (Lubitz et al. 2014). The proton transfer pathway has not been fully elucidated yet. Several conserved amino acid residues are discussed as primary proton acceptors: a terminal cysteine of the Ni in addition to a nearby glutamate residue (Cys-Glu pathway), and an arginine in the canopy region of the active site (Arg pathway). Site-specific exchanges of the glutamate as well as the arginine residue resulted in substantially diminished or completely abolished catalytic activity (Dementin et al. 2004; Adamson et al. 2017b; Evans et al. 2016; Evans et al. 2018; Greene et al. 2016; Gebler et al. 2007). In the proposed Cys-Glu pathway, the protons are further transferred from the glutamate to the protein surface through a chain of glutamate

residues (Galván et al. 2008; Teixeira et al. 2008). The proposed Arg pathway leads to the protein surface via a histidine-rich motif (Szóri-Dorogházi et al. 2012).

1.1.5. NAD⁺-reducing soluble hydrogenase from *H. thermoluteolus*

Hydrogenophilus thermoluteolus TH-1 is an aerobic, facultative chemolithoautotrophic, H₂-oxidizing β -proteobacterium (Hayashi et al. 1999). It is moderate thermophilic with optimal chemolithoautotrophic growth at a temperature of 52 °C (Goto et al. 1978). It possesses an O₂-tolerant NAD⁺-reducing soluble hydrogenase (*HtSH*), which catalyzes the reversible electron transfer from H₂ to NAD⁺ producing NADH and two H⁺ (Preissler et al. 2018b). Because of its O₂-tolerance and thermostability the *HtSH* is an attractive candidate for H₂-driven NAD(P)H cofactor regeneration in biotechnological applications (Lauterbach et al. 2013). It is composed of four subunits, HoxFUYH, which form two catalytic units – a hydrogenase unit and a NAD⁺ reductase unit (**Figure 3**). The hydrogenase unit consists of the large subunit HoxH, carrying the NiFe active site and the small subunit HoxY harboring one [4Fe-4S] cluster. The NAD⁺ reductase unit consists of HoxU which harbors one [2Fe-2S] and two [4Fe-4S] clusters and HoxF carrying one [4Fe-4S] cluster and the NAD⁺ reductase active site with one flavin mononucleotide (FMN) molecule. The hydrogenase unit catalyzes the reversible cleavage of H₂ into two H⁺ and two e⁻, while the NAD⁺ reductase module catalyzes the reversible conversion of NAD⁺ into NADH. Electron transfer between the two active sites is mediated by the five FeS clusters.

Introduction

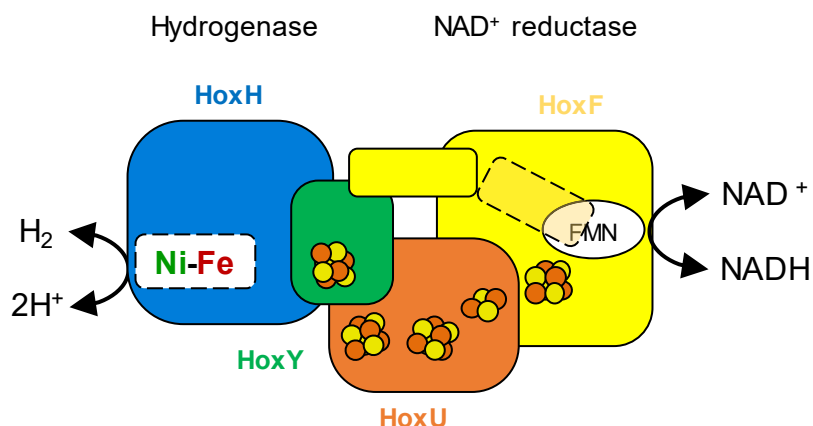


Figure 3. Subunit and cofactor composition of *HtSH*. HoxH and HoxY form the hydrogenase module, HoxF and HoxU form the NAD⁺ reductase module. The large hydrogenase subunit HoxH harbors the NiFe active site. HoxF harbors the FMN-based NAD(H)-binding site. Both catalytic sites are connected via a chain of FeS clusters. The C-terminal region of HoxF (small yellow box) changes between an oxidized and a reduced conformation. In the oxidized conformation it reaches to the NAD⁺/NADH binding site (dotted line), in the reduced conformation it aligns with the HoxY subunit (bold line).

Recent IR and EPR spectroscopic analysis of *HtSH* lead to the assignment of the catalytically active Ni_a-SR, Ni_a-C and Ni_a-SI states. Under oxidizing conditions, three different active site states have been observed, two of them correspond to the Ni_r-SI and Ni_r-B-like states, which are EPR-silent. The third oxidized state could not be assigned to any known state. The IR signal of this state exhibits an extremely high CO stretching vibration at 1993 cm⁻¹ (**Figure 4**). Such a high CO stretching frequency has not been observed for any other [NiFe]-hydrogenase so far and may reflect an unusual active site configuration (Preissler et al. 2018b).

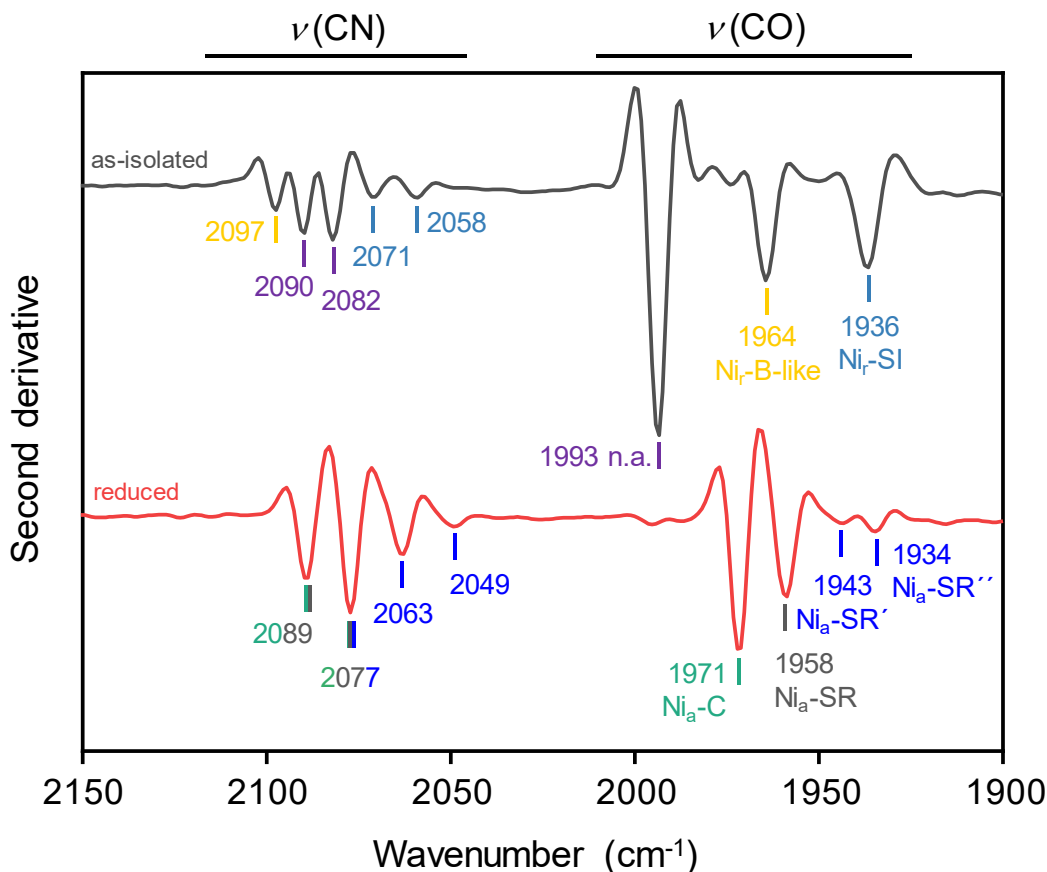


Figure 4. IR spectra of *HtSH* recorded under different redox conditions. The spectrum of as-isolated *HtSH* under oxidizing conditions is shown in gray, the spectrum of *HtSH* reduced with TCEP, NADH and H₂ is shown in red. The different active site states are color-coded as follows: Ni_r-SI = light blue, Ni_r-B-like = yellow, not assigned (n.a.) = purple, Ni_a-SR = grey, Ni_a-SR' and Ni_a-SR'' = blue, Ni_a-C = green. Overlapping peaks are labeled in multiple colors corresponding to the represented states.

The crystal structure of *HtSH* isolated from its native host has been published in the air-oxidized and H₂-reduced states (Shomura et al. 2017). The oxidized structure of the NiFe active site reveals an unprecedented coordination geometry (**Figure 5**). The Ni ion is six-coordinated by three bridging cysteines, one terminal cysteine and the carboxyl group of Glu32 serving as bidentate ligand. In the reduced state, the NiFe active site shows the standard conformation with two bridging cysteines and two terminal cysteines (Shomura et al. 2017).

Besides the NiFe active site, differences in the overall structure of the oxidized and the reduced state were observed. In the oxidized state, the very C-terminal end of HoxF gets into contact with the NAD⁺/NADH binding site of HoxF. Upon reduction with H₂, the C-terminal region flips over to the HoxY subunit (**Figure 3**) and FMN appears to dissociate.

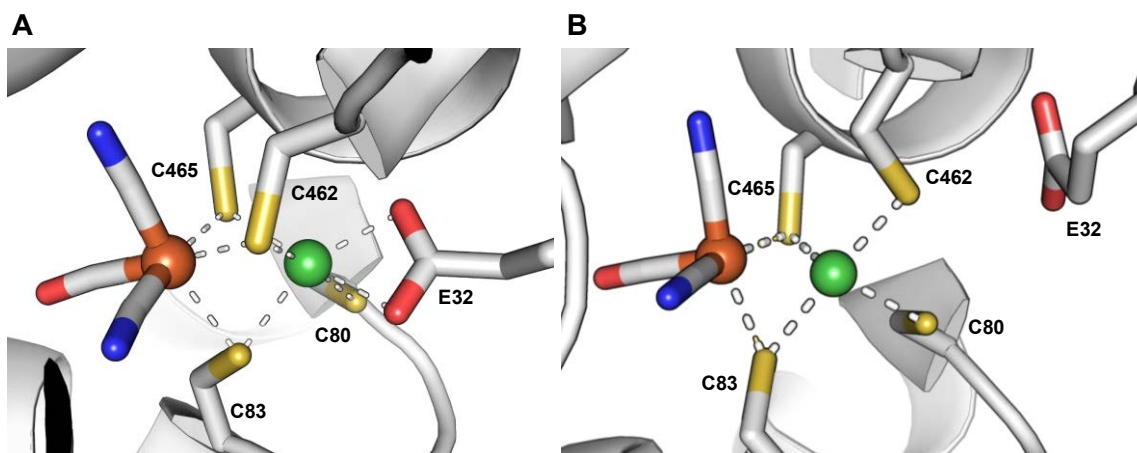


Figure 5. Structure of the NiFe active site of *HtSH*. (A) Oxidized state at 2.58 Å resolution (PDB: 5XF9), (B) H₂-reduced state at 2.70 Å resolution (PDB: 5XFA). The coordinating cysteine residues and the Glu32 residue are shown as stick models. Iron and nickel are depicted by orange and green spheres, respectively. Dotted lines represent the ligand bonding between the metals and the amino acid residues.

1.2. Maturation of [NiFe]-hydrogenases

Biosynthesis of [NiFe]-hydrogenases including the assembly of the NiFe(CN)₂(CO) moiety is a complex process that requires a sophisticated maturation machinery involving at least six auxiliary proteins, named HypA-F (Böck et al. 2006). According to the current model (**Figure 6**) (Böck et al. 2006; Forzi et al. 2007; Watanabe et al. 2012b), a complex of HypC and HypD serves as scaffold for the assembly of the Fe(CN)₂(CO) moiety (Bürstel et al. 2012). The CN⁻ and CO ligands are proposed to be attached to a single Fe, which is jointly coordinated by both proteins. Because of their toxicity in living organisms, the biosynthesis of the CO and CN⁻ ligands is of particular interest. While crucial steps of the assembly of the catalytic center of [Fe]-hydrogenase have been elucidated, the origin of the CO ligands remains unknown (Bai et al. 2017). In the case of [FeFe]-hydrogenase, both CO and CN⁻ originate from tyrosine, which is converted by the maturase HydG into *p*-cresol and dehydroglycine in a radical-SAM reaction. Dehydroglycine is then decomposed into one CO and one CN⁻ ligand (Kuchenreuther et al. 2013). In [NiFe]-hydrogenases synthesis of the two CN⁻ ligands is catalyzed by the two maturases HypF and HypE using carbamoyl phosphate as substrate (Reissmann et al. 2003). The cyanide group is transferred from HypE to the Fe coordinated by HypCD. The pathway for anaerobic CO ligand synthesis remains unclear. However, under aerobic conditions an additional maturation protein, designated HypX, which occurs exclusively in microorganisms synthesizing [NiFe]-hydrogenases under oxic conditions is required for CO ligand synthesis (Buhrke and Friedrich 1998; Bürstel et al. 2016).

Introduction

Upon completion, the $\text{Fe}(\text{CN})_2(\text{CO})$ moiety is transferred from HypCD to the apo-form of the [NiFe]-hydrogenase large subunit (Bürstel et al. 2012; Stripp et al. 2013). Subsequently, the Ni ion is incorporated in a process that is facilitated by the metal chaperones HypA and HypB (Lubitz et al. 2014; Khorasani-Motlagh et al. 2019). In *E. coli* HypC and HypA are required for the maturation of hydrogenase 3 and functionally replaced by HybG and HybF, respectively, for the synthesis of hydrogenase 1 and 2 (Blokesch et al. 2001a; Hube et al. 2002).

Finally, most but not all hydrogenases undergo proteolytic cleavage of the C-terminus of the large subunit, which is mediated by a specific endopeptidase (Thiemermann et al. 1996; Binder et al. 1996). The maturation of the [NiFe]-hydrogenase is completed by the binding of the small subunit.

Although the maturation of [NiFe]-hydrogenases and the assembly of the $\text{NiFe}(\text{CN})_2(\text{CO})$ moiety are intensively studied and crystal structures of all individual Hyp proteins and of the transient HypCD, HypCDE and HypEF complexes are available, the detailed maturation mechanism is not yet fully unraveled.

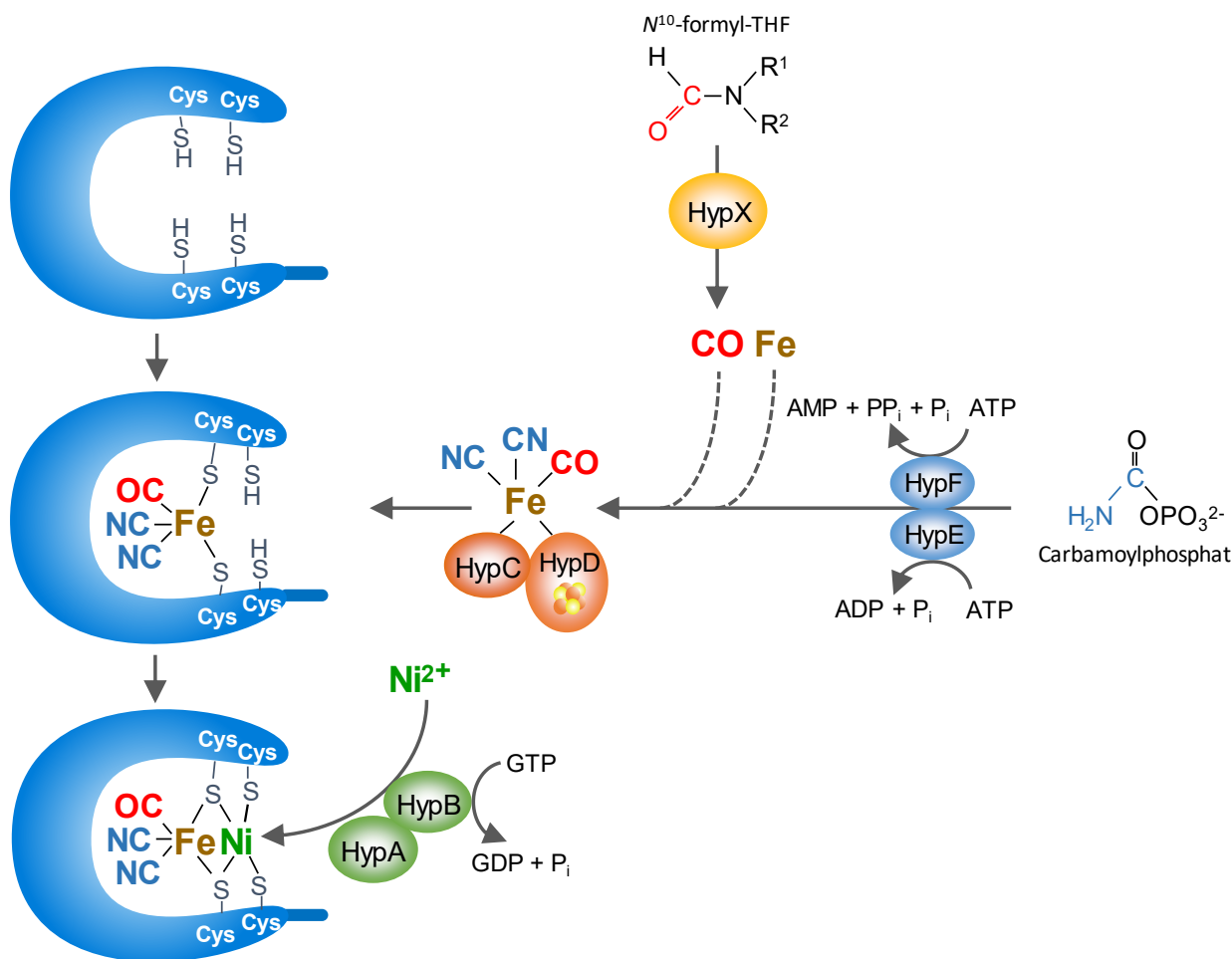


Figure 6. Model of the assembly of the NiFe(CN)₂(CO) active site in [NiFe]-hydrogenases under aerobic conditions. The HypCD complex (orange) serves as scaffold for the assembly of the Fe(CN)₂(CO) moiety. HypE and HypF (blue) provide the two CN⁻ ligands. HypX (yellow) synthesizes the CO ligand under aerobic conditions. The Fe(CN)₂(CO) complex is transferred from the HypCD complex to the apo-form of the hydrogenase large subunit (blue, C-shaped). HypA and HypB (green) insert the Ni ion.

1.2.1. HypCD serves as scaffold for the Fe(CN)₂(CO) synthesis

Among the Hyp proteins, HypD is the only member carrying an FeS cluster (Blokesch and Böck 2006; Blokesch et al. 2004b). The cubane-type [4Fe-4S] cluster is coordinated to the protein by four conserved cysteine residues that are arranged in a unique CX₁₄CX₆CX₁₆CX coordination motif (Blokesch et al. 2004b; Watanabe et al. 2007; Blokesch and Böck 2006). Its function is still under debate (see below).

HypD and HypC form a tight complex, which according to the current model, is the central construction site in the biosynthesis of the Fe(CN)₂(CO) moiety. It interacts with HypE, which is involved in CN⁻ ligand synthesis and HypX, which is required for aerobic CO ligand synthesis (Muraki et al. 2019; Blokesch et al. 2004b; Watanabe et al. 2012a; Jones et al. 2004).

Introduction

The presence of the $\text{Fe}(\text{CN})_2(\text{CO})$ moiety on HypCD was demonstrated by IR spectroscopic analysis of purified HypCD complexes from *R. eutropha* and *E. coli* (Bürstel et al. 2012; Soboh et al. 2012). IR analysis of isolated *E. coli* HypD in the absence of HypC revealed the same spectral pattern with the characteristic CO and CN^- signatures as the HypCD complex, whereas isolated HypC shows no absorption bands in the CO/ CN^- region, which has been interpreted as that HypD alone might serve as scaffold for the assembly of the $\text{Fe}(\text{CN})_2(\text{CO})$ moiety (Stripp et al. 2013). However, in *in vitro* transfer assays, the radioactively labeled CN^- group was transferred from HypE to the HypCD complex, but not to HypD alone (Blokesch et al. 2004).

The $\text{Fe}(\text{CN})_2(\text{CO})$ moiety is presumably coordinated to the HypCD complex via two conserved cysteine residues; Cys2 in the N-terminal domain of HypC and Cys41 in HypD (*E. coli* numbering) (**Figure 7**). The functional importance of these two cysteine residues was shown in several studies. Amino acid exchanges of each cysteine residue abolished complex formation, hydrogenase maturation, and H_2 production (Blokesch and Böck 2006, 2002; Magalon and Böck 2000; Soboh et al. 2012; Bürstel et al. 2012). IR spectroscopic analysis of an *E. coli* HypC-HypD(C41A) variant revealed an IR spectrum lacking the absorption bands characteristic for the CN^- and CO ligands, indicating that Cys41 in HypD is required to coordinate the $\text{Fe}(\text{CN})_2(\text{CO})$ moiety (Soboh et al. 2012). Crystal structures of the *T. kodakarensis* HypCD and the HypCDE complex support the role of the two conserved cysteine residues as Fe binding site, as they are in close proximity to each other and to the cyanide group on HypE (Watanabe et al. 2012a; Watanabe et al. 2007). Unfortunately, a crystal structure of the HypCD complex carrying the additional iron is not available. Hence, the precise details of the coordination of the $\text{Fe}(\text{CN})_2(\text{CO})$ moiety remain elusive. Coordination of the $\text{Fe}(\text{CN})_2(\text{CO})$ moiety to the HypCD complex by two cysteine residues would yield a stable 5-fold coordination of the Fe (**Figure 7 A**). In case of the precursor Fe, additional residues or other ligands might be involved since an initial twofold coordination of the Fe is very unlikely. In close proximity of the putative Fe-binding site in *T. kodakarensis* HypCD, two conserved histidine residues His41 and His202 (H44 and H201, *E. coli* numbering) have been identified that might be (temporarily) involved in Fe binding (**Figure 7 B**) (Watanabe et al. 2007; Albareda et al. 2013), although exchanges of these histidine residues did not affect hydrogenase maturation in *E. coli* (Blokesch and Böck 2006). Based on the structural similarity of the HypD α/β domains to sugar-binding proteins, Watanabe and coworkers proposed that a sugar molecule or a carbonate might be additionally involved in Fe binding by the HypCD complex (Watanabe et al. 2012a).

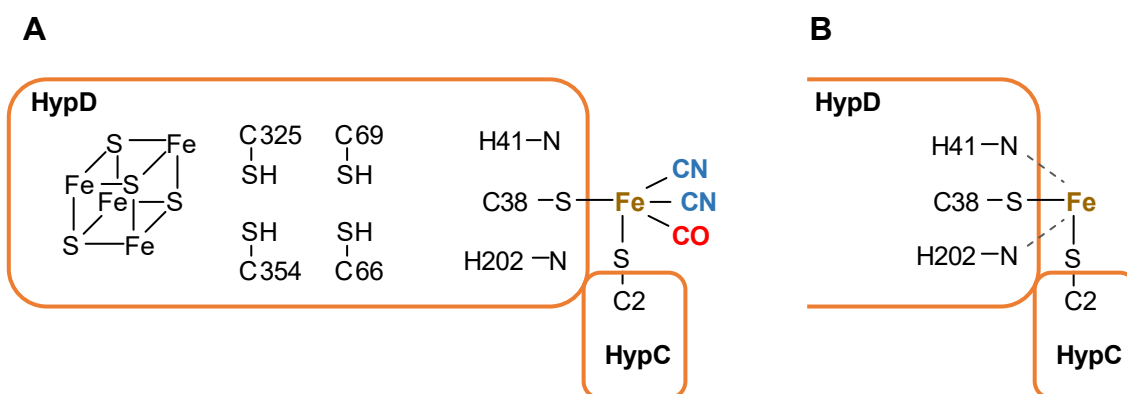


Figure 7. Model of the Fe binding site of HypCD. (A) $\text{Fe}(\text{CN})_2(\text{CO})$ binding, (B) binding of the precursor Fe. Amino acid numbering refers to the HypC and HypD proteins of *T. kodakarensis*, based on the crystal structure of *T. kodakarensis* HypCD (PDB: 3VYR).

During the maturation process, the precursor Fe is supposed to receive the CN^- and CO ligands. The CN^- ligands are synthesized by HypE and HypF and transferred from HypE to HypCD via a yet unknown mechanism (see chapter 1.2.2). CO ligand synthesis under aerobic conditions requires HypX (see chapter 1.2.3). The pathway for anaerobic CO ligand synthesis is still not clear. It is under debate whether the $[\text{4Fe-4S}]$ cluster in HypCD plays a role in anaerobic CO ligand synthesis by reduction of CO_2 , or in the CN^- ligand transfer from HypE (Watanabe et al. 2007; Watanabe et al. 2012a; Soboh et al. 2013). The order of CN^- and CO attachment to the precursor Fe is still under debate. Indication that CN^- loading is a prerequisite for the addition of CO was obtained by IR spectroscopic analysis. HypCD, purified from cells in which the CN^- but not the CO biosynthesis pathway is disrupted, revealed an IR spectrum lacking the absorption bands for both the CN^- and CO ligands (Bürstel et al. 2012). However, the observation of an additional CO band in the IR spectrum of purified HypCD, which was assigned as Fe(I)-CO species suggests the opposite order of ligand attachment (Stripp et al. 2014).

After assembly, the $\text{Fe}(\text{CN})_2(\text{CO})$ moiety needs to be delivered to the hydrogenase large subunit. Since it has been shown that HypC forms a complex with the apo-large subunit it was proposed that it is involved in the transfer of the $\text{Fe}(\text{CN})_2(\text{CO})$ moiety (Drapal and Böck 1998; Blokesch and Böck 2002). Complex formation of HypC with the apo-large subunit depends on the conserved C-terminal Cys2 residue, suggesting that it also plays a role in the $\text{Fe}(\text{CN})_2(\text{CO})$ delivery (Blokesch et al. 2001a; Magalon and Böck 2000).

Interestingly, it was recently discovered that purified *E. coli* HypCD as well as the individual HypD and HypC/HybG proteins display an ATPase activity (Nutschan et al. 2019). The function of the ATPase activity is yet unknown.

1.2.2. Cyanide ligand synthesis and transfer

CN⁻ ligand synthesis is catalyzed from carbamoyl phosphate by a complex of HypF and HypE. First, HypF catalyzes the carbamoylation of a conserved C-terminal cysteine residue of HypE producing HypE-thiocarbamate (Blokesch et al. 2004c; Reissmann et al. 2003). Based on structural analysis on HypF, three catalytic sites have been identified catalyzing three consecutive reactions (**Figure 8**). Each catalytic site is connected by protein channels, suggesting that the consecutive reactions occur without the release of the intermediates (Shomura and Higuchi 2012; Petkun et al. 2011). The first reaction is the dephosphorylation of carbamoyl phosphate to carbamate, which then reacts at the second catalytic site with ATP to carbamoyladenylate and pyrophosphate (PP_i). Finally, the carbamoyl group is transferred to the C-terminal cysteine residue of HypE while AMP is released (Rangarajan et al. 2008; Shomura and Higuchi 2012; Petkun et al. 2011). The C-terminal tail of HypE is flexible and can adopt an inward or an outward conformation. To receive the carbamoyl group, the C-terminal tail assumes the outward conformation to get in close contact with HypF (Rangarajan et al. 2008; Shomura and Higuchi 2012; Shomura et al. 2007). Upon ATP binding to HypE the C-terminal tail adopts the inward conformation. In an internal ATP-dependent dehydration reaction, HypE converts the protein-bound thiocarbamate into thiocyanate (**Figure 8**) (Blokesch et al. 2004c; Reissmann et al. 2003; Rangarajan et al. 2008; Watanabe et al. 2007; Shomura et al. 2007). IR Spectroscopic analysis of HypE and HypEF suggested the presence of a protein-bound isothiocyanate on HypE instead thiocyanate group (Stripp et al. 2015).

Introduction

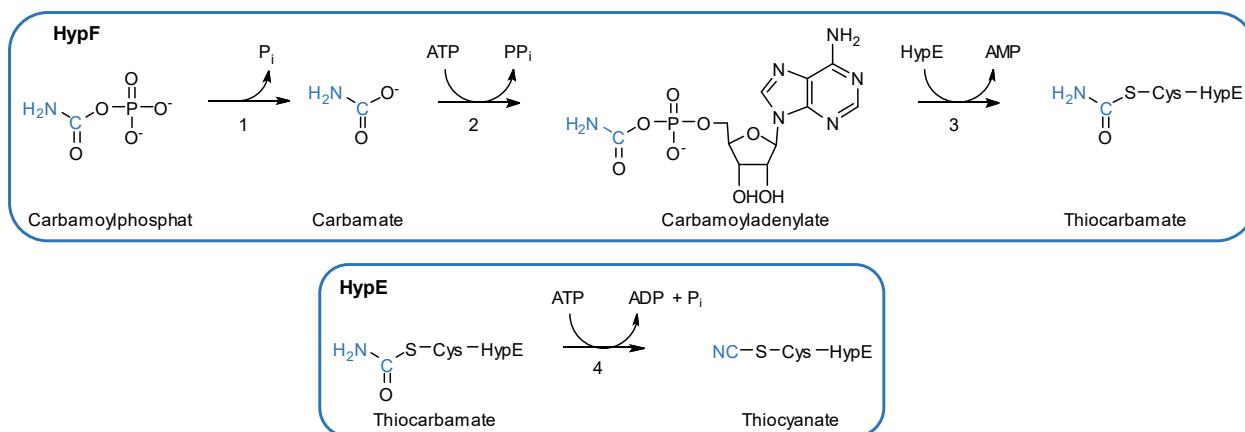


Figure 8. CN⁻ ligand synthesis catalyzed by HypF and HypE. HypF catalyzes the carbamoylation of the C-terminal cysteine residue of HypE in three steps: (1) dephosphorylation of carbamoyl phosphate to carbamate, (2) addition of carbamate to AMP forming carbamoyladenylate, (3) transfer of the carbamoyl group to HypE. HypE catalyzes the dehydration of HypE-bound thiocarbamate into thiocyanate (4).

After dehydration of the HypE-bound thiocarbamate into thiocyanate, the HypEF complex dissociates and HypE forms a complex with HypCD. Complex formation with HypCD induces conformational changes of the C-terminal tail of HypE resulting in the outward conformation to facilitate the delivery of the CN⁻ group to the precursor Fe of HypCD (Watanabe et al. 2012a). In this conformation, the cyanated C-terminal cysteine residue is in close proximity to conserved motifs in HypD, which are proposed to be involved in CN⁻ transfer. In the crystal structure of *T. kodakarensis* HypD, two pairs of cysteine residues (Cys66 and Cys69, Cys325 and Cys354) are located next to the Fe-binding site. They are linked to the [4Fe-4S] cluster of HypD and form a putative ferredoxin:thioredoxin reductase (FTR)-like redox cascade (Watanabe et al. 2007; Watanabe et al. 2012b). In the proposed cyanation mechanism, Cys66 attacks the HypE-Cys338-thiocyanate leading to the transfer of the first CN⁻ group to the HypCD-bound Fe (**Figure 9**, steps 1 and 2). The resulting heterodisulfide bond between HypD-Cys66 and HypE-Cys338 can be continuously reduced by the thiol redox cascade (**Figure 9**, steps 2 – 5), thereby regenerating HypD-Cys66 for the second CN⁻ ligand transfer. Reduction of the disulfide bonds of the two cysteine pairs after the second transfer may be mediated by the [4Fe-4S] cluster in an FTR-like manner (Watanabe et al. 2012a; Watanabe et al. 2007). The proposed cyanide mechanism is supported by the observation that chemical modification of the free thiols inhibits CN⁻ ligand transfer (Blokesch and Böck 2006).

Introduction

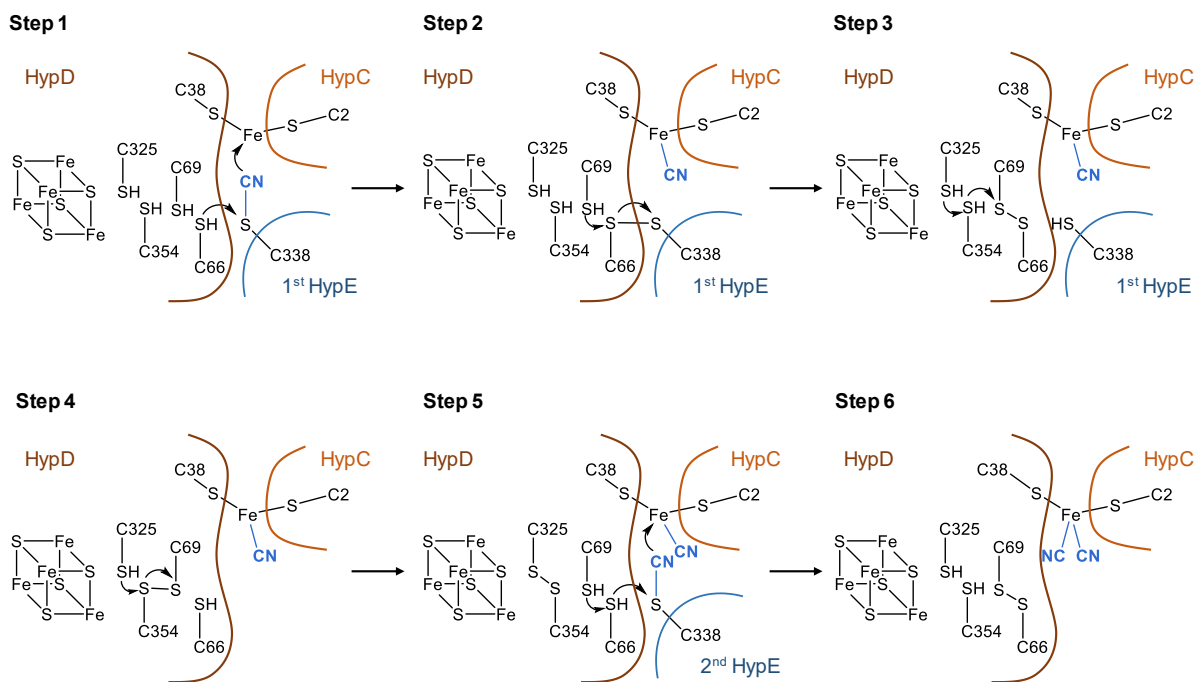


Figure 9. Proposed cyanation mechanism in the HypCDE complex. Amino acid numbering refers to the HypC, HypD, and HypE proteins of *T. kodakarensis*. C66 attacks the HypE-C338-thiocyanate leading to the transfer of the first CN⁻ group to the HypCD-bound Fe (steps 1 and 2). The resulting heterodisulfide bond between HypD-C66 and HypE-C338 is continuously reduced by the thiol redox cascade and HypE is released (steps 2 – 5). A second HypE protein binds to HypCD and the second CN⁻ ligand is transferred in the same way (steps 5 and 6).

Not all HypD proteins contain these two cysteine pairs. Of 448 analyzed HypD isoforms, 63 % contained two cysteine pairs, whereas 37 % contained only one pair of cysteine residues (Bürstel et al. 2012). For example, *E. coli* HypD possess only one cysteine pair, whereas *R. eutropha* HypD has two pairs. Mutant analysis of *R. eutropha* HypD revealed, that the pair of cysteine residues proximal to the FeS cluster are dispensable for HypD function, while exchanges in the distal cysteine pair almost abolished HypD function (Bürstel et al. 2012).

1.2.3. HypX – CO ligand synthesis under aerobic conditions

At least two different pathways for CO ligand synthesis have been proposed for [NiFe]-hydrogenase (Bürstel et al. 2011). One is functional during hydrogenase biosynthesis under anaerobic and microaerobic conditions and proposed to convert CO₂ reductively into CO (Soboh et al. 2013; Soboh et al. 2012). The other is functional under aerobic conditions and responsible for CO ligand insertion into [NiFe]-hydrogenases that are assembled and functional under aerobic conditions (Lenz et al. 2015). Aerobic CO biosynthesis involves an additional maturation protein, designated HypX, which occurs exclusively in microorganisms

synthesizing [NiFe]-hydrogenases under oxic conditions (Buhrke and Friedrich 1998; Bürstel et al. 2016). First evidence for HypX-mediated CO synthesis was obtained by hydrogenase maturation studies on the aerobic H₂-oxidizing proteobacterium *R. eutropha*. Compared to the wild type strain *R. eutropha* H16, HypX-deficient *R. eutropha* strains showed a considerable growth delay when cultivated with a gas mixture containing H₂, CO₂ and 15% O₂. Wild type-like growth could be restored by addition of external CO gas (Bürstel et al. 2016). Members of the HypX family show a bipartite structure with an N-terminal and a C-terminal module with similarities to N¹⁰-formyltetrahydrofolate (N¹⁰-formyl-THF) transferases and enoyl-CoA hydratases/isomerases of the crotonase superfamily, respectively (Rey et al. 1996). These similarities suggest that HypX proteins catalyze two different consecutive reactions: the transfer of the formyl group of N¹⁰-formyl-THF to an unknown substrate and a reaction involving oxyanion-based chemistry on a Coenzyme A (CoA) derivative. In fact, it has been shown in *in vivo* experiments that the ¹³C-labelled formyl group of N¹⁰-formyl-THF ends up as Fe-bound active site ¹³CO ligand of the regulatory hydrogenase (RH) of *R. eutropha*. Isotopic labeling of the CO ligand was not observed in mutant strains lacking functional HypX protein (Bürstel et al. 2016).

1.3. Aim of the study

One topic of this study is the investigation of the [NiFe]-hydrogenase maturation process, with a particular focus on the assembly and delivery of the Fe(CN)₂(CO) unit involving the HypCD complex and the aerobic CO ligand synthesis catalyzed by HypX.

The biosynthesis of the NiFe active site has been intensively studied using biochemical, spectroscopic and structural methods (see reviews (Lacasse and Zamble 2016; Watanabe et al. 2012b)). According to the current knowledge, the HypCD complex serves as a scaffold for the assembly of the Fe(CN)₂(CO) unit. Two CN⁻ ligands and one CO ligand are supposed to be attached to an Fe ion jointly coordinated by HypC and HypD. Besides the order of ligand binding, the origin of the precursor Fe and its coordination to the HypCD complex remain elusive. It is also not clear how the precise stoichiometry of one CO and two CN⁻ ligands is maintained. Upon assembly of the Fe(CN)₂(CO) unit on HypCD, this synthon becomes delivered to the hydrogenase apo-large subunit. How this is achieved by HypC, HypD or both is not yet understood.

Introduction

Synthesis of the CN^- ligands is catalyzed by the maturases HypE and HypF. For CO ligand biosynthesis at least two different pathways have been proposed. Little is known so far about the pathway which is active under anaerobic or microaerobic conditions. Under aerobic conditions an additional maturation protein, HypX, uses N^{10} -formyl-THF to synthesize the CO ligand of the hydrogenase active site (Bürstel et al. 2016). The exact reaction mechanism, however, remains unclear.

To obtain a better understanding of the maturation process, purified *E. coli* HypCD was investigated using different spectroscopic techniques including Resonance Raman and IR spectroscopy. Apo-HypCD complex was used for *in vitro* maturation experiments.

To gain insight into the reaction mechanism by which HypX converts N^{10} -formyl-THF into CO, purified *R. eutropha* HypX protein was subjected to a comprehensive biochemical analysis. HypX-mediated CO production was monitored spectrophotometrically via the formation of carboxyhemoglobin (HbCO).

The second part of this study focusses on the detailed investigation of the thermostable *HtSH*. The first IR spectroscopic analysis of *HtSH* revealed a unique spectral pattern. It exhibits a band at 1993 cm^{-1} which could be assigned to a CO stretching mode. Such a high CO stretching frequency is very uncommon and might represent an unusual active site configuration (Preissler et al. 2018b). Prior to the first spectroscopic characterization, the first crystal structures of *HtSH* were obtained. In the oxidized state, the structure revealed an unprecedented conformation of the active site with a glutamate residue as bidentate Ni ligand in addition to three bridging cysteines and one terminal cysteine yielding in a six-fold coordination of the Ni (Shomura et al. 2017). To combine the structural and the IR spectroscopic findings, different *HtSH* variants carrying exchanges for the glutamate residue were generated and analyzed biochemically and spectroscopically.

2. Materials and Methods

2.1. Strains, plasmids, and oligonucleotides

The bacterial strains, plasmids and oligonucleotides used in this study are listed in **Table 1**, **Table 2** and **Table 3**.

Table 1. Bacterial strains used in this study.

Strains	Characteristics*	Reference
<i>R. eutropha</i>		
HF469	MBH ⁺ SH ⁺ RH ⁺ , HoxJ ^{G422S} , <i>hypX</i> Δ ₂	(Buhrke and Friedrich 1998)
H16	MBH ⁺ SH ⁺ RH ⁺ , HoxJ ^{G422S}	DSM 428, ATCC 17699
HF1054	<i>ΔhoxG, ΔhoxFUYHW, ΔhoxI (330-bp NarI/MroI deletion)</i>	(Preissler et al. 2018b)
HF497	<i>ΔhypD, ΔhoxG, ΔhoxH</i>	Lenz lab
HP73	HF469 carrying pTS1 (<i>malE-hypX</i>)	this study
HP74	HF469 carrying pTS2 (<i>hypX</i>)	this study
HP77	HF469 pEDY309	this study
HP75	HF469 carrying pTS3	this study
HP76	HF469 carrying pTS4	this study
HP86	HF1054 carrying pTS10	this study
HP87	HF1054 carrying pTS11	this study
HP88	HF1054 carrying pTS12	this study
HF497	<i>ΔhypD, ΔhoxG, ΔhoxH</i>	Lenz lab
HP68	HF497 carrying GC50	Giorgio Caserta, unpublished
<i>E. coli</i>		
Rosetta™(DE3)	F ⁻ <i>ompT hsdS_B(r_B⁻ m_B⁻) gal dcm</i> (DE3) pRARE (Cam ^R)	Novagen, Germany
NEB 10-beta	<i>Δ(ara-leu) 7697 araD139 fhuA ΔlacX74 galK16 galE15 e14- φ80dlacZΔM15 recA1 relA1 endA1 nupG rpsL (Str^R) rph spoT1 Δ(mrr-hsdRMS-mcrBC)</i>	NEB, Germany
JM109	<i>recA1 endA1 supE44 gyrA96 thi hsdR17(rK - mK +) relA1 Δ(lac-proAB) e14- mcrB+ F'[traD36 proAB+ lacq lacZΔM15]</i>	(Yanisch-Perron et al. 1985)

Materials and Methods

Strains	Characteristics*	Reference
S17-1	Tra ⁺ <i>recA</i> , <i>pro thi</i> , <i>hsdR chr</i> :RP4-2	(Simon et al. 1983)
AK2473	Rosetta TM (DE3) carrying pCH631	this study
AK2502	Rosetta TM (DE3) carrying pThypDCstrep	this study
AK2503	Rosetta TM (DE3) carrying pTDEFcstrep	this study
AK2480	Rosetta TM (DE3) carrying pTS5	this study
AK2481	Rosetta TM (DE3) carrying pTS6	this study
AK2482	Rosetta TM (DE3) carrying pTS7	this study
AK2483	Rosetta TM (DE3) carrying pTS8	this study
AK2504	Rosetta TM (DE3) carrying pTS9	this study
AK2505	Rosetta TM (DE3) carrying pTS13	this study
AK2506	Rosetta TM (DE3) carrying pTS14	this study
AK2507	Rosetta TM (DE3) carrying pTS15	this study
AK2508	Rosetta TM (DE3) carrying pTS16	this study

*Plasmids are described in Table 2

Table 2. Plasmids used in this study.

Plasmids	Characteristic	Reference
pCH631	<i>hypX</i> fused at 5' end to <i>malE</i> in pMal-c2, encoding MBP-HypX	(Bürstel et al. 2016)
pTS1	3.5 kb PvuII fragment from pCH631 containing P _{tac} - <i>malE-hypX</i> in SwaI-cut pEDY309	this study
pTS2	XbaI digested 1.9 kb PCR product carrying P _{tac} - <i>hypX</i> amplified with primers 1 and 2 using pCH631 as template in XbaI-cut pEDY309	this study
pTS3	3.5 kb PvuII fragment from pCH631 carrying P _{tac} <i>malE-hypX</i> in Eco53kI-cut pCM62	this study
pTS4	XbaI-cut 1.9 kb PCR product carrying P _{tac} - <i>hypX</i> amplified with primers 1 and 2 using pCH631 as template in XbaI-cut pCM62	this study
pTS5	pMal-c2 carrying P _{tac} <i>malE-HthypX</i> encoding MBP-HtHypX, created by Gibson assembly, 6.7 kb PCR product amplified with Primers 5 and 6 using pCH631 as template, 1.7 kb PCR product amplified with primers 3 and 4 using genomic DNA of <i>H. thermoluteolus</i> as template	this study
pTS6	pMal-c2 carrying P _{tac} <i>strepHthypX</i> with a Strep-tag II coding sequence fused to the 5' end of <i>HthypX</i> , created by Gibson assembly, 5.6 kb PCR	this study

Materials and Methods

Plasmids	Characteristic	Reference
	product amplified with primers 5 and 8 using pCH631 as template, 1.8 kb PCR product amplified with primers 7 and 4 using pTS5 as template	
pTS7	MBP-HypX S448A, QuikChange site-directed mutagenesis using primers 9 and 10 with pCH631 as template	this study
pTS8	MBP-HypX Y439F, Q5 [®] site-directed mutagenesis with primers 11 and 12 using pCH631 as template	this study
pTS9	MBP-HypX E449Q, site-directed mutagenesis via Gibson assembly, 2 kb PCR product amplified with primers 13 and 14 using pCH631 as template, 6.5 kb PCR product amplified with primers 15 and 16 using pCH631 as template	This study
pTS10	<i>HtSH</i> HoxH E32Q, mutagenesis via Gibson assembly, 3.6 kb PCR product amplified with primers 17 and 18 using pLL2000 as template, 2.1 kb PCR product amplified with primers 19 and 20 using pLL2000 as template, XbaI-, Eco53kI-cut pEDY309	this study
pTS11	<i>HtSH</i> HoxH E32A, mutagenesis via Gibson assembly, 3.6 kb PCR product amplified with primers 17 and 21 using pLL2000 as template, 2.1 kb PCR product amplified with primers 22 and 20 using pLL2000 as template, XbaI-, Eco53kI-cut pEDY309	this study
pTS12	<i>HtSH</i> HoxH E32D, mutagenesis via Gibson assembly, 3.6 kb PCR product amplified with primers 17 and 23 using pLL2000 as template, 2.1 kb PCR product amplified with primers 24 and 20 using pLL2000 as template, XbaI-, Eco53kI-cut pEDY309	this study
pTS13	<i>hypE</i> fused at 5' end to a hexa-His-tag coding sequence in a modified pET15b, created by Gibson assembly, 5.7 kb PCR product amplified with primers 25 and 26 using <i>Fold</i> -pET15bTEV as template, 1.1 kb PCR product amplified using primers 29 and 30 with pThypDEFCstrep as template	This study
pTS14	<i>hypF</i> fused at 5' end to a hexa-His-tag coding sequence in pET15b, created by Gibson assembly, 5.7 kb PCR product amplified with primers 25 and 26 using <i>Fold</i> -pET15bTEV as template, 2.3 kb PCR product amplified using primers 27 and 28 with pThypDEFCstrep as template	This study
pTS15	pT7-7, <i>hypD</i> , <i>hypE</i> , <i>hypC_{His}</i> , <i>hypF</i> , hexa-His tag sequence fused at the 5' end of <i>hypC</i> introduced via Gibson assembly using primer pairs 14, 31 and 32, 33 with template pThypDEFCstrep	This study
pTS16	pT7-7, <i>hypD</i> , <i>hypC_{His}</i> , hexa-His tag sequence fused at the 5' end of <i>hypC</i> introduced via Gibson assembly using primer pairs 15, 34 and 14, 33 with template pThypDCstrep	This study
GC50	<i>hoxG</i> with C-terminal extension and with a Strep-tag II coding sequence fused to the 5' end of <i>hoxG</i> in pEDY309	Giorgio Caserta, unpublished
pJP09	pEDY309 carrying P _{SH} <i>Hthox_{strep}FUYHW</i> with a Strep-tag II coding sequence fused to the 5' end of <i>hoxF</i>	(Preissler et al. 2018b)

Materials and Methods

Plasmids	Characteristic	Reference
pLL2000	Km ^R , ColE1 <i>ori</i> , M13 <i>ori</i> , P _{SH} -Hthox _{Strep} FUYHW in pGE837	(Preissler et al. 2018b)
pEDY309	Tet ^R , RK2 <i>ori</i> , Mob ⁺	(Kleihues et al. 2000)
pCM62	Tet ^R , P _{lac} , ColE1 <i>ori</i> , <i>oriV</i> , <i>oriT</i>	(Marx and Lidstrom 2001)
<i>Fold</i> -pET15bTEV	<i>P. aeruginosa fold</i> ligated into a modified pET15b vector containing a Tobacco Etch Virus (TEV) protease recognition sequence in place of thrombin	(Eadsforth et al. 2012)
pThypDCstrep	pT7-7, <i>hypD</i> , <i>hypC_{Strep}</i> , Amp ^R	(Blokesch et al. 2004b)
pThypDEFcstrep	pT7-7, <i>hypD</i> , <i>hypE</i> , <i>hypC_{Strep}</i> , <i>hypF</i> , Amp ^R	(Blokesch et al. 2004b)

Table 3. Oligonucleotides used in this study.

No	Name	Sequence
1	Ptac_hypX fwd	ctctagatgttgacaattaatcatcggctcgataatgtgtcaaggaccatagattatgcatattgctcctcacc
2	Ptac_hypX rev	cagatctcaagatcggttccccgcaag
3	Ht_hypX for	aataacaacaacctcgggatcgagggaaggatgcgtatcctgcttttggtccatg
4	Ht_hypX rev	aagaacagtggcctgctgtcagacatggcttacacctccatgaagagcgattgccgc
5	pMal-for	gccatgtctgacaagcaggccactgttctt
6	pMal-rev	cctccctcgatcccagggtgtgtatt
7	Strep-HtHypX-for	atgtggagccaccgcagttcgaaaaagctggcatgcgtatcctgcttttggtccatgc
8	pMal-rev-strep	gccagcttttcgaactcgggtggctccacataatctatggctcctgttggtgaagtgctcg
9	MBP-HypX.S448A-for	gggcaatctgtatggtgcggaatactggacctatc
10	MBP-HypX.S448A-rev	gataggtccagatattccgcaccatacagattgccc
11	Y439F_Q5_F	aatccgcactcaagaacatggg
12	Y439F_Q5_R	cacgagtacacctcgcg
13	1_E449 for	caatctgtatggttcgcaatac
14	2_Amp rev	gataccgcgagaccac
15	3_Amp for	gataaatctggagccggtg
16	4_E449 rev	caacagataggtccagattg

Materials and Methods

No	Name	Sequence
17	1_pEDY XbaI pLL2000	ctaactagttcgaagcttgagatctcctctagaaccggtgacgtcaccatgggaag
18	2_HoxH E32Q	cttgccatggccttgacgcgggagag
19	3_HoxH E32Q for	ctctcccgcgtccaaggccatggcaag
20	4_pLL2000 Eco53kI pE DY	ggcaaaagctcatttaaatcagtcctcgggtacccgggatccatgctacc
21	2_HoxH E32A	cttgccatggcctgcgacgcgggagag
22	3_HoxH E32A for	ctctcccgcgtcgcaggccatggcaag
23	2_HoxH E32D	cttgccatggcctgcgacgcgggagag
24	3_HoxH E32D for	ctctcccgcgtcgcaggccatggcaag
25	pET15b rev	gccgctgctgtgatgatgatg
26	pET15b for	tcgaggatccggctgctaac
27	HypF N-term	catcatcatcacagcagcggcatggcaaaaaacacatcttg
28	HypF C-term	gttagcagccggatcctcgattatccgttctggactcac
29	HypE N-term	catcatcatcacagcagcggcgtgaataatatccaactgcccacgg
30	HypE C-term	gttagcagccggatcctcgattagcatatacgcggaagcgg
31	hypD rev	ggcattgatgcggcttac
32	Seq hypD	ggtgaggtattaacgggc
33	His HypCD rev_2	ttagtgatgatgatgatgatggccgctgctttttcctcgccatacaacagc
34	His HypCD for_2	agcagcggccatcatcatcatcactaaggggatcctctagagtcgac

2.2. Bacterial cultivation conditions

2.2.1. *R. eutropha*

R. eutropha strains were cultivated in mineral salts medium (**Table 4**) (Schlegel et al. 1961; Friedrich 1982). The medium is based on a phosphate buffer (H16 buffer) with a pH value of 7. Minerals and NH₄Cl as nitrogen source were added as listed in **Table 4**. Depending on the growth conditions different carbon sources were used. For heterotrophic growth fructose (FN medium) or a mix of fructose and glycerol (FGN_{mod} medium) were added. Lithoautotrophic cultures were grown without any organic carbon source in a desiccator filled with 10 % CO₂ as carbon source, 4 % H₂ as energy source, 15 % O₂, and 71 % N₂. Solid media contained 1.5 % (w/v) agar. Antibiotics were added as listed in **Table 5**.

Materials and Methods

Table 4. Mineral salts medium for cultivation of *R. eutropha*.

Ingredients	Final concentration
10x H16 buffer	
90 g Na ₂ HPO ₄ x 12 H ₂ O	25 mM
15 g KH ₂ PO ₄	11 mM
ad 1 L H ₂ O, adjust to pH 7 at RT, autoclave	
Additives (added sterile to 1 L 1x H16 buffer)	
10 ml NH ₄ Cl, 20% (w/v), autoclave	37.4 mM
1 ml MgSO ₄ x 7 H ₂ O, 20 % (w/v), autoclave	0.81 mM
1 ml CaCl ₂ x 2 H ₂ O, 1% (w/v), autoclave	0.068 mM
1 ml FeCl ₃ x 6 H ₂ O, 0.5 % (w/v) in 0.1 M HCl, sterile filtration	18 mM
1 ml NiCl ₂ x 6 H ₂ O, autoclave	0.001 mM
FN medium (added to H16 buffer with additives)	
10 ml Fructose, 40 % (w/v), sterile filtration	0.4 %
FGN_{mod} medium (added to H16 buffer with additives)	
1.25 ml Fructose, 40 % (w/v), sterile filtration	0.05 %
10 ml Glycerol, 40 % (w/v), autoclave	0.4 %

Table 5. Antibiotics used for cultivation.

Antibiotic	Stock solution	Final concentration
Carbenicillin	100 mg/ml in H ₂ O	100 µg/ml
Tetracycline	10 mg/ml in 80 % Ethanol	10 µg/ml
Chloramphenicol	34 mg/ml in 100 % Ethanol	34 µg/ml
Kanamycin	50 mg/ml in H ₂ O	50 µg/ml

Expression of genes under the control of the SH (P_{SH}) and MBH (P_{MBH}) promoters is regulated by the available carbon source and the temperature. Expression is induced in the absence of fructose when grown with glycerol or CO₂ as carbon source and at 30 °C. Molecular hydrogen is not required for expression. Growth at 37 °C or with fructose as carbon source represses gene expression (Friedrich et al. 1981; Friedrich and Friedrich 1983). Therefore, pre-cultures were grown in FN medium supplemented with 1 % LB medium at 37 °C overnight. Main

cultures for protein production under the control of the SH promoter were grown in FGN_{mod} medium at 30 °C. Cultures were inoculated with 1 % of an overnight pre-culture and grown in 4 L Erlenmeyer flasks filled to 80 % until an OD₄₃₆ > 10 was reached (after 7-10 days). Cells were harvested by centrifugation (11500 x g, 4 °C, 15 min). If not used immediately, the cell pellet was frozen in liquid nitrogen and stored at -80 °C.

For *in vivo* complementation studies, main cultures were inoculated to an OD₄₃₆ of 0.1 and grown lithoautotrophically in mineral salts medium with CO₂ as carbon source at 30 °C. Gene expression was regulated by the tac promoter (P_{tac}), which is a constitutive promoter in *R. eutropha* (Nakamura et al. 2000). Thus, no inducer of gene expression was added to the medium. All cultures were incubated in a shaker at 120 rpm. Growth was monitored by measuring the OD at 436 nm.

2.2.2. *E. coli*

E. coli strains were cultivated in LB medium (1 % (w/v) tryptone, 0.5 % (w/v) yeast extract) or TGYEP medium ((Begg et al. 1977) modified: (w/v) tryptone 1 %, 0.5 % (w/v) yeast extract, 0.8 % (w/v) glucose, 0.1 M potassium phosphate buffer pH 6.5). Antibiotics were added in the concentrations listed in **Table 5**.

For aerobic protein production, pre-cultures were grown overnight at 37 °C in LB medium while shaking at 120 rpm. Main cultures were inoculated with 1 % of the respective pre-culture and grown at 37 °C until an OD₆₀₀ of 0.4 – 0.8 was reached and gene expression was induced with 0.2 – 0.5 mM IPTG. After induction, cells were incubated overnight at 16 °C in LB medium and harvested by centrifugation (11500 x g, 4 °C, 15 min). Cell pellets were frozen in liquid nitrogen and stored at -80 °C.

Anaerobic cultures were grown in TGYEP medium in rubber stopper sealed serum bottles. Main cultures were inoculated with the respective aerobic overnight pre-cultures grown in LB medium at 37 °C. Anaerobiosis of the main culture was accomplished by O₂ consumption by the growing cells during the first hour of cultivation. Gene expression was induced with 0.2 – 0.5 mM IPTG at an OD₆₀₀ of 0.4 – 0.8. Cells were incubated overnight at 16 °C and harvested by centrifugation. When not used immediately, cell pellets were frozen in liquid nitrogen and stored at -80 °C.

2.2.3. Conservation of bacterial strains

Bacterial strains grown on agar plates were stored at 4 °C up to a few weeks. For long-term storage, glycerol stocks were prepared. Therefore, cultures were freshly grown in LB medium (*E. coli*) or FN medium (*R. eutropha*) with the respective antibiotics and sterile glycerol was added at a final concentration of 22 % (v/v). The glycerol stocks were frozen in liquid nitrogen and stored at -80 °C. For reactivation, cells of the frozen glycerol stock were scratched off with a sterile pipette and transferred to the appropriate medium.

2.3. Polymerase chain reaction (PCR)

PCR was performed using the following polymerases according to the supplier's protocols: Q5[®] High-Fidelity DNA polymerase (NEB, Germany), Phusion[®] High-Fidelity polymerase (NEB, Germany), LongAmp[®] Taq polymerase (NEB, Germany) and Taq polymerase (NEB, Germany). Oligonucleotides used in this study are listed in **Table 3**.

Colony-PCR: Colony-PCR was performed to screen for the successful integration of insert DNA into a plasmid after ligation or Gibson assembly. To determine whether the insert DNA has the correct size, primers binding to the vector DNA in the flanking region of the insert DNA were used. Colony material of individual transformants was directly added to the PCR reaction and lysed while the initial heating step. The released plasmid DNA served as template for the amplification. Taq or LongAmp[®] polymerases (NEB, Germany) were used with a modified PCR protocol where the initial heating step was increased to 5 min.

2.4. Determination of DNA concentrations

DNA concentrations were determined photometrically by measuring the extinction at 260 nm on a Nanophotometer P330 (Implen GmbH, Germany) or estimated by comparison with a DNA standard (2-log DNA ladder, NEB, Germany) after agarose gel electrophoresis.

2.5. Agarose gel electrophoresis

DNA fragments were separated by size using agarose gel electrophoresis. 0.8 – 2 % (w/v) agarose powder was dissolved in TPE buffer (80 mM Tris-H₃PO₄ (pH 7.6), 8 mM EDTA) by heating. Midori Green Advance (Nippon Genetics, Germany) was added for DNA staining.

Materials and Methods

The melted agarose gel was casted in horizontal gel chambers. A comb was placed in the liquid gel to create wells for loading the samples. Once the gel has set, the comb was removed, and the gel was covered with TPE buffer. Samples were prepared by adding gel loading dye (6x) (NEB, Germany) and loaded into the wells. 2-log DNA ladder (NEB, Germany) was run as standard. Electrophoresis was performed at 90 V and 400 mA for about 45 min. The gel was analyzed using an UV-transilluminator (UVT-28S, Herolab, Germany).

For the isolation of DNA fragments from agarose gels, the respective DNA fragments were first cut out from the gel with a scalpel, followed by DNA extraction using AgaroseOut Gel-Extraction DNA Kit (Roboklon GmbH, Germany) according to the manufacturer's protocol.

2.6. Restriction of DNA

The amounts of enzyme, buffer and DNA were used as recommended by the supplier (NEB, Germany). Incubation time was typically 1 h. If necessary, the incubation time was increased up to 16 h. The resulting fragments were separated by agarose gel electrophoresis and extracted as described in section 2.5.

2.7. Dephosphorylation and Phosphorylation of DNA fragments

Self-ligation of linearized vector DNA was prevented by dephosphorylation of the 3' and 5' ends of vector DNA by calf intestinal alkaline phosphatase (CIP, NEB, Germany). 1 U of CIP was added directly into the digestion reaction.

Blunt end PCR products were 5' phosphorylated prior ligation. T4 polynucleotide kinase and the respective T4 polynucleotide kinase reaction buffer (NEB, Germany) and ATP were incubated with the PCR product according to the manufacturer's protocol.

2.8. Ligation of DNA fragments

DNA fragments were ligated using T4 DNA ligase with the respective T4 DNA ligase reaction buffer (NEB, Germany). Vector DNA and Insert DNA were used in a ratio of 1:3 to 1:5. For difficult ligations, 10 % PEG 8000 was added. The reaction mix was incubated at 16 °C overnight or at room temperature for about 20 min.

Materials and Methods

2.9. Gibson assembly

Gibson assembly was used to insert one or more DNA fragments into a vector and for site-directed mutagenesis (Gibson et al. 2009). Vector DNA can either be linearized by restriction or synthesized by PCR. Adjacent DNA fragments require a 20 to 40 bp sequence overlap for successful assembly. The overlap was typically created by PCR. For site-directed mutagenesis, the mutation was inserted into the overlap region. In a 20 μ l reaction mix approximately 10 – 100 ng of each DNA fragment were added in equimolar amounts to 15 μ l assembly master mix (**Table 6**) and incubated at 50 °C for 1 h.

Table 6. Composition of the assembly master mix for Gibson assembly.

Volume/amount	Stock solution	Final concentration
5x ISO reaction buffer		
1.5 g	PEG 8000	25 % (w/v) PEG 8000
3000 μ l	1 M Tris-HCl pH 7.5	500 mM Tris-HCl pH 7.5
150 μ l	2 M MgCl ₂	50 mM MgCl ₂
300 μ l	1 M DTT	50 mM DTT
300 μ l	100 mM NAD ⁺	5 mM NAD ⁺
Fill up with H ₂ O to 6000 μ l		
Assembly master mix		
32 μ l	5x ISO reaction buffer	1x ISO reaction buffer
0.64 μ l	T5 exonuclease (10 U/ μ l)	0.04 U/ μ l
2 μ l	Phusion [®] DNA polymerase (2 U/ μ l)	0.025 U/ μ l
16 μ l	Taq DNA ligase (40 U/ μ l)	4 U/ μ l
48 μ l	10 mM dNTPs (2.5 mM each)	3 mM
Fill up with H ₂ O to 120 μ l, prepare 15 μ l aliquots		

2.10. Site-directed mutagenesis

Site-directed mutagenesis was either achieved by Gibson assembly, introducing the mutation with primers carrying the mutation in the overlapping region of two adjacent DNA fragments, by using the Q5[®] site-directed mutagenesis kit (NEB, Germany) following the manufacturer's

protocol or by the QuikChange method using two complementary primers carrying the desired mutation. After the PCR reaction, remaining template DNA was removed by DpnI digestion.

2.11. DNA sequencing

DNA sequencing was performed by the company Microsynth Seqlab, Germany, using the chain-termination method (Sanger et al. 1977).

2.12. Plasmid preparation

Depending on the size and the copy number of the plasmid (low copy or high copy plasmids) different kits were used for mini or midi preparations.

For smaller plasmids with a high copy number one of the following kits was used according to the manufacturer's protocol: Monarch® Plasmid Miniprep Kit (NEB, Germany), Plasmid Miniprep DNA Kit (Roboklon, Germany).

For large plasmids or low copy plasmids like pEDY309 the QIAGEN Plasmid Midi Kit (Qiagen, Germany) was used according to the manufacturer's protocol.

2.13. Plasmid transfer

2.13.1. Preparation of competent cells

Electrocompetent cells: For preparation of electrocompetent cells, 500 ml LB medium were inoculated with 1 ml overnight culture of the respective *E. coli* strain and incubated on a shaker at 120 rpm and 37 °C. The culture was grown until an OD₆₀₀ of 0.4 – 0.7 was reached. Cells were harvested at 3000 x g for 10 min at 4 °C. All following steps were performed on ice. The cell pellet was resuspended in 100 ml ice-cold H₂O and pelleted again. After washing three times the pellet was resuspended in 2 – 5 ml ice-cold 10 % glycerol (v/v). Aliquots of 50 µl cell suspension were frozen in liquid nitrogen and stored at –80 °C.

Chemically competent cells: For preparation of chemically competent cells, 100 ml LB medium were inoculated with 2 ml of the respective *E. coli* overnight culture and incubated in a shaker at 120 rpm at 37 °C for about 2 h until an OD₆₀₀ of 0.5 – 1.0 was reached. Cells were harvested at 4 °C, 4000 x g for 10 min. The cell pellet was resuspended in ice-cold TFB 1 buffer (100 mM RbCl, 50 mM MnCl₂, 30 mM K-acetate, 10 mM CaCl₂, 15 % glycerol (v/v), pH 5.8, adjusted with acetic acid; the buffer was sterilized by filtration) and the cell suspension was incubated on ice for 90 min. The cells were centrifuged again and the pellet was

Materials and Methods

resuspended in 4 ml of TFB 2 buffer (10 mM MOPS (pH 6.8, adjusted with NaOH), 10 mM RbCl, 75 mM CaCl₂, 15 % glycerol (v/v)) per 100 ml culture. Aliquots of 100 µl cell suspension were immediately frozen in liquid nitrogen and stored at -80 °C.

2.13.2. Transformation

Plasmid DNA was transferred into *E. coli* via electroporation or heat shock transformation. *E. coli* strains JM109 and NEB 10 beta were used for cloning, *E. coli* S17-1 was used for conjugation and *E. coli* Rosetta™(DE3) was used for protein production.

Electroporation: For transformation via electroporation, electrocompetent cells were thawed on ice and 1-5 µl of plasmid DNA, ligation reaction or Gibson assembly reaction were added to the cells. Cells and DNA were mixed by gently flicking the tube and the mixture was transferred to a pre-chilled electroporation cuvette. Electroporation was performed at 2500 V, 25 µF and 200 Ω using an EasyjecT Prima electroporator (EquiBio Ltd, UK). Immediately after electroporation, 900 µl of 37 °C warm SOC medium (2 % tryptone (w/v), 0.5 % yeast extract (w/v), 2.5 mM KCl, 10 mM MgCl₂, 20 mM glucose, pH 7) were added and cells were shaken at 37 °C for 1 h before they were plated on LB plates with the respective antibiotic and incubated overnight at 37 °C.

Heat shock: For heat shock transformation, chemically competent cells were thawed on ice. 1-10 µl of plasmid DNA, ligation reaction or Gibson assembly reaction were added to the cells and the tube was carefully flicked to mix the DNA and the cells. The mixture was incubated on ice for 30 min and subsequently heat shocked at 42 °C for 30 s and then incubated on ice for 5 min. After adding 900 µl of warm SOC medium, cells were shaken for 1 h at 37 °C. Finally, 100 – 1000 µl sample were plated on selection plates with the respective antibiotic and incubated overnight at 37 °C.

2.13.3. Conjugation

For the transfer of plasmids from the donor strain *E. coli* S17-1 into *R. eutropha* recipient strains, the agar spot mating technique was used. Therefore, both donor and recipient strain were cultivated overnight at 37 °C. *E. coli* strains were cultivated in 10 ml LB medium and *R. eutropha* strains were cultivated in 10 ml NB medium (0.3 % (w/v) beef extract, 0.5 % (w/v)

peptone, pH 6.8). Cells were harvested at 4000 x g, 4 °C for 5 min and washed with 5 ml H16 buffer and centrifuged again. The resulting pellets were resuspended in 200 µl H16 buffer and 100 µl of each cell suspension was mixed and streaked on LB plates without antibiotics and incubated at 37 °C until a thick layer of cells was visible. Cell material was scratched off the plate, washed in H16 buffer, and resuspended in 1 ml H16 buffer. 100 µl of diluted cell suspensions ($10^{-1} - 10^{-3}$) were plated on FN plates with the respective antibiotic and incubated at 37 °C for 2 to 3 days until colonies were visible. Single colonies were streaked again on fresh plates to gain a pure culture.

2.14. Protein purification

All purification steps were performed on ice or at 4 °C. Purity of the protein preparations was checked by SDS-PAGE (see chapter 2.16). Purified proteins were frozen in liquid nitrogen and either stored in liquid nitrogen or at -80 °C.

2.14.1. HypX

The following HypX proteins were overproduced in *E. coli* and purified by affinity chromatography: MBP-HypX from *R. eutropha*, MBP-*Ht*HypX from *H. thermoluteolus* and Strep-*Ht*HypX from *H. thermoluteolus*. Cell pellets were resuspended in 2 – 3 ml/g cells resuspension buffer (50 mM Tris-HCl pH 7.4 at 4 °C, 200 mM NaCl, 0.1 mM DTT) containing protease inhibitor cocktail (one tablet in 50 ml solution, Complete EDTA-Free, Roche) and DNaseI (tip of a spatula, Roche). Resuspended cells were disrupted in a French pressure cell at a pressure of 125 MPa. Soluble extract was obtained by ultracentrifugation (45 min, 4 °C, 100,000 x g) and loaded onto an Amylose Resin High Flow column (NEB, Germany) in case of MBP-HypX and MBP-*Ht*HypX or a Strep-Tactin high capacity column (IBA, Germany) for Strep-*Ht*HypX. After the columns were washed with 10 bed volumes (BV) washing buffer (50 mM Tris-HCl, pH 7.4 at 4 °C, 200 mM NaCl, 0.1 mM dithiothreitol (DTT)), the protein was eluted with 5 BV washing buffer containing either 10 mM maltose (MBP-HypX, MBP-*Ht*HypX) or 5 mM desthiobiotin (Strep-HypX). Eluted protein was concentrated by centrifugation using Ultra Centrifugal Filter Units (Amicon Ultra Ultracel 50K for MBP-HypX and MBP-*Ht*HypX and 30K for Strep-*Ht*HypX, Millipore).

Materials and Methods

For crystallization screenings, purified and concentrated Strep-*HtHypX* was further purified by size exclusion chromatography using a Superdex 200 10/30 GL column (GE healthcare, Germany) equilibrated with crystallization buffer (20 mM Tris-HCl pH 7.4 at 4 °C, 150 mM NaCl, 0.05 mM CoA) with the ÄKTA pure system (GE healthcare, Germany) at a flow rate of 0.4 ml/min. The eluate was collected in 0.3 ml fractions. Elution of the protein was monitored at 280 nm. Fractions containing monomeric Strep-*HtHypX* were pooled and concentrated.

2.14.2. *HtSH*

Purification of *HtSH* and *HtSH* variants was carried out as described before (Preissler et al. 2018b; Preissler 2018a). Before resuspension, the buffer and the frozen cell pellet were made anaerobic by gassing with argon for 20 min. Cells were resuspended in 2 ml resuspension buffer per 1 g cells. The purification buffer contained 50 mM KPO₄, pH 7.2, 15 % glycerol (v/v), 5 mM MgCl₂ and 0.5 mM NiCl₂. The resuspension buffer contained additionally 5 mM NAD⁺, protease inhibitor cocktail (Complete EDTA-Free, Roche) and DNaseI (Roche). NAD⁺ was added to keep the *HtSH* oxidized to prevent oxidative damage. Cells were disrupted by two passages through a chilled french pressure cell at a pressure of 125 MPa. To keep micro-aerobic/anoxic conditions the ultracentrifuge tubes were gassed with argon before being filled with cell extract. Soluble extract was obtained by ultracentrifugation (45 min, 4 °C, 100,000 x g) and loaded onto a Strep-Tactin high capacity column (IBA, Germany). The column was previously equilibrated with purification buffer supplemented with 5 mM NAD⁺. After washing with two BV of purification buffer with 5 mM NAD⁺ and four BV purification buffer without NAD⁺ the protein was eluted with 5 BV purification buffer containing 5 mM desthiobiotin. Eluted protein was concentrated using Ultra Centrifugal Filter Units (Amicon Ultra Ultracel 100K, Millipore).

To obtain *HtSH* protein with homogeneous subunit stoichiometry, the concentrated protein was further purified by size-exclusion chromatography. A maximum amount of 10 mg of protein was loaded on a Superdex 200 10/30 GL column (GE healthcare, Germany) equilibrated with purification buffer. Size exclusion chromatography was performed with ÄKTA pure system at a flow rate of 0.3 ml/min. Elution of the protein was monitored at 280 nm. Additionally absorbance at 420 nm was monitored, which is specific for FeS cluster containing proteins. The eluate was collected in 0.4-ml fractions. Fractions containing *HtSH* protein with an

apparent subunit stoichiometry of about 1:1:1:1, visualized by SDS-PAGE, and highest activity were pooled and concentrated.

2.14.3. HypCD

Overproduction of HypCD took place in *E. coli* Rosetta™(DE3) transformed with plasmid pThypDCstrep or pThypDChis, encoding apo-HypCD, or pThypDEFcstrep or pThypDEFChis, encoding holo-HypCD. Cell pellets of aerobic or anaerobic grown cells were resuspended in 2-3 ml per 1 g cells of washing buffer (100 mM Tris-HCl pH 8 at 4 °C, 100 mM NaCl, (±) 0.1 mM DTT) containing protease inhibitor cocktail and DNaseI. Cell disruption and preparation of soluble extract were performed as described in chapter 2.14.1. Strep-tagged proteins were purified via a Strep-Tactin high capacity column (IBA, Germany). Soluble extract was loaded on a column equilibrated with washing buffer. After washing with 5 BV of washing buffer the protein was eluted with 5 BV washing buffer containing 5 mM desthiobiotin. His-tagged proteins were purified via a Ni-NTA superflow column (IBA, Germany). Before loading the soluble extract, the column was equilibrated with washing buffer. After the soluble extract was applied, the column was washed with two BV washing buffer, three BV washing buffer containing 10 mM imidazole and three BV washing buffer containing 20 mM imidazole. The protein was eluted with 5 BV washing buffer containing 250 mM imidazole. Purified proteins were concentrated by centrifugation using Ultra Centrifugal Filter Units (Amicon Ultra Ultracel 10K, Millipore). To reduce the imidazole concentration, concentrated His-tagged proteins were washed three times with washing buffer without imidazole and concentrated again. All purified proteins were flash frozen and stored in liquid nitrogen.

2.14.4. HypE and HypF

His-tagged HypE and HypF proteins were purified from aerobically grown *E. coli* Rosetta™(DE3) cells. Cell pellets were resuspended in washing buffer containing protease inhibitor cocktail (one tablet in 50 ml solution, Complete EDTA-Free, Roche) and DNaseI (tip of a spatula, Roche). HypE washing buffer contained 50 mM Tris-HCl, pH 7.5 at 4 °C, 50 mM NaCl, 10 mM Mg acetate, 0.1 mM DTT. HypF washing buffer contained 50 mM Tris-HCl pH 7.5 at 4 °C, 50 mM KCl, 10 mM MgCl₂, 1 mM DTT. Cell disruption and preparation of the

Materials and Methods

soluble extract was done as described in chapter 2.14.1. Soluble extracts were loaded on Ni-NTA superflow columns (IBA, Germany) equilibrated with the respective washing buffer. Column washing and elution of the protein was done as described in chapter 2.14.3. Eluted HypE protein was concentrated by centrifugation using a 10K concentrator (Amicon Ultra Ultracel, Millipore), HypF protein was concentrated using a 30K concentrator (Amicon Ultra Ultracel, Millipore). Concentrated proteins were washed three times to reduce the imidazole concentration.

2.15. Determination of protein concentrations

Protein concentrations were determined using the PierceTM BCA Protein Assay Kit (Thermo Scientific, Germany) using Bovine serum albumin as standard.

2.16. SDS-PAGE

SDS-PAGE was used for separation of proteins by their molecular weight under denaturing conditions. For preparation of SDS gels the Mini-PROTEAN[®] Tetra Handcast System (BIO-RAD, Germany) was used. The composition of the two-layered gel is listed in **Table 7**. In the last step, the catalyst TEMED and the radical initiator ammonium peroxodisulfate (APS) were added to start the polymerization reaction.

Table 7. Composition of a denaturing SDS gel. Volumes are for the preparation of one mini gel.

component	Separating gel 12.5 %	Stacking gel
Rotiphorese [®] Gel 30 (37.5 :1)	4.2 ml	1.0 ml
1.5 M Tris-HCl pH 8.8	5.0 ml	-
0.5 M Tris-HCl pH 6.8	-	2.5 ml
H ₂ O	675 µl	1.5 ml
10 % (w/v) SDS	100 µl	50 µl
10 % (w/v) APS	100 µl	50 µl
TEMED	5 µl	10 µl

Materials and Methods

Protein samples for SDS-PAGE were mixed with 4 x SDS sample buffer (250 mM Tris-HCl, pH 6.8, 8 % (w/v) SDS, 40 % (w/v) glycerol, 20 % (w/v) beta-mercaptoethanol, 0.016 (w/v) bromphenol blue) and heated to 95 °C for 5 to 10 min. After denaturation samples were spun down and loaded on the SDS gel together with 5 µl of Precision Plus Protein™ Dual Color Standards (10-250 kDa, BIO-RAD, Germany) as molecular mass size marker.

Electrophoresis was performed in running buffer (25 mM Tris-HCl, 192 mM glycine, 0.1% (w/v) SDS) at 40 mA until the buffer front, visible as colored band, reached the end of the gel. Subsequently, the gel was either stained with Coomassie Brilliant Blue to visualize the protein bands, or used for Western blotting.

2.17. Coomassie staining

SDS gels were stained in a Coomassie staining solution that was prepared as follows: 60-80 mg Coomassie Brilliant Blue G-250 (Serva, Germany) were first dissolved in 1 L H₂O and stirred for 2 – 3 h at room temperature. Then HCl was added to a final concentration of 35 mM. Before adding the staining solution, the SDS gel was washed three times for 2-5 min in H₂O. Before every washing step the H₂O-rinsed gel was warmed up for 30 s (without boiling!) in the microwave oven. The gel was covered with staining solution and warmed up in the microwave oven for 10 s followed by a 10-15 min incubation while gently shaking until the protein bands were visible. Finally, the Coomassie solution was removed and the gel was destained in water to improve the contrast between protein bands and background.

2.18. Western blot

Western blotting was used to identify proteins using polyclonal antibodies raised against the target protein. Proteins were separated via SDS-PAGE followed by an electrophoretic transfer onto a nitrocellulose membrane and an immunostaining procedure to visualize the protein band on the membrane.

Before protein transfer, the SDS gel was rinsed with water and washed twice for 10 min in Tris/glycine buffer (25 mM Tris, 192 mM glycine). The nitrocellulose membrane (BioTrace™, Pall Corporation, Germany) and blotting papers were soaked in buffer and stacked together with the gel in the following order from anode to cathode: blotting paper, membrane, gel and again blotting paper. The electrophoretic transfer was performed at 1.3 A, 25 V for 7 min at

Materials and Methods

room temperature using Trans-Blot®Turbo™ Transfer System (Bio-Rad, Germany). To check if the protein transfer was successful, the membrane was transiently stained with Ponceau S solution (0.2 % in 3 % TCA, Serva, Germany).

To avoid non-specific binding of the antibodies, the membrane was first shaken gently for 1 h in TBST buffer (20 mM Tris-HCl (pH 7.5), 150 mM NaCl, 0.05% (v/v) Tween 20) containing 5 % skim milk powder (Fluka, Germany). After washing three times with TBST buffer, the membrane was incubated for 1 h with the primary antibody (**Table 8**). Afterwards, the membrane was washed again three times for 5 min and incubated for 1 h with the secondary antibody (**Table 8**). To remove unbound secondary antibody, the membrane was washed three times for 5 min in TBST buffer and once in TBS buffer (TBST buffer without Tween 20). To detect Strep tag II fusion proteins, a Strep Tactin alkaline phosphatase conjugate (1:2000 in TBST, IBA, Germany) was used instead of primary and secondary antibodies. For the staining reaction 90 µl BCIP (5-bromo-4-chloro-3-indolyl phosphate (Roth, Germany), 50 mg/ml in 100 % DMSO) and 70 µl NBT (p-nitrotetrazolium blue chloride (AppliChem, Germany), 50 mg/ml in 70 % DMSO) were freshly diluted in 20 ml developing buffer (100 mM Tris-HCl (pH 9.5), 100 mM NaCl, 5 mM MgCl₂). The membrane was incubated in the BCIP/NBT developing buffer in the dark without shaking until the protein bands were clearly visible. The reaction was stopped by rinsing the membrane with H₂O.

Table 8. Antibodies used in this study

Primary antibody	Dilution in TBST	Secondary antibody
α-HypC	1:5000	α-rabbit (1:10000)
α-HypD	1:5000	α-rabbit (1:10000)
α-Strep	1:1000	α-mouse (1:10000)
Strep Tactin alkaline phosphatase conjugate	1:2000	no secondary antibody

2.19. Metal determination

Metal determination of protein samples was performed in cooperation with Jasmin Kurtzke from the group of Prof. Dr. Silke Leimkühler (Universität Potsdam). The metal content of different HypX and HypCD preparations was quantified by ICP-OES. 500 µl protein solution (10 µM) and 500 µl of the respective buffer were each mixed with 500 µl nitric acid (65 %

(v/v)) and incinerated over night at 100 °C. Subsequently, the samples were filled up to 5 ml with ultrapure H₂O and measured in an Optima 2100DV ICP-OES (Perkin-Elmer). Samples were measured in triplicates and analyzed for Fe, Co and Zn in case of HypX and Fe in case of HypCD. The metal concentration was determined by measuring the element-specific emission at different wavelengths. Fe was measured at 238.204, 239.562 and 259.939 nm, Co was measured at 228.616 and 230.786 nm and Zn was measured at 206.200 and 213.857 nm.

2.20. Determination of HypX activity

HypX-dependent CO production was determined using deoxyhemoglobin as reporter. The CO-mediated conversion of deoxyhemoglobin (deoxyHb) to carboxyhemoglobin (HbCO) was detected spectrophotometrically using a Cary[®]50 UV-Vis spectrophotometer (Varian, Agilent, California, USA). The reaction was carried out at 30 °C in 50 mM MOPS pH 7.9, 0.5 mM *N*¹⁰-formyl-THF, 1.25 μM deoxyHb and 0.25 mM sodium dithionite (NaDT). CoA was added to a final concentration of 50 μM. To avoid formation of oxyhemoglobin (Soret band at 415 nm), assays were set up in an anaerobic workstation (Don Whitley Scientific, UK). The reaction took place in 1 ml-cuvettes which were sealed with rubber stoppers before being discharged from the anaerobic workstation for UV-Vis analysis. For kinetic measurements, the absorbance was followed at 419 nm. Activities were calculated using the molar extinction coefficient of HbCO of 192 mM⁻¹ cm⁻¹ (Antonini and Brunori 1971). Additionally, UV-Vis spectra were recorded before and after the addition of HypX to verify the formation of HbCO by the shift of the Soret band from 430 nm to 419 nm and the splitting of the signal at 555 nm.

In case of the E449Q variant of MBP-HypX, 10 mg/ml (final concentration) of BSA were added to the activity assay to prevent precipitation. A control experiment showed that native MBP-HypX showed no significant change in activity in the presence of BSA.

2.21. Determination of *Ht*SH activity

*Ht*SH H₂ oxidation activity was determined spectrophotometrically by measuring the H₂-driven reduction of NAD⁺ to NADH. The reaction was carried out in 50 mM Bis-Tris, pH 6.5, 0.5 mM NiCl₂, 5 mM MgSO₄, with 0.75 mM TCEP, 2 μM FMN and 1 mM NAD⁺ at 50 °C. Before the reaction was set up, the reaction buffer was saturated with H₂ for at least 30 min at 50 °C. 1.9 ml H₂-saturated buffer were transferred into a 3ml cuvette. NAD⁺, TCEP and FMN were

added and the cuvette was sealed with a rubber septum and flushed with H₂ for at least 1 min. The reaction was initiated by addition of an *HtSH* sample and the formation of NADH was followed in a Cary®50 UV-Vis spectrophotometer (Varian, Agilent, USA) at 365 nm. Activities were calculated using a molar extinction coefficient of 3.4 mM⁻¹ cm⁻¹ (Bergmeyer 1975).

2.22. Chemical synthesis of formyl-CoA

Synthesis of formyl-CoA was performed in cooperation with Phillip Pommerening in the group of Martin Oestreich at TU Berlin. Formyl-CoA was synthesized in two consecutive reactions. Product formation and purity of both products was verified by NMR spectroscopy (**Figure S1-S3** in chapter 8 Appendix). ¹H and ¹³C NMR spectra were recorded in CDCl₃ or D₂O on Bruker AV500 and Bruker AV700 instruments. Chemical shifts are reported in parts per million (ppm) and are referenced to the residual solvent resonance as the internal standard (CHCl₃: δ = 7.26 ppm for ¹H NMR and CDCl₃: δ = 77.16 ppm for ¹³C NMR and HDO: δ = 4.79 ppm for ¹H NMR). Data are reported as follows: chemical shift, multiplicity (s = singlet, d = doublet, t = triplet, m = multiplet), coupling constant (Hz), and integration.

The product of the first reaction, *S*-phenyl methanethioate, was synthesized by dissolving formic acid (500 mg, 10.9 mmol, 1.20 equiv.) and thiophenol (996 mg, 9.04 mmol, 1.00 equiv.) in anhydrous CH₂Cl₂ (25 mL). After cooling down the mixture to 0 °C, a solution of 1-ethyl-3-(3-dimethylaminopropyl)carbodiimide hydrochloride salt (EDC·HCl 2.08 g, 10.9 mmol, 1.20 equiv.) in CH₂Cl₂ (25 mL) was added dropwise at 0 °C over a period of 1 h. The solution was then slowly warmed up to room temperature and stirred for 30 h. The reaction was quenched by evaporation of volatiles under reduced pressure. The resulting residue was purified by flash column chromatography on silica gel using cyclohexane/tert-butylmethyl ether = 20/1 as eluent affording *S*-phenyl methanethioate (0.46 g, 3.33 mmol, 37 %) as a yellowish oil.

¹H NMR (500 MHz, CDCl₃): δ/ppm = 7.43–7.52 (m, 5H), 10.24 (s, 1H). ¹³C{¹H} NMR (126 MHz): δ/ppm = 126.3, 129.8, 130.1, 134.4, 190.1.

In the second reaction, CoA (20 mg, 0.026 mmol, 1.0 equiv.) was dissolved in an aqueous solution of NaHCO₃ (0.1 M, 10 mL) under a nitrogen atmosphere and cooled down to 0 °C. *S*-phenyl methanethioate was added in a 5 – 10-fold excess, and the reaction was stirred for 3 h

Materials and Methods

at 0 °C. The reaction was quenched by adding HCl (1M in H₂O) until a pH of approx. 5 was reached. The mixture was washed with Et₂O (3 x 20 mL), and the aqueous phase freeze-dried to yield formyl-CoA (5.2 mg, 0.0018 mmol, 25 %) as a white solid.

¹H NMR (700 MHz, D₂O): δ /ppm = 0.85 (s, 3H), 0.97 (s, 3H), 2.49 (t, J = 6.5 Hz, 1H), 2.52 (t, J = 6.6 Hz, 1H), 2.65 (t, J = 6.6 Hz, 1H), 3.16 (t, J = 6.5 Hz, 1H), 3.36 (t, J = 6.6 Hz, 1H), 3.42 (t, J = 6.5 Hz, 1H), 3.48–3.54 (m, 2H), 3.63 (dd, J = 9.7 Hz, J = 4.3 Hz, 1H), 3.89 (dd, J = 9.7 Hz, J = 4.5 Hz, 1H), 4.06 (s, 1H), 4.25–4.35 (m, 2H), 4.64 (s, 1H), 4.87–4.94 (m, 2H), 6.27 (d, J = 5.8 Hz, 1H), 8.49 (s, 1H), 8.72 (s, 1H), 10.19 (s, 1H). The N–H and O–H signals could not be detected.

2.23. Quantification of CoA and formyl-CoA

The CoA content of purified MBP-HypX was determined using a CoA Assay Kit (Sigma-Aldrich) specific for free CoA. Protein samples were heat-precipitated for 10 min at 70 °C. After centrifugation, the concentration of free CoA in the supernatant was determined spectrophotometrically by following the protocol provided by the manufacturer. For quantification of formyl-CoA in a mixture composed of formyl-CoA and free CoA, we measured spectrophotometrically the absorbance at 260 nm with an extinction coefficient of 12.7 mM⁻¹ cm⁻¹. The extinction coefficient was previously determined by measuring the absorbance at 260 nm of solutions with different CoA concentrations (0.01 – 1.00 mM). The concentration of formyl-CoA was calculated by subtracting the concentration of free CoA from the total CoA concentration.

Another, less specific method to quantify the CoA content of purified HypX is Ellman's test. Ellman's reagent (5,5'-dithiobis-(2-nitrobenzoic acid) or DTNB) reacts with free thiols producing 2-nitro-5-thiobenzoate (TNB⁻). In neutral and alkaline pH, TNB⁻ deprotonates to TNB²⁻ which has a yellow color and can be spectrophotometrically quantified by measuring the absorbance at 412 nm. The extinction coefficient at 412 nm of 10.1 mM⁻¹ cm⁻¹ was determined by measuring solutions with different CoA concentrations (0.01 – 1.00 mM). 180 μ l reaction buffer (100 mM Tris-HCl, pH 8.0 at RT containing 0.2 mM DTNB) were mixed with 20 μ l sample or CoA standard and incubated for 15 min at RT. Purified MBP-HypX was denatured and the CoA content of the supernatant was determined.

2.24. Fourier-transform infrared spectroscopy (FTIR)

FTIR was performed in cooperation with Catharina Kulka who is member of the group of Ingo Zebger and Peter Hildebrandt (TU Berlin) and Giorgio Caserta from our group. FTIR spectra were recorded with a resolution of 2 cm^{-1} on a Bruker Tensor 27 FTIR spectrometer (Bruker Optik GmbH, Germany) equipped with a liquid nitrogen-cooled mercury cadmium telluride (MCT) detector. Protein samples of a minimum concentration of $200\text{ }\mu\text{M}$ were loaded into a gas-tight IR cell (volume $\sim 7\text{ }\mu\text{l}$, path length: $50\text{ }\mu\text{m}$) equipped with CaF_2 windows. After installing the IR cell in the FTIR spectrometer, the sample compartment was purged with dried air. Spectra were taken at $10\text{ }^\circ\text{C}$. For every measurement, a reference spectrum with the respective buffer was taken and subtracted from the spectrum of the sample. Spectra analysis was performed using the Bruker OPUS software. Spectra are either displayed as baseline-corrected absorbance spectra or second derivative spectra, where the maximum of an absorption band appears as a sharp negative peak.

2.25. Resonance Raman Spectroscopy

Resonance Raman (RR) spectroscopy was performed in cooperation with Catharina Kulka who is member of the group of Ingo Zebger and Peter Hildebrandt (TU Berlin). RR spectra were recorded with a spectral resolution of 2 cm^{-1} using a confocal Raman spectrometer (Lab Ram HR-800, Jobin Yvon) equipped with liquid-nitrogen and Peltier-element cooled charge coupled device (CCD) cameras. Spectra were probed with excitation line of 458 nm using Argon and Krypton ion continuous wave lasers. The laser power was set to $1 - 4\text{ mW}$, focused on a spot of ca. $2\text{ }\mu\text{m}$ in diameter. The temperature of the sample was set to 80 K throughout the measurement using a Linkam Cryostage THMS600 cryostat.

2.26. UV-Vis spectroscopy

UV-Vis spectra were recorded at room temperature using a Cary[®]300 UV-Vis spectrophotometer (Varian, Agilent, USA).

2.27. Crystallization trials with Strep-*HtHypX*

To determine the structure of a protein by X-ray diffraction the protein of interest needs to form high-quality crystals suitable for X-ray diffraction analysis. For transformation from the soluble into the crystalline phase, the solubility of the protein will be decreased by increasing the protein concentration or by increasing the concentration of a precipitant. For this purpose the sitting-drop vapor diffusion method was used (Benvenuti and Mangani 2007). In this study, we aimed at determining the structure of Strep-*HtHypX*. Crystallization screenings were performed in cooperation with Holger Dobbek and Berta Martins at Humboldt-Universität zu Berlin. Strep-*HtHypX* was purified via affinity chromatography and subsequent size-exclusion chromatography. Freshly prepared protein was used in concentrations ranging between 8 to 18 mg/ml. The following kits were used to test more than 700 different conditions in 96-well crystallization plates, each at 18 and 10 °C: ProPlex HT-96 (moleculardimensions.com), JCSG-plus™ HT-96 (moleculardimensions.com), PACT premier™ HT96 (moleculardimensions.com), MemGold HT-96 (moleculardimensions.com), Structure Screen 1 & 2 HT-96 (moleculardimensions.com), Wizard CRYO 1 & 2 (Rigaku), The Stura Footprint Screen™ + MacroSol™ HT-96 (moleculardimensions.com), SaltRX HT™ (Hampton Research). None of the chosen conditions resulted in crystal growth.

2.28. Cleavage of MBP-*HtHypX* fusion protein with factor Xa

Factor Xa cleavage of MBP-*HtHypX* fusion protein was carried out in 100 mM Tris-HCl, pH 8.0 at 25 °C, 500 mM NaCl, 10 mM CaCl₂. 50 µg of MBP-*HtHypX* were mixed with 1 µg factor Xa and incubated at RT for up to several days. To increase the rate of cleavage, the amount of factor Xa was increased to a ratio of 4 % (w/w) the amount of fusion protein, SDS was added at concentrations of 0.005, 0.025 and 0.05 % and the reaction mix was incubated at 30 and 37 °C. Cleavage of the fusion protein was checked by SDS-PAGE.

2.29. Determination of ATPase activity of HypE, HypF and HypCD

ATPase activity of HypE, HypF and HypCD was tested in a coupled assay using pyruvate kinase (PK) and lactate dehydrogenase (LDH) by following the conversion NADH to NAD⁺. ADP, the product of the ATP hydrolysis catalyzed by HypE, HypF or HypCD (reaction 1), is used by PK together with phosphoenyl pyruvate (PEP) to form pyruvate and ATP (reaction 2).

Materials and Methods

The resulting pyruvate is used in a third reaction by LDH forming lactate, while converting NADH to NAD⁺ (reaction 3). The oxidation of NADH was monitored spectrophotometrically as a decrease in absorbance at 340 nm using a Cary[®]50 UV-Vis spectrophotometer (Varian, Agilent, California, USA).

- (1) HypE/F/CD ATP → ADP + P_i
- (2) PK ADP + PEP → pyruvate + ATP
- (3) LDH pyruvate + NADH + H⁺ → lactate + NAD⁺

The reaction was carried out at 25 °C in 100 mM Tris-HCl pH 7.5 at 25 °C, 2.5 mM MgCl₂, 1 mM PEP, 0.3 mM NADH. PK and LDH were added in a final amount of 4 U PK and 3 U LDH. To test the coupled activity of PK-LDH, 1 mM ADP was added as substrate for PK and the NADH to NAD⁺ conversion, catalyzed by LDH, was followed at 340 nm. Activities were calculated using a molar extinction coefficient of 6.3 mM⁻¹ cm⁻¹ (Bergmeyer 1975). To test the ATPase activities of HypE, HypF, and HypCD, the assay contained 1 mM ATP and no ADP. Before HypE, HypF or HypCD were added to the reaction, an unspecific activity due to contamination of ADP in the ATP solution was observed. After the unspecific reaction was ceased, the Hyp proteins were added. HypE and HypF activity was tested in the absence and presence of 1 mM carbamoyl phosphate.

2.30. Reconstitution of HypCD with (PPh₄)[Fe(CO)₂(CN)₂(μ-pdt)K] complex

To test whether apo-HypCD accepts a chemical mimic of the Fe(CN)₂(CO) moiety, it was reconstituted with (PPh₄)[Fe(CO)₂(CN)₂(μ-pdt)K] complex. The complex was synthesized by Siad Wolff in the group of Christian Limberg at HU Berlin. All reconstitution steps were carried out under anoxic conditions in an anaerobic workstation (Don Whitley Scientific, UK). The reconstitution protocol was adopted from an established reconstitution protocol (Sven Hartmann, personal communication). Therefore, the purification protocol of apo-HypCD was modified; 50 mM KPO₄, pH 7.3, 150 mM NaCl was used as purification buffer (see chapter 2.14.3). Approximately 3 mg purified apo-HypCD were incubated with 2 mM NaDT for 15 min. The synthetic complex was dissolved in DMSO and added to the reduced apo-HypCD protein in a 10-fold molar excess. After 1 h incubation, the reconstitution mix was loaded on an illustra[™] NAP-5 column packed with a Sephadex[™] G-25 resin (GE healthcare, Germany)

to remove unbound synthetic complex. The eluted protein was concentrated using Ultra Centrifugal Filter Units (Amicon Ultra Ultracel 10K, Millipore) and subjected to IR spectroscopic analysis.

2.31. Reconstitution of HypCD with Fe

Since as-purified apo-HypCD presumably does not contain the precursor Fe necessary for $\text{Fe}(\text{CN})_2(\text{CO})$ assembly, it was reconstituted with Fe. Reconstitution of apo-HypCD was carried out in an anaerobic workstation (Don Whitley Scientific, UK). 2 – 7 mg of HypCD were incubated with 5-fold molar excess of $\text{Fe}(\text{II})(\text{NH}_4)_2(\text{SO}_4)_2$ in the presence of 50-fold molar excess of DTT for 1.5 – 2 h. Following the reconstitution, the mixture was centrifuged, and the supernatant was run on a Superdex 200 Increase 10/300 GL column to remove excess Fe. The column was equilibrated and run with 100 mM Tris-HCl, pH 8 at 4 °C, 100 mM NaCl. Size-exclusion chromatography was carried out with an ÄKTA pure system (GE healthcare, Germany) at a flow rate of 0.5 ml/min. Eluted protein was collected in 0.4 ml fractions. Elution of the protein was monitored at 280 nm and 420 nm at which the [4Fe-4S] cluster of HypD absorbs. Fractions containing HypCD were pooled and concentrated by centrifugation using Ultra Centrifugal Filter Units (Amicon Ultra Ultracel 10K, Millipore). To confirm the successful reconstitution of HypCD, the Fe content of as-purified and reconstituted HypCD was determined via ICP-OES (see chapter 2.19).

2.32. Chemical *in vitro* assembly of the $\text{Fe}(\text{CN})_2(\text{CO})$ moiety with KCN and CO

For the chemical *in vitro* assembly assay of the $\text{Fe}(\text{CN})_2(\text{CO})$ moiety, Fe-reconstituted apo-HypCD_{strep} was used as basis for the addition of CN^- and CO ligands derived from KCN and CO gas. The assembly assay was performed under anoxic conditions in an anaerobic workstation (Don Whitley Scientific, UK). Apo-HypCD_{strep}(Fe) was incubated for 30 min with 10-fold molar excess of NaDT and 10-fold molar excess of KCN. The sample was loaded into an IR cell and the IR spectrum was recorded (see chapter 2.24). As controls, non-reconstituted apo-HypCD, BSA, and the buffer were treated in the same way and IR spectra were recorded. For the addition of the CO ligand, a highly concentrated sample (~ 0.8 mM) of apo-HypCD_{strep}(Fe) was reduced with a 10-fold molar excess of NaDT under anoxic conditions inside an anaerobic workstation. The sample was sealed with a gas-tight rubber septum and

Materials and Methods

removed from the anaerobic workstation where it was purged for 30 min with CO gas before it was 1:2 diluted with CO-saturated buffer. Under constant CO gas flow, the sample was loaded into the IR cell.

3. Results

3.1. *HtSH* – a thermostable NAD⁺-reducing [NiFe]-hydrogenase from *H. thermoluteolus*

Recent IR spectroscopic investigation of as-isolated, aerobically- and NAD⁺-oxidized *HtSH* revealed an exceptional spectral pattern that is remarkably different from those of other NAD⁺-reducing [NiFe]-hydrogenases (Preissler et al. 2018b). The spectrum showed three distinct CO stretching vibrations separated by approximately 30 cm⁻¹, whereas the closely related enzyme from *R. eutropha* (*ReSH*), for example, exhibited just one intense CO stretching band in addition to a weak stretching band at a distance of 15 cm⁻¹ (Horch et al. 2015b; Happe et al. 2000; van der Linden et al. 2006). Two of the CO stretching bands in the *HtSH* spectrum were assigned to a Ni_r-B-like state and the Ni_r-SI state that are also observed in *ReSH* and other NAD(P)⁺-reducing [NiFe]-hydrogenases (Horch et al. 2012; van der Linden et al. 2006; Horch et al. 2010; Germer et al. 2009; Horch et al. 2015b; Greene et al. 2015). The third CO band was found at an exceptionally high stretching frequency at 1993 cm⁻¹, which has not been observed for any other [NiFe]-hydrogenase. It is proposed to correspond to an unusual active site geometry or coordination (Preissler et al. 2018b). Interestingly, in the oxidized state, the crystal structure of the *HtSH* revealed an unprecedented coordination geometry of the active site. The Ni is coordinated by three cysteines – all of which bridging the Ni and Fe – in addition to one terminal cysteine and the carboxy group of Glu32 acting as bidentate ligand (Shomura et al. 2017). In the reduced state, however, the [NiFe] active site shows the standard configuration with Ni being coordinated by two bridging and two terminal cysteines (see chapter 1.1.5).

By poisoning *HtSH* to different defined redox conditions, we aimed to elucidate the state represented by the CO stretching band at 1993 cm⁻¹ in more detail. Furthermore, to combine previous structural and spectroscopic findings and to investigate whether the unusually high CO stretching vibration at 1993 cm⁻¹ corresponds to the active site configuration with Glu32 coordinating the Ni, different variants carrying amino acid exchanges for Glu32 were generated and investigated biochemically and spectroscopically. IR spectroscopic measurements and corresponding data analysis were carried out by Catharina Kulka from the group of Ingo Zebger.

Results

3.1.1. The oxidized active site species at 1993 cm^{-1} accumulates upon O_2 exposure

HtSH was heterologously produced in *R. eutropha* and purified via Strep-Tactin affinity chromatography and subsequent size-exclusion chromatography as described previously (Preissler et al. 2018b). Size-exclusion chromatography was performed to obtain homogeneous protein preparations with high purity, optimized subunit stoichiometry, and high activity suitable for spectroscopic characterization. Purity and subunit stoichiometry were estimated by SDS-PAGE and activity assays. A typical SDS-PAGE gel of purified *HtSH* after size-exclusion chromatography is shown in **Figure 10**. Fractions 14 – 16 showed the highest activity and were pooled and subjected to spectroscopic analysis. The average specific activity for *HtSH* purified via affinity chromatography is $(14.4 \pm 3.0)\text{ U/mg}$ which could be increased up to $(42.3 \pm 22.1)\text{ U/mg}$ after size-exclusion chromatography.

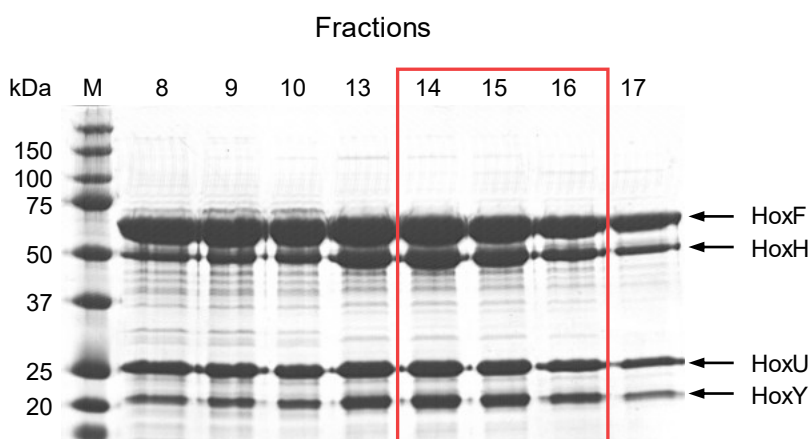


Figure 10. SDS gel of *HtSH* purified via size-exclusion chromatography. A volume of $10\ \mu\text{l}$ of each fraction were separated on a 12.5 % SDS gel, which was subsequently stained with Coomassie brilliant blue. The fraction numbers are indicated on top of each lane. The four *HtSH* subunits HoxF (64 kDa), HoxH (57 kDa), HoxU (26 kDa) and HoxY (21 kDa) are indicated by arrows. Lane M contains a protein standard with the corresponding molecular masses indicated on the left-hand side. Fractions 14 – 16 (red frame) were pooled and used for subsequent IR spectroscopic analysis.

It has been shown previously that the oxidized species reflected by the 1993 cm^{-1} band can be activated under reducing conditions indicating that it is not related to irreversible oxidative damage (Preissler et al. 2018b). To gain detailed information on the reversibility of the 1993 cm^{-1} species, we followed the slow aerobic oxidation of previously reduced *HtSH* by IR spectroscopy (**Figure 11**). Therefore, a NADH/TCEP/ H_2 -reduced sample was placed in the IR cell and aerobically oxidized by letting air diffusing slowly into the IR cell. The setup allowed

Results

us to follow time-dependent redox changes over several hours. The resulting spectra are shown as second derivatives, where an absorbance maximum appears as sharp negative peak. The starting point was the IR spectrum of freshly reduced *HtSH*. It exhibited four fairly well-separated CO stretching bands at 1934, 1943, 1958 and 1971 cm^{-1} , corresponding to the catalytically active $\text{Ni}_a\text{-SR}''$, $\text{Ni}_a\text{-SR}'$, $\text{Ni}_a\text{-SR}$ and $\text{Ni}_a\text{-C}$ states, respectively (Preissler et al. 2018b). With continuing O_2 exposure, these bands disappeared, and new ones emerged. After 11 h, a band at 1951 cm^{-1} appeared temporarily, which was assigned to the $\text{Ni}_a\text{-SI}$ state (Preissler et al. 2018b). After 20 h, three bands including the high frequency band at 1993 cm^{-1} are developed that were also observed in the as-isolated *HtSH* spectrum. The two bands at 1936 and 1966 cm^{-1} (in the as-isolated spectrum at 1964 cm^{-1}) were assigned to the catalytically inactive $\text{Ni}_r\text{-SI}$ and $\text{Ni}_r\text{-B}$ -like resting states (Preissler et al. 2018b). Upon further O_2 exposure, the ratio of the intensity of the peaks changed, and the 1993 cm^{-1} band became the dominant species while the band at 1936 cm^{-1} decreased. This indicates that the active site modification resulting in the unusually high frequency at 1993 cm^{-1} can be produced upon aerobic oxidation. Furthermore, it has been shown that anaerobic oxidation with $[\text{Fe}(\text{CN})_6]^{3-}$ of *HtSH* purified from its natural host, *H. thermoluteolus*, did not result in the formation of the 1993 cm^{-1} species whereas aerobic oxidation with O_2 does (Catharina Kulka and Charlotte Wiemann, personal communication), supporting the assumption that the 1993 cm^{-1} species is formed upon aerobic but not anaerobic oxidation. It is likely that the structural modification reflected by the 1993 cm^{-1} band corresponds to the active site configuration observed in the crystal structure of *HtSH* with Glu32 coordinating the Ni. This unprecedented coordination was only observed in air-oxidized crystals, which would be in line with the conclusion that the 1993 cm^{-1} species is induced upon O_2 exposure.

Noticeably, the signal intensity of the active site-related IR bands decreased over time while the protein concentration – according to the intensity of the amide II band – remained the same, indicating that the $\text{NiFe}(\text{CN})_2(\text{CO})$ moiety is not stable over longer time under these conditions.

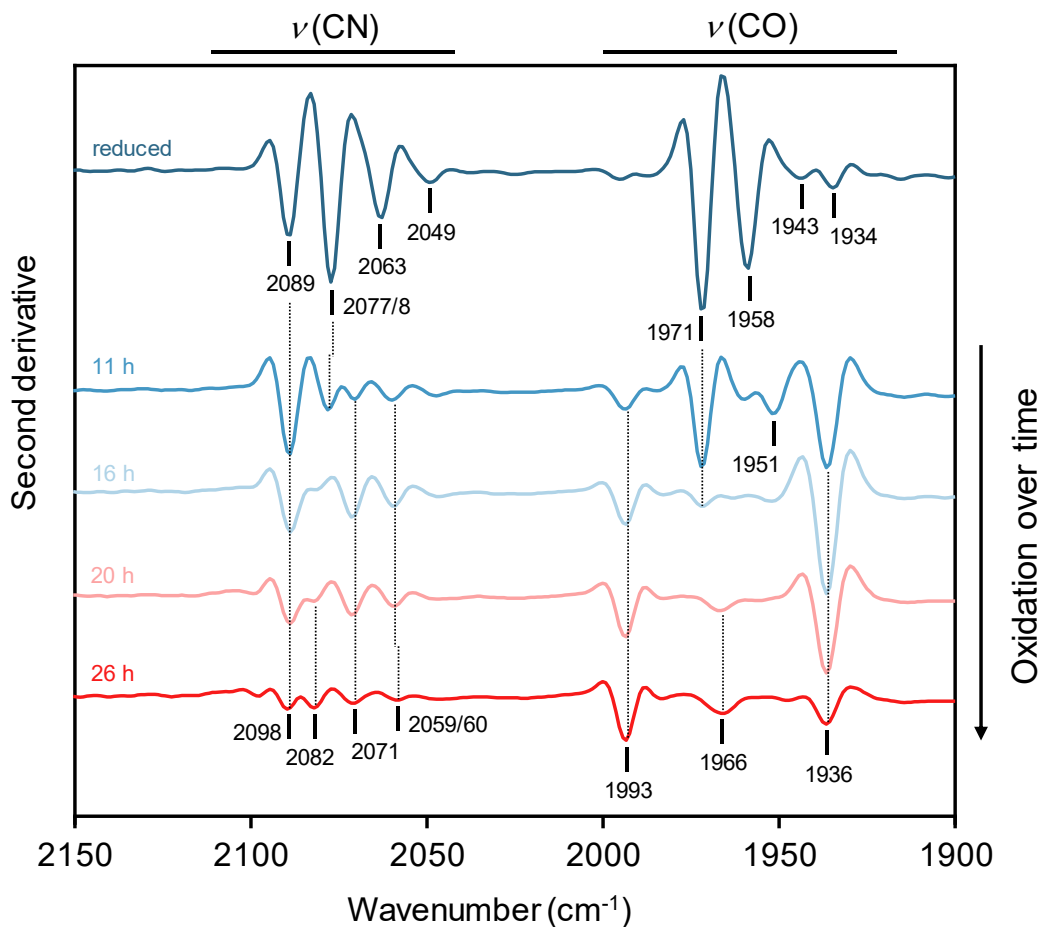


Figure 11. Aerobic oxidation of reduced *HtSH* over time. The incubation time is indicated on the left of each spectrum and increases from top to bottom. Starting point was the spectrum of *HtSH* reduced with TCEP, NADH and H_2 . Slow aerobic oxidation was achieved by diffusion of air into the IR cell while continuously recording spectra. Spectra are normalized to the protein concentration and shown as second derivative.

3.1.2. The CO stretching frequency at 1993 cm^{-1} reflects an active site configuration with Glu32 coordinating the Ni

To test whether the 1993 cm^{-1} species can be assigned to the active site configuration where Glu coordinates the Ni, three *HtSH* variants were created by exchanging Glu32 for Gln, Ala and Asp in the large subunit HoxH. The respective mutations were introduced by site-directed mutagenesis using plasmid pLL2000, encoding Strep-tagged native *HtSH* as template (Preissler et al. 2018b). *R. eutropha* strain HF1054 was used for heterologous overproduction, in which the native SH genes *hoxFUYHWI* and *hoxG*, encoding the large subunit of membrane-bound hydrogenase (MBH), were deleted (Preissler et al. 2018b). *HtSH* variants were purified

Results

by Strep-Tactin affinity chromatography, and the purity was checked by SDS-PAGE (**Figure 12**).

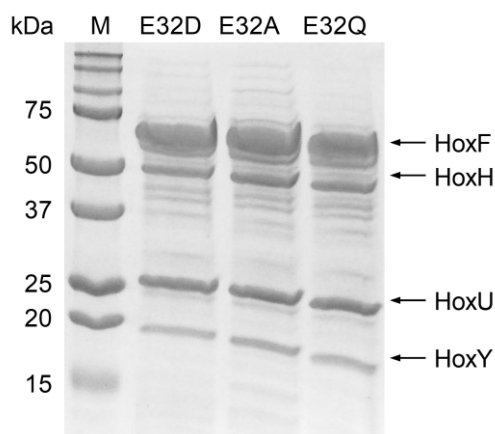


Figure 12. SDS-PAGE gel of purified *HtSH* variants E32D, E32A and E32Q. 12 μg of each *HtSH* variant were separated on a 15 % SDS gel and visualized by Coomassie staining. Lane M contains a protein standard with the corresponding molecular masses indicated on the left-hand side. The four subunits HoxF, HoxH, HoxU and HoxY are indicated with arrows.

First, the *HtSH* variants were analyzed by IR spectroscopy. If the coordination of Ni with the Glu32 carboxyl group as ligand results in the 1993 cm^{-1} CO stretching band, the IR spectra of the variants E32A and E32Q, should lack the 1993 cm^{-1} band because they lack a carboxyl group side chain. Aspartate, with its carboxyl group side chain might be able to restore the Ni coordination similar to the native glutamate residue, resulting in a high CO stretching frequency. All spectra were recorded in the as-isolated, NAD^+ -oxidized state because the Glu-Ni coordination and the 1993 cm^{-1} band were only observed in an oxidized state. The variants E32A and E32Q exhibited similar spectra that, however, were completely different compared to the spectrum of native *HtSH* (**Figure 13**), indicating that their corresponding active site geometries deviated considerably from that of native *HtSH*. Moreover, there is no high frequency CO signal in the 2000 cm^{-1} region indicating that the coordination of Ni by the Glu32 carboxyl side chain indeed results in the 1993 cm^{-1} band. However, the spectrum of the variant E32D showed three bands, including one at 1998 cm^{-1} , which are comparable to the frequencies of the signals in native *HtSH*. This suggests that the active site architecture and redox state varied only slightly to that of native *HtSH*. The exchange of Glu for Asp resulted in a shortening of the side chain but might still enabled coordination of the Ni by the carboxyl group. These results point out, that the signal at 1993 cm^{-1} indeed reflects an active site

Results

geometry with the Glu32 carboxyl group coordinating Ni. Interestingly, when normalized to the protein concentration, all three variants showed decreased intensities of the CO and CN bands in the absorbance spectrum when compared to those of native *HtSH*. This observation has been reported before and might point out a role of the conserved E32 in the assembly or incorporation of the NiFe(CN)₂(CO) active site (Greene et al. 2016).

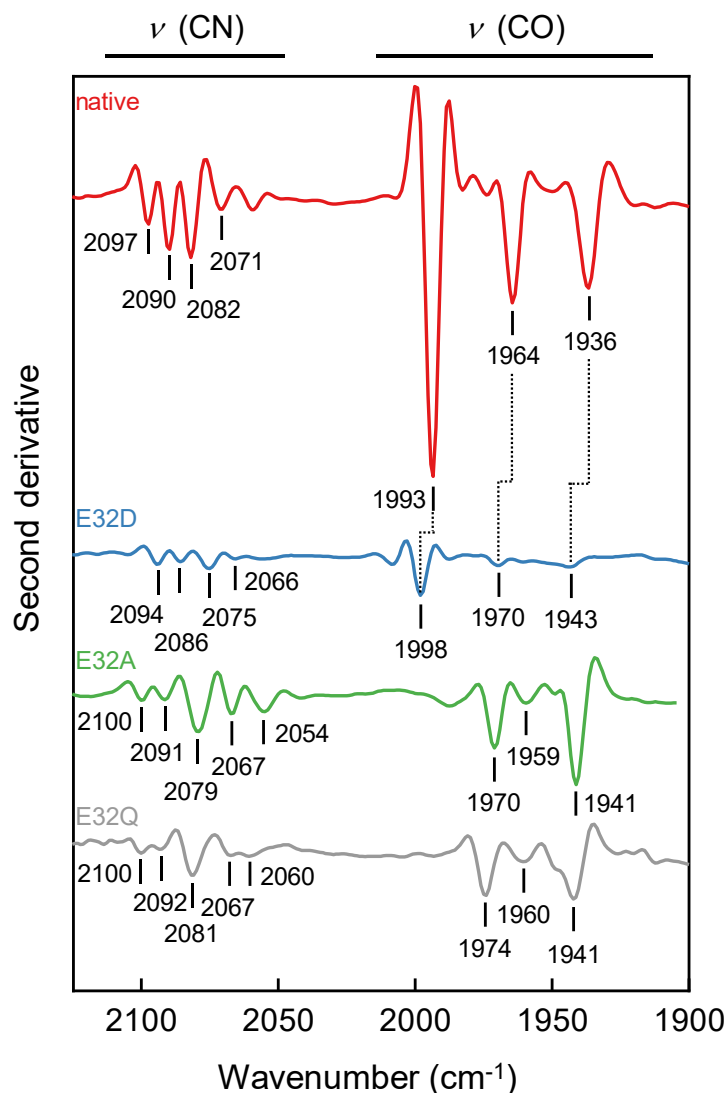


Figure 13. IR spectra of native *HtSH* (red) and *HtSH* variants E32D (blue), E32A (green) and E32Q (grey). All spectra are recorded in the as-isolated oxidized state and are shown as second derivative.

Next, the H₂ oxidation activity of the *HtSH* variants was measured as the H₂-driven reduction of NAD⁺ to NADH at 50 °C (**Figure 14**). All three variants showed drastically reduced activities ranging between 0.4 to 10 % of that of native *HtSH* (**Table 9**). Glu32 is highly conserved in [NiFe]-hydrogenases and is proposed to be involved in H⁺ transfer from the active

Results

site to the protein surface. In the course of H₂ oxidation the terminal, Ni-coordinating cysteine close to Glu32 accepts an H⁺, which, in the next step is transferred to Glu32. Exchanges of this conserved glutamate residue interrupts H⁺ transfer and results in a reduced or abolished enzyme activity as shown previously for other [NiFe]-hydrogenases (Dementin et al. 2004; Adamson et al. 2017b; Greene et al. 2016; Gebler et al. 2007). Among the three *Ht*SH variants, E32D showed the highest activity. Both, aspartate and glutamate have an acidic side chain that can be protonated/deprotonated and therefore participate in H⁺ transfer. Due to the shorter side chain of aspartate, the exchange of glutamate against aspartate might result in a reduced H⁺ transfer and a lower H₂ oxidation activity of the E32D variant. Since the side chains of alanine and glutamine cannot be protonated, they cannot mediate H⁺ transfer. However, the activity of the E32A variant is still 10-times higher compared to the one of the variant E32Q. The small side chain of alanine might leave enough space for a water molecule to act as alternative proton acceptor. Glutamine, on the other hand, has a side chain similar in size to that of glutamate, leaving no space for a water molecule to participate in H⁺ transfer. It must be noted, that the reduced NiFe(CN)₂(CO) moiety loading of the variants, deduced from the IR spectra, may also account for the reduced enzymatic activity of the variants.

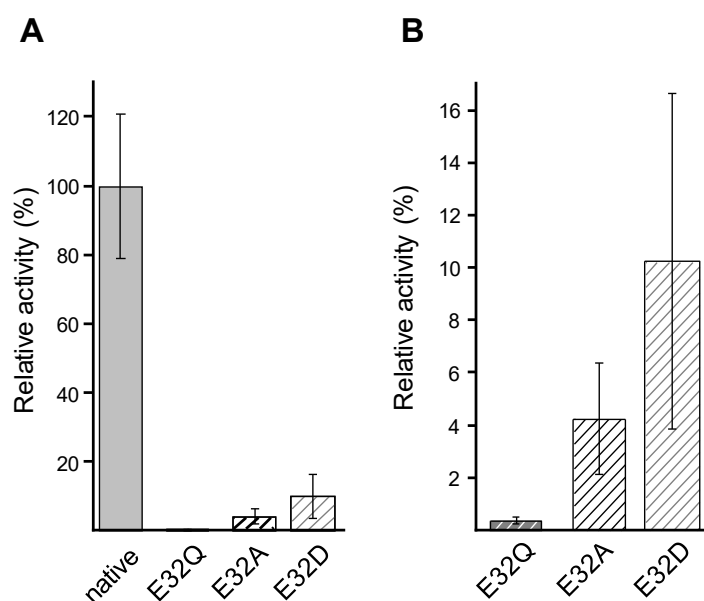


Figure 14. H₂-oxidation activity of Glu32 variants. The H₂-dependent reduction of NAD⁺ to NADH was measured at 50 °C in H₂-saturated buffer. (A) Activity of native *Ht*SH and variants E32Q, E32A and E32D, (B) activity of variants E32Q, E32A and E32D. A specific activity of 14.4 ± 3.0 U/mg measured for native *Ht*SH corresponds to 100 %.

Results

Table 9. H₂-oxidation activities of *Hs*SH variants carrying exchanges for Glu32 in the large subunit HoxH.

Sample	Specific activity (U/mg)	Relative activity (%)
native	14.4 ± 3.0	100.0 ± 20.9
E32Q	0.06 ± 0.02	0.4 ± 0.1
E32A	0.61 ± 0.30	4.3 ± 2.1
E32D	1.47 ± 0.92	10.2 ± 6.4

3.2. HypCD – the central scaffold for Fe(CN)₂(CO) moiety assembly

According to the current model, the HypCD complex is the central construction site for the assembly of the Fe(CN)₂(CO) moiety. The CO and CN⁻ ligands are supposed to be attached to an Fe jointly coordinated by HypC and HypD (Blokesch et al. 2004b; Watanabe et al. 2007). Little is known so far about the detailed mechanism and the order of ligand attachment. It is also unknown how the precise stoichiometry of two CN⁻ and one CO ligand is maintained. Furthermore, the origin of the precursor Fe and its coordination to the HypCD complex, as well as the coordination of the assembled Fe(CN)₂(CO) moiety, are not entirely unraveled. The final transfer of the Fe(CN)₂(CO) moiety into the hydrogenase apo-large subunit is another process that is not yet fully understood.

To obtain a better understanding of the HypCD-dependent maturation process, purified *E. coli* HypCD was analyzed using different spectroscopic techniques. Various maturation experiments were performed using Fe-reconstituted apo-HypCD to study the ligand attachment. HypE and HypF were purified and tested for their functionality, for their future use in enzymatic *in vitro* reconstitution assays. Apo-HypCD was reconstituted with a synthetic Fe(CN)₂(CO) moiety mimic and the first preliminary studies for the transfer of the Fe(CN)₂(CO) moiety to the apo-large hydrogenase subunit were performed. The results presented in this chapter are preliminary and form the basis for following investigations.

3.2.1. Spectroscopic characterization of *E. coli* HypCD

The HypCD complex from *E. coli* was homologously produced in *E. coli* Rosetta™(DE3) transformed with the already established plasmids pThypDEFCstrep and pThypDCstrep (Blokesch et al. 2004b). It was shown previously, that co-expression of *hypCD* together with *hypEF* from plasmid pThypDEFCstrep leads to the formation of holo-HypCD complex, carrying the Fe(CN)₂(CO) moiety, whereas expression of *hypCD* alone (pThypDCstrep) results in the accumulation of apo-HypCD, free of diatomic ligands (Bürstel et al. 2012; Soboh et al. 2012). A Strep-tag II C-terminally fused to HypC enabled purification of HypCD_{strep} via Strep-Tactin affinity chromatography. To find the best conditions for protein production, cell culture and protein expression were tested under aerobic and anaerobic conditions. No substantial difference in purity (**Figure 15 A, B**) or protein yield was observed between proteins purified from aerobically or anaerobically cultivated cells. An amount of 1 g of cells (wet weight) yielded in average (0.38 ± 0.29) mg or (0.30 ± 0.20) mg protein for anaerobically or aerobically cultivated cells, respectively. However, protein yield could be significantly

Results

increased up to (2.67 ± 0.81) mg per 1 g of cells (wet weight) when changing from standard Strep-Tactin Superflow to Strep-Tactin Superflow high capacity columns (IBA, Germany). Holo-HypCD_{strep} purified from cells expressing pThypDEFcstrep under anaerobic and aerobic conditions contained substoichiometric amounts of HypE which is reasonable as it forms a ternary complex with HypCD to transfer the CN⁻ ligands (Blokesch et al. 2004b; Jones et al. 2004). The identity of HypC and HypD was verified using specific antibodies raised against HypC or HypD (**Figure 15 C**).

Since aerobic cultivation was easier to handle and yielded more cells and therefore more protein, all further experiments were performed with HypCD_{strep} purified from aerobically cultivated cells.

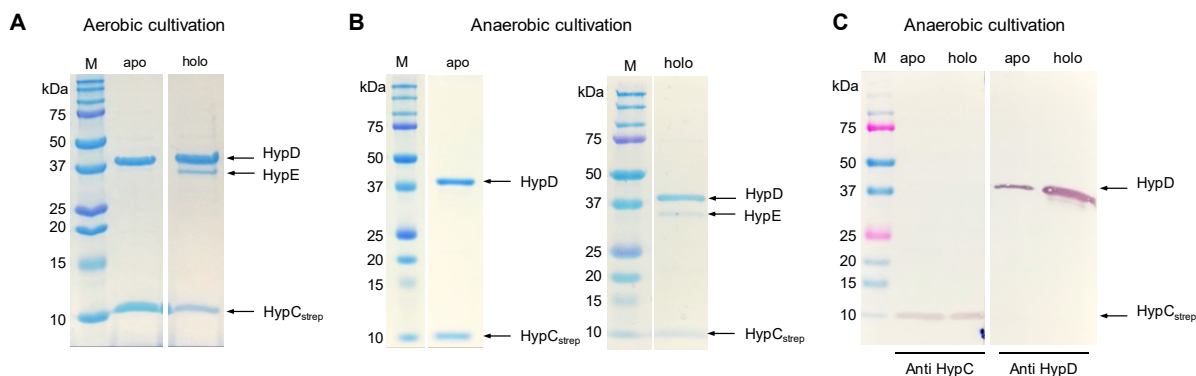


Figure 15. SDS-PAGE analysis and immunological detection of apo-HypCD and holo-HypCD purified from aerobically or anaerobically grown recombinant *E. coli* cells harboring plasmids pThypDCstrep or pThypDEFcstrep. (A) 4 μ g of each, apo- and holo-HypCD purified from aerobically cultivated cells and (B) 3 μ g each, apo- and holo-HypCD purified from anaerobically cultivated cells were separated on a 12.5 % SDS gel and stained with Coomassie brilliant blue. (C) 3 μ g each, apo- and holo-HypCD purified from anaerobically cultivated cells were separated on a 12.5 % SDS gel and detected by specific antibodies against HypD and HypC (C). Lanes containing apo-HypCD_{strep} are labeled “apo”, lanes containing holo-HypCD_{strep} are labeled “holo”. Lane M contains a protein standard with the corresponding molecular masses on the left-hand side. The arrows indicate the position of HypD, HypE and HypC_{strep} with theoretical molecular masses of 41 kDa, 35 kDa and 11 kDa (including Strep-Tag), respectively.

IR spectroscopy. Apo- and holo-HypCD_{strep} purified from aerobically cultivated cells were analyzed by IR spectroscopy to check for the absence or presence of the Fe(CN)₂(CO) moiety (**Figure 16**). The absorbance spectrum of holo-HypCD_{strep} showed four major bands. Two of them appeared in the CN⁻ region at 2099 and 2074 cm⁻¹. The other two bands appeared at 1961 and 1952 cm⁻¹ and correspond to CO stretching vibrations. These were similar band positions as previously reported for holo-HypCD purified from cells cultivated under aerobic and as well anaerobic conditions (Bürstel et al. 2012; Soboh et al. 2012). The presence of two CO peaks

Results

might be explained by the formation or cleavage of disulfide bonds close to the $\text{Fe}(\text{CN})_2(\text{CO})$ moiety binding site which might affect the electronic properties of the $\text{Fe}(\text{CN})_2(\text{CO})$ moiety resulting in different CO stretching vibrations (Bürstel et al. 2012). The spectra of apo-HypCD_{strep}, in contrast, exhibited no CO or CN^- signals (**Figure 16**).

To test the effect of NaDT on the $\text{Fe}(\text{CN})_2(\text{CO})$ moiety, holo-HypCD_{strep} was incubated with a 10-fold molar excess of NaDT. No changes in the IR spectrum were observed (**Figure 16**), indicating that the Fe of the $\text{Fe}(\text{CN})_2(\text{CO})$ moiety cannot be reduced and might persist in the Fe(II) state, as it has been described for the $\text{NiFe}(\text{CN})_2(\text{CO})$ moiety in the active site of [NiFe]-hydrogenases (Caserta et al. 2020).

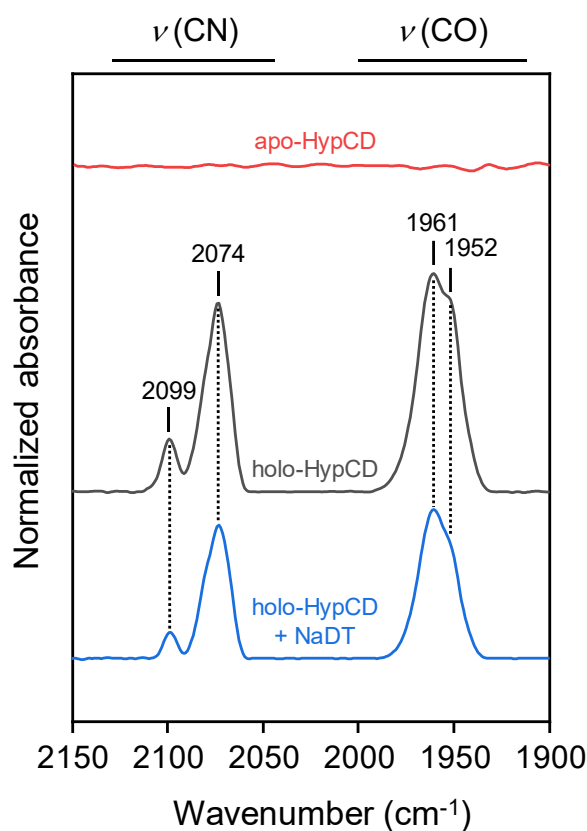


Figure 16. IR spectra of apo-HypCD (red spectrum), holo-HypCD (grey spectrum) and holo-HypCD treated with NaDT (blue spectrum). Spectra are normalized to the protein concentration.

UV-Vis spectroscopy. To confirm the presence of the [4Fe-4S] cluster in HypD, holo-HypCD_{strep} and apo-HypCD_{strep} were analyzed by UV-Vis spectroscopy (**Figure 17**). The spectra of both samples showed a broad maximum at 405 – 410 nm characteristic for [4Fe-4S] clusters demonstrating that the [4Fe-4S] cluster was present in the preparations. The intensity

Results

of the maximum at 405 – 410 nm, however, was higher in the spectrum of holo-HypCD_{strep}. This might indicate a greater population of reduced [4Fe-4S] clusters in the apo-HypCD_{strep} preparation compared to the holo-HypCD_{strep} preparation. It must be noted, that both proteins were purified via affinity chromatography which did not reveal stoichiometric HypCD complex but also free HypC protein, since the Strep-tag was fused to the C-terminal end of HypC. Thus, the observed differences in the intensity of the absorbance corresponding to the [4Fe-4S] cluster might be due to different HypCD ratios in the preparations. Interestingly, the spectrum of holo-HypCD_{strep} showed a higher absorbance in the region between 350 – 400 nm than that of apo-HypCD_{strep}. This additional absorbance feature in holo-HypCD has already been described previously (Soboh et al. 2012). This might be due to a second chromophore in addition to the [4Fe-4S] cluster which is only present in holo-HypCD_{strep}, that is the Fe(CN)₂(CO) moiety. Recently, the UV-Vis spectroscopic signature for the NiFe(CN)₂(CO) moiety has been detected for the first time in an isolated large subunit (Caserta et al. 2020). It showed an absorbance maximum in the region between 360 – 400 nm, which supports the assignment of the absorbance feature between 350 – 400 nm in holo-HypCD_{strep} to the Fe(CN)₂(CO) moiety.

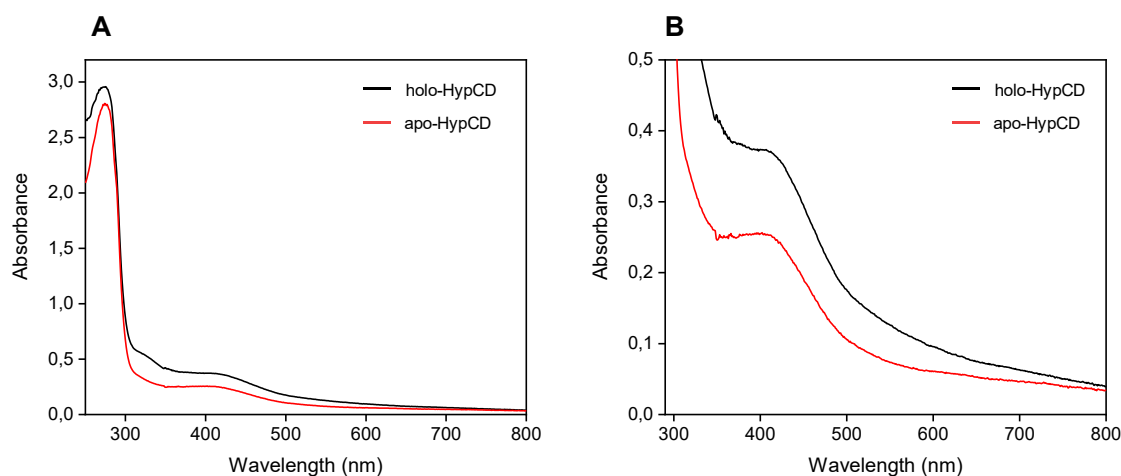


Figure 17. UV-Vis spectra of holo- and apo-HypCD_{strep}. 40 μ M each of apo- (red line) and holo-HypCD_{strep} (black line) purified via affinity chromatography recorded in 100 mM Tris-HCl, pH 8 at 4 °C, 100 mM NaCl. B shows an enlargement of the spectra shown in A in the region between 290 and 800 nm.

Metal determination via ICP-OES. To investigate whether apo-HypCD_{strep} contains the precursor Fe and to check if the [4Fe-4S] cluster is fully assembled, the Fe content of purified HypCD_{strep} was determined by ICP-OES (**Table 10**). The expected amount of Fe per protein is five, corresponding to four Fe of the [4Fe-4S] cluster in HypD and one Fe, which in case of

Results

holo-HypCD_{strep} stems from the Fe(CN)₂(CO) moiety. In an IR spectroscopic control experiment, we showed that HypC alone does not carry the Fe(CN)₂(CO) cofactor (**Figure 18 D**). In case of apo-HypCD_{strep} one would also expect five Fe, but the precursor Fe should lack the CN⁻ and CO ligands. Samples purified via affinity chromatography contained only substoichiometric amounts of Fe. Since the Strep-tag is fused to HypC, purified protein after affinity chromatography contained an excess of dimeric HypC. To obtain a pure preparation with an apparent 1:1 stoichiometry of HypC and HypD, an additional purification step via size-exclusion chromatography was added. The chromatograms of the size-exclusion chromatography runs of apo-HypCD_{strep} and holo-HypCD_{strep} are shown in **Figure 18 A** and **B**. Elution of the protein was monitored at 280 and additionally at 420 nm, at which the [4Fe-4S] cluster of HypD absorbs. The peak assignment is based on the comparison to a calibration curve (**Figure 18 C**). The chromatogram of holo-HypCD_{strep} showed an additional peak around 12.4 ml which presumably corresponded to a dimer of the HypCDE complex. Dimerization of the HypCDE complex has also been observed in the crystal structure of the HypCDE complex from *T. kodakarensis* (Watanabe et al. 2012a). By collecting only the fractions containing pure HypCD_{strep}, the Fe content was increased to (6.64 ± 0.09) Fe/protein for holo-HypCD_{strep} and (5.37 ± 0.06) Fe/protein for apo-HypCD_{strep}. Similar values have been previously reported for holo-HypCD (Soboh et al. 2012). Strikingly, apo-HypCD_{strep} contains one Fe less compared to holo-HypCD_{strep} purified in the same way. This indicates, that apo-HypCD_{strep} carries the [4Fe-4S] cluster while lacking the precursor Fe.

Results

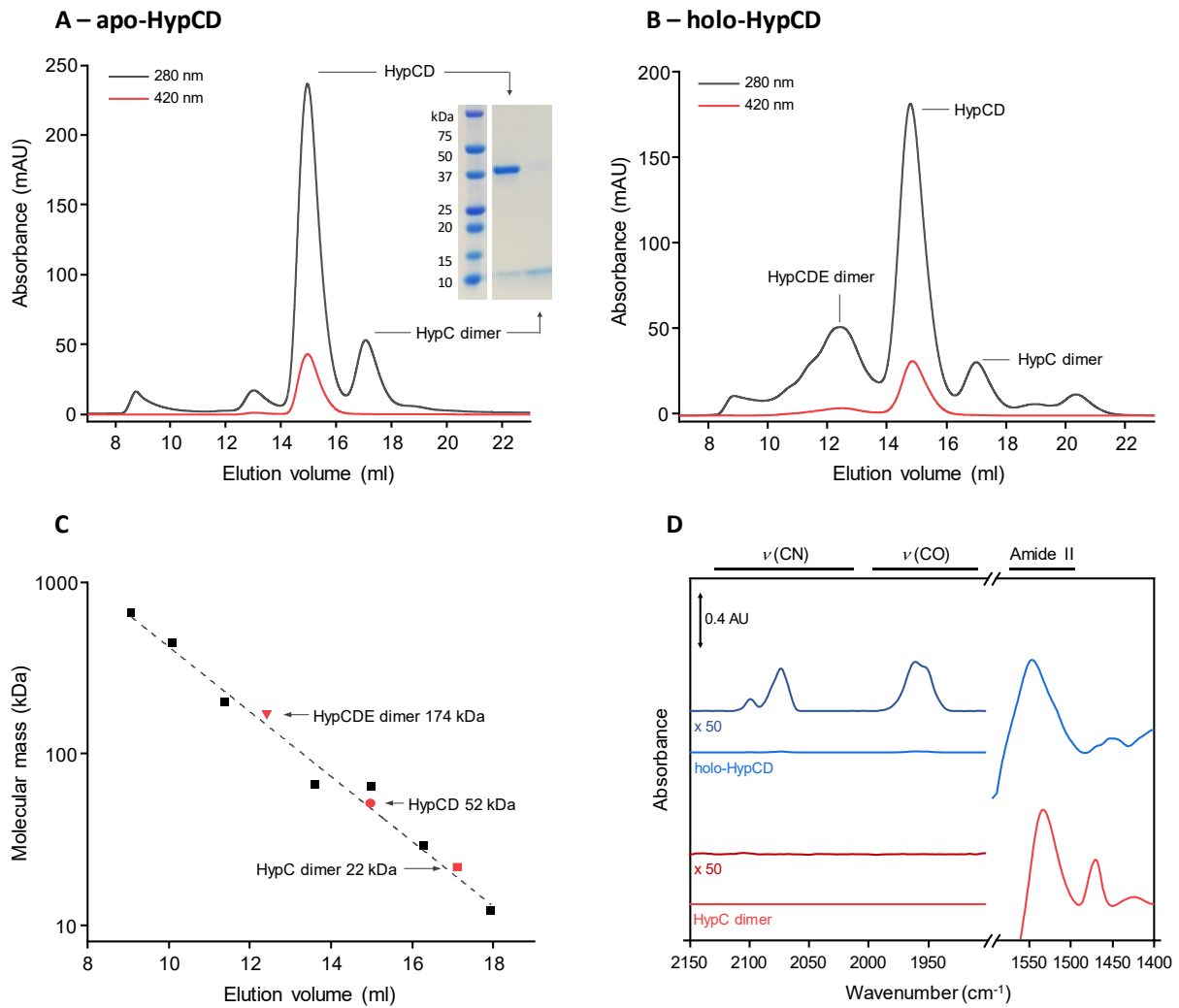


Figure 18. Size-exclusion chromatography of apo-HypCD_{strep}. Size-exclusion chromatography was performed in 100 mM Tris-HCl, pH 8 at 4 °C, 100 mM NaCl. Elution of the protein was monitored at 280 nm (grey) and 420 nm (red). (A) Chromatogram of 2.4 mg apo-HypCD_{strep}. Samples corresponding to HypCD and dimeric HypC were separated on a 12.5 % SDS gel and subsequently stained with Coomassie brilliant blue. The left lane contains a protein standard with the corresponding molecular masses indicated on the left-hand side. Lanes containing HypCD and HypC dimer are indicated with arrows. (B) Chromatogram of 2.0 mg holo-HypCD_{strep}. (C) Calibration curve of seven standard proteins with molecular masses between 12 – 670 kDa. Samples are plotted with the expected sizes of HypCDE dimer (▼ 174 kDa), HypCD (● 52 kDa), and HypC dimer (■ 22 kDa) against the corresponding elution volume. (D) IR spectra of dimeric HypC collected after Size-exclusion (blue) compared to holo-HypCD_{strep} purified via affinity chromatography (red). Spectra are normalized to the protein concentration (see amide II region). The CN/CO region of both spectra is additionally 50-times magnified (dark blue and dark red traces).

Results

Table 10. Metal determination via ICP-OES of apo- and holo-HypCD_{strep}. Samples were either purified only via affinity chromatography (AC) or additionally by size-exclusion chromatography (AC/SEC). The metal content is given in Fe/protein. The metal content of one biological replicate each was measured in triplicates.

Sample	AC	AC/SEC
apo-HypCD _{strep}	2.77 ± 0.03	5.37 ± 0.06
holo-HypCD _{strep}	3.72 ± 0.01	6.64 ± 0.09

Resonance Raman (RR) spectroscopy. To gain further information about the metal cofactors in HypCD, holo- and apo-HypCD_{strep} were analyzed by resonance Raman (RR) spectroscopy. RR spectroscopy detects metal-ligand vibrations, such as Fe-CN, Fe-CO and Fe-S, Fe-N or Fe-O modes, thus providing information on structural and redox properties of metal cofactors. Previous measurements conducted on different [NiFe]-hydrogenases have shown that signals in the range of 400 – 600 cm⁻¹ of the RR spectrum reflect Fe-CN/CO modes, while signals below 400 nm⁻¹ correspond to Fe-S modes. Excitation with different wavelengths enables signal enhancement of various cofactors. Excitation with 458 nm results in an enhancement of FeS cluster signals, whereas Fe-CO/CN signals are best observed at 514 nm (Siebert et al. 2013; Horch et al. 2014; Horch et al. 2015a).

Samples of holo- and apo-HypCD_{strep} were measured with an excitation wavelength of 458 nm (**Figure 19**), at which signals of Fe-S stretching modes are enhanced. The spectra were normalized to the protein concentration. Holo-HypCD_{strep} was measured in the as-isolated, oxidized state and after reduction with a 10-fold molar excess of NaDT to reduce the [4Fe-4S] cluster. In the reduced state, the [4Fe-4S] cluster would be Raman-silent, which was supposed to enable a better detection of features derived from the redox-inactive Fe(CN)₂(CO) moiety (see **Figure 16**). Apo-HypCD_{strep} was measured in the as-isolated state. No signals corresponding to Fe-CN or Fe-CO modes were observed in any of the spectra. However, the spectrum of as-isolated, aerobically oxidized holo-HypCD_{strep} exhibited intense signals in the Fe-S region at 253, 285, 337, 363 and 403 cm⁻¹. These stretching modes, and especially the frequency of the most intense band at 337 cm⁻¹, are characteristic for [4Fe-4S] clusters (Todorovic and Teixeira 2018). The spectrum of reduced holo-HypCD_{strep} still exhibited the same Fe-S bands but with reduced intensity, indicating that the [4Fe-4S] cluster was not completely reduced. It has been described earlier, that HypD can only be partially reduced with NaDT ($E^{\circ'} = -660$ mV) although the redox potential of the [4Fe-4S] cluster was determined to be $E^{\circ'} = -260$ mV (Adamson et al. 2017a; Roseboom et al. 2005). Nevertheless, these results support the assignment of the observed Fe-S bands as [4Fe-4S] cluster signals. This

Results

assumption can be further validated by comparison with apo-HypCD_{strep}, which lacks the Fe(CN)₂(CO) moiety and exhibits the same bands in the Fe-S region.

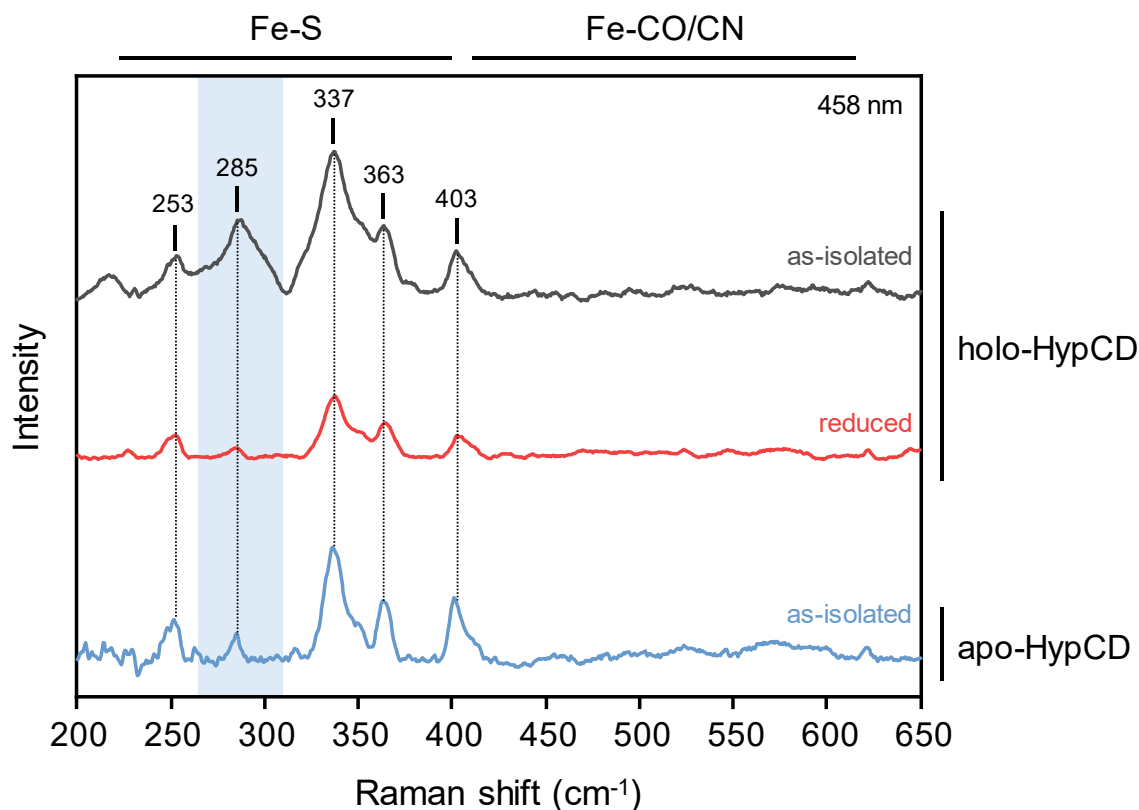


Figure 19. Resonance Raman spectra of holo- and apo-HypCD. Holo-HypCD was recorded in the as-isolated, oxidized state (grey spectrum) and in the reduced state (red spectrum) Apo-HypCD was recorded in the as-isolated state (blue spectrum). All spectra were recorded with 458 nm excitation. The spectra were normalized with respect to the phenylalanine band at 1003 cm⁻¹.

Interestingly, all of the bands in the NaDT-treated sample decreased in the same ratio, except for one broad band at 285 cm⁻¹ of which the intensity decreased disproportionate (**Figure 19**, blue area). Possibly, this band at 285 cm⁻¹ represents more than one Fe-S mode originating from the [4Fe-4S] cluster. It may contain a second species derived from another metal cofactor, whose signals disappeared completely upon reduction. Not only the [4Fe-4S] cluster, but also the cysteine-coordinated Fe(CN)₂(CO) moiety would cause Fe-S signals in this region of the RR spectrum. However, as shown by IR analysis (see above), the Fe(CN)₂(CO) moiety cannot be reduced with NaDT, so Fe-S signals corresponding to the cysteine-coordinated Fe(CN)₂(CO) moiety would not disappear upon reduction. It is possible, that parts of the holo-HypCD_{strep} preparation contain HypCD carrying the precursor Fe without CN⁻ and CO ligands. Signals derived from the Fe-S stretching mode of the cysteine-bound precursor Fe might contribute to the wide signal at 285 cm⁻¹. A precursor Fe in the Fe(III) state would be reduced

with NaDT, resulting in signal loss as observed for rubredoxins (Fe4S). In rubredoxins, which are RR active in the Fe(III) state and RR inactive in the Fe(II) state, however, the Fe is coordinated by four cysteine residues (Todorovic and Teixeira 2018). Since the two conserved cysteine residues of HypC and HypD would yield a twofold coordination of the precursor Fe, additional ligands might be temporarily involved. Based on the crystal structures and computational models, two conserved histidine residues are in close proximity to the Fe(CN)₂(CO) moiety and could be involved in Fe binding (Watanabe et al. 2012a; Albareda et al. 2013). Fe-N(His) stretching vibrations are observed in the same region of the RR spectrum as Fe-S stretching vibrations. In RR spectra of Rieske proteins, which carry a [2Fe-2S] cluster coordinated by two Cys and two His residues, the Fe-N(His) stretching modes appear around 270 cm⁻¹ and disappear upon reduction (Todorovic and Teixeira 2018; Kuila et al. 1992). Hence, the broad signal at 285 cm⁻¹ could be caused partially by Fe-N(His) stretching modes overlapping with a Fe-S stretching mode from the 4Fe4S cluster.

To verify these assumptions, additional experiments are required, such as analysis of Fe-reconstituted apo-HypCD, which would carry exclusively the precursor Fe devoid of any CO/CN⁻ ligands. In Rieske proteins, the Fe-N(His) stretching mode is pH-sensitive depending on the imidazole protonation state (Todorovic and Teixeira 2018; Kuila et al. 1992). RR spectra taken at different pH could help to identify possible Fe-N(His) stretching vibrations in HypCD.

3.2.2. ATPase activity of HypCD

Recently, the HypCD complex has been shown to have an ATPase activity, whose function is so far unknown (Nutschan et al. 2019). To gain more information, we tested therefore the ATPase activities of purified apo- and holo-HypCD_{strep} cultivated and purified under different conditions (**Figure 20**).

For the detection of the ATPase activity, a reporter system comprising pyruvate kinase (PK) and lactate dehydrogenase (LDH) was used. In the presence of phosphoenolpyruvate (PEP), PK converts ADP produced by HypCD into ATP and pyruvate. In the second LDH-catalyzed reaction pyruvate is converted to lactate with the concomitant oxidation of NADH to NAD⁺. Changes in the NADH content in the assay can easily be monitored spectrophotometrically at 340 nm.

Results

Production of HypCD_{strep} under anaerobic conditions and its subsequent purification in the absence of DTT resulted in an ATPase activity comparable to the activity of HypCD_{strep} purified from aerobically grown cells, indicating that the cultivation conditions have no effect on the ATPase activity. HypCD_{strep} from anaerobically grown cells, purified in the presence of 0.1 mM DTT, however, revealed the highest activity. Thus, purification under reducing conditions seems to result into highest ATPase activity. Notably, there was no significant difference in ATPase activity between apo- and holo-HypCD_{strep} preparations. Hence, the ATPase activity of HypCD seems to be independent of the presence or absence of the Fe(CN)₂(CO) moiety.

Surprisingly, even the highest ATPase activity determined with the PK-LDH system was approximately 100-times lower than that previously reported, which was about 1 U/mg (Nutschan et al. 2019). In the study of Nutschan et al., however, the HypCD complex was purified under anaerobic conditions and in the presence of NaDT and the activity was determined in an HPLC-based assay under different conditions.

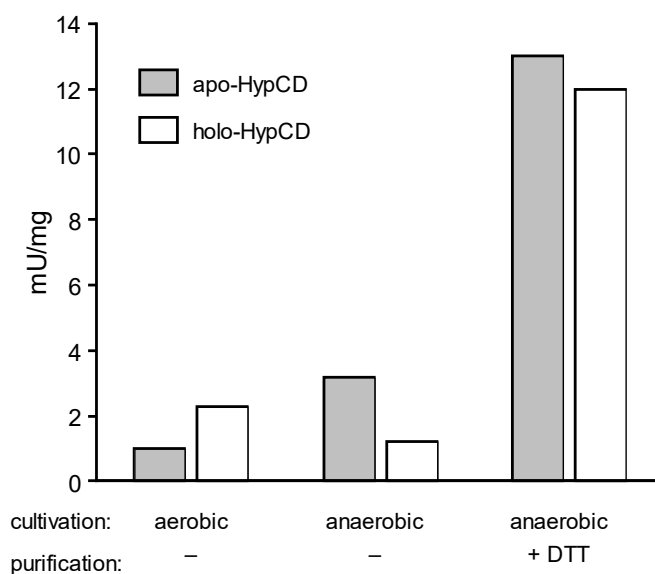


Figure 20. ATPase activity of different HypCD_{strep} preparations. ATPase activity of HypCD_{strep} cultivated under aerobic or anaerobic conditions and prepared in the absence or presence of 0.1 mM DTT as indicated below the columns. Apo-HypCD_{strep} is colored in grey, holo-HypCD_{strep} is colored in white.

3.2.3. Chemical maturation of HypCD

3.2.3.1. Reconstitution of apo-HypCD with Fe

Since apo-HypCD_{strep} seems to lack the precursor Fe, we aimed to reconstitute it with Fe. The reconstitution reaction with apo-HypCD_{strep} was performed under anaerobic, reducing conditions in the presence of DTT and Fe(SO₄)₂(NH₄)₂ as described in materials and methods (see chapter 2.31). After the reconstitution reaction, the excess of Fe was removed by size-exclusion chromatography. Finally, the Fe content of reconstituted apo-HypCD_{strep} (apoHypCD_{strep}(Fe)) was determined by ICP-OES. As additional control, holo-HypCD_{strep} was treated in the same way and the Fe content was also determined. The Fe content of both reconstituted samples in comparison to non-reconstituted apo- and holo-HypCD is listed in **Table 11**. The Fe content of non-reconstituted and reconstituted holo-HypCD_{strep} remained the same, whereas the reconstituted apo-HypCD_{strep}(Fe) contains one Fe per protein more than non-reconstituted apo-HypCD_{strep} indicating, that the reconstitution was successful.

Table 11. Metal determination via ICP-OES of Fe-reconstituted (Fe) apo- and holo-HypCD_{strep}.

	apoHypCD _{strep}	apoHypCD _{strep} (Fe)	holo-HypCD _{strep}	holo-HypCD _{strep} (Fe)
Fe/protein	5.37 ± 0.06	6.39 ± 0.06	6.64 ± 0.09	6.53 ± 0.08

3.2.3.2. Treatment of apo-HypCD(Fe) with KCN and CO gas

After successful reconstitution of apo-HypCD_{strep} with Fe, we aimed to develop an *in vitro* assembly system to reconstitute the entire Fe(CN)₂(CO) moiety. In this chemical assembly assay, apo-HypCD_{strep}(Fe) served as the basis, which was incubated with KCN and CO gas as possible sources for the CN⁻ and CO ligands. Ligand attachment was monitored by IR spectroscopy.

First, we tested the attachment of CO to Fe-reconstituted apo-HypCD_{strep}. Therefore, a highly concentrated sample (~ 0.8 mM) of apo-HypCD_{strep}(Fe) was reduced with a 10-fold molar excess of NaDT under anoxic conditions inside an anaerobic workstation. The sample was sealed with a gas-tight rubber septum and removed from the anaerobic workstation where it was purged for 30 min with CO gas before it was 1:2 diluted with CO-saturated buffer. Under constant CO gas flow, the sample was loaded into the IR cell. The corresponding IR spectrum

Results

showed no CO stretching vibrations (**Figure 21**), indicating that CO did not bind to the precursor Fe.

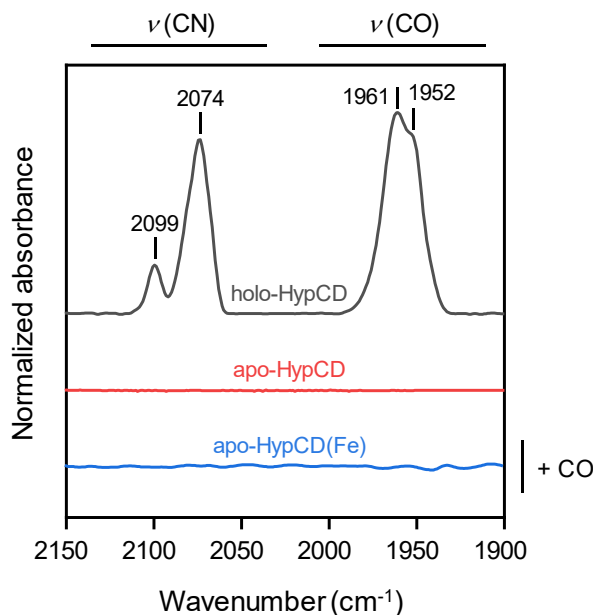


Figure 21. Treatment of apo-HypCD(Fe) with CO gas. Apo-HypCD_{strep}(Fe) was incubated with a 10-fold molar excess of NaDT and subsequently purged with CO gas and diluted with CO saturated buffer. IR absorbance spectra are shown in the following colors: as-isolated holo-HypCD_{strep} (grey), as-isolated apo-HypCD_{strep} (red), apo-HypCD(Fe) treated with CO (blue).

Next, Fe-reconstituted apo-HypCD_{strep} was incubated with KCN under anoxic, reducing conditions and analyzed by IR spectroscopy (**Figure 22**, **Table 12**). The IR spectrum of KCN-treated apo-HypCD_{strep}(Fe) exhibited five signals in the CN region at 2040, 2080, 2093, 2114 and 2124 cm⁻¹. The signals at 2080 and 2093 cm⁻¹ correspond to aqueous CN⁻ and HCN, respectively (Ciaccafava et al. 2016). The assignment of the signal to 2093 cm⁻¹ as dissolved HCN was verified by IR analysis of the reconstitution buffer containing KCN (**Figure 22 A**, purple trace). Control experiments using KCN-treated apo-HypCD and BSA were performed in order to assign the remaining bands at 2040, 2114 and 2124 cm⁻¹. The signal at 2124 cm⁻¹ was also observed in the spectra of non-reconstituted apo-HypCD_{strep} and BSA and, hence, does not represent an Fe-bound CN species. It probably represents CN bound to a cysteine residue since HypCD and BSA both possess several solvent-exposed cysteine residues. The broad signal at 2039/40 cm⁻¹, however, was HypCD-specific and appeared only in the spectra of KCN-treated Fe-reconstituted and non-reconstituted apo-HypCD. The second derivative spectrum of KCN-treated apo-HypCD(Fe) revealed that this band was composed of two overlapping bands at 2038 and 2044 cm⁻¹ (**Figure 22 B**). Based on the comparison to the

Results

second derivative spectrum of $[\text{Fe(II)(CN)}_6]^{4-}$ which exhibits one sharp band at 2037 cm^{-1} (**Figure 22 B**), signals in this region might be assigned to Fe(II)-bound CN stretching vibrations. Since the 2040 cm^{-1} band was also present in non-reconstituted apo-HypCD it probably derived from interaction of CN with the [4Fe-4S] cluster. However, CN binding to the precursor Fe would possibly result in a similar stretching frequency and therefore could not be distinguished from Fe(II)-CN species derived from the [4Fe-4S] cluster. It must be noted, that the band intensities of the Fe-reconstituted and non-reconstituted apo-HypCD in **Figure 22 A** cannot be compared since Fe-reconstituted apo-HypCD was additionally purified by size-exclusion chromatography resulting in a higher Fe per protein content, whereas non-reconstituted apo-HypCD was only purified by affinity chromatography. Finally, the weak signal at 2114 cm^{-1} observed in the spectrum of KCN-treated apo-HypCD_{strep}(Fe) might correspond to CN bound to an Fe(III) species as it is almost at the same positions as the CN stretching of $[\text{Fe(III)(CN)}_6]^{3-}$ (**Figure 22 B**).

To remove nonspecifically protein-bound CN and the excess of free CN, KCN-treated apo-HypCD and apo-HypCD(Fe) were buffer exchanged using a desalting column. The eluted samples were again concentrated and subjected to IR analysis. To be able to compare the intensities of the CN bands, both samples were also purified by size-exclusion chromatography. As observed before (Ciaccafava et al. 2016), the signals at 2080 and 2124 cm^{-1} corresponding to aqueous CN^- and protein-bound CN, respectively, vanished after buffer exchange (**Figure 22 C**). The band at 2093 cm^{-1} corresponding to HCN significantly decreased. Surprisingly, also the band at $2039/40\text{ cm}^{-1}$ corresponding to an Fe(II)-bound CN species decreased drastically and the band position shifted by a few wavenumber indicating that the main Fe(II)-bound CN species contributing to the $2039/40\text{ cm}^{-1}$ band is not tightly bound to the protein. Possibly, this species is $[\text{Fe(II)(CN)}_6]^{4-}$ complex which was formed in a reaction with free Fe released from the [4Fe-4S] cluster upon incubation with KCN. The degradation of FeS clusters and the release of free Fe upon KCN treatment followed by the formation of $[\text{Fe(II)(CN)}_6]^{4-}$ has also been observed for HydSL [NiFe]-hydrogenase from *Thiocapsa roseopersicina* (Zorin et al. 2017).

Results

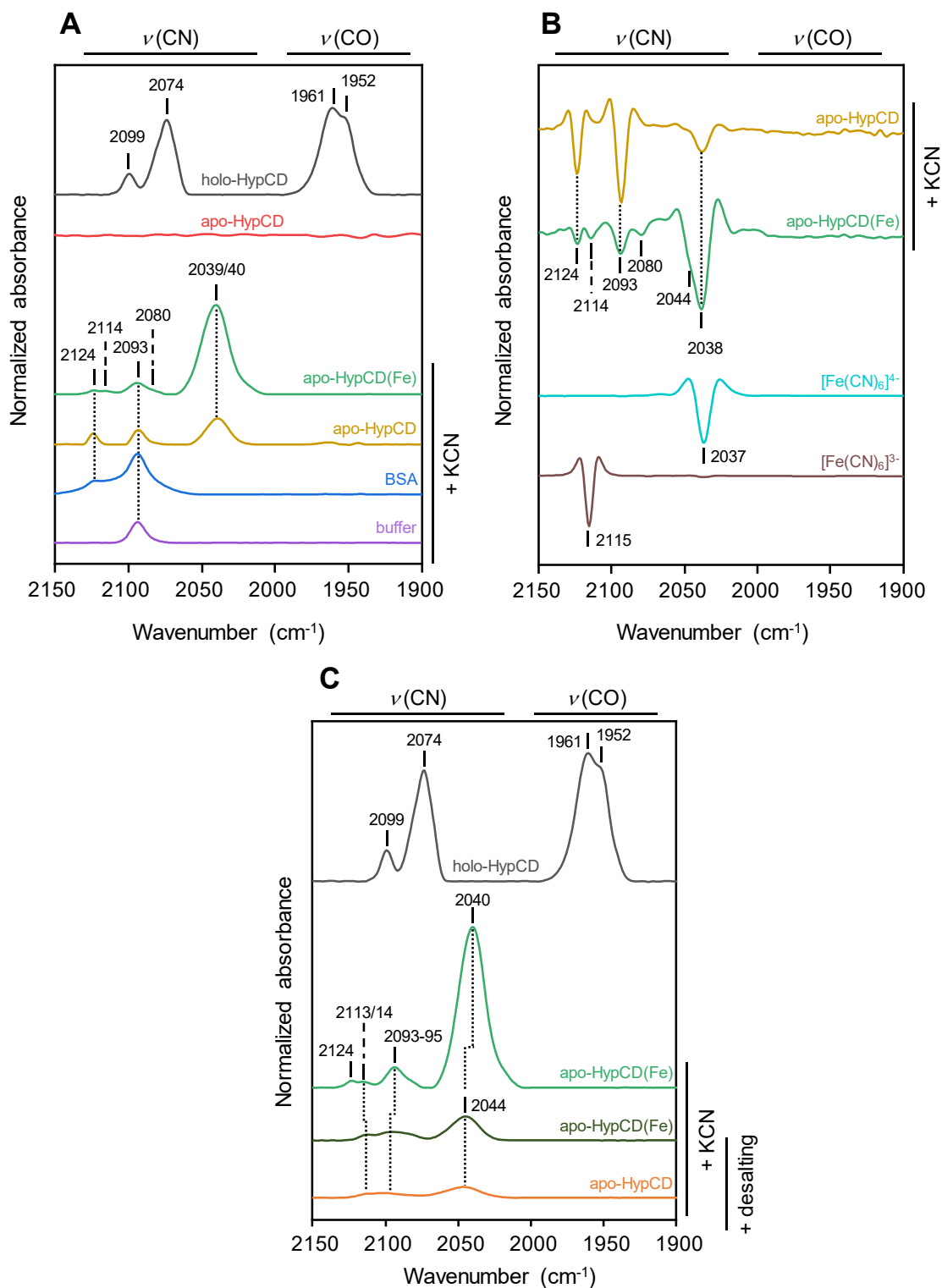


Figure 22. Treatment of apo-HypCD(Fe) with KCN. (A) IR absorbance spectra are shown in the following colors: as-isolated holo-HypCD_{strep} (grey), as-isolated apo-HypCD_{strep} (red), the following samples were treated with 5 – 10 fold excess of KCN: apo-HypCD_{strep}(Fe) (green), apo-HypCD_{strep} (yellow), BSA (blue), and buffer 100 mM Tris pH 8.0 at 4 °C, 100 mM NaCl (purple); (B) second derivative spectra are color-coded as follows: KCN-treated apo-HypCD_{strep}(Fe) (green), KCN-treated apo-HypCD_{strep} (yellow), $[\text{Fe}(\text{CN})_6]^{4-}$ (cyan) and $[\text{Fe}(\text{CN})_6]^{3-}$ (brown); (C) absorbance spectra normalized to the protein concentration of as-isolated holo-HypCD (grey), KCN-treated apo-HypCD(Fe) (green), KCN-treated samples after buffer exchange via desalting column: apo-HypCD(Fe) (dark green), apo-HypCD (orange).

Results

The remaining bands at 2045/2046 cm^{-1} and 2113 cm^{-1} presumably represent CN binding to a protein-bound Fe, possibly the precursor Fe. If this is the case, the peak integral of these bands and therefore the amount of protein-bound Fe-CN species should be higher in Fe-reconstituted apo-HypCD compared to non-reconstituted apo-HypCD. Indeed, the peak integral of non-reconstituted apo-HypCD was about 57 % compared to that of reconstituted apo-HypCD. Non-reconstituted apo-HypCD might also be partially equipped with the precursor Fe which can bind CN explaining the Fe-CN species produced in KCN-treated apo-HypCD. These results indicate that Fe-reconstituted apo-HypCD, and in a lower amount also non-reconstituted apo-HypCD, carries the precursor Fe for the assembly of the $\text{Fe}(\text{CN})_2(\text{CO})$ moiety and that it can be chemically reconstituted with CN^- ligands. However, the comparison of the CN band intensities in KCN-treated apo-HyoCD(Fe) and holo-HypCD showed that the *in vitro* CN attachment was rather inefficient. Based on the high amount of $[\text{Fe}(\text{II})(\text{CN})_6]^{4-}$ that was removed after buffer exchange, a significant portion of the [4Fe-4S] cluster seems to be damaged, which might hinder CN attachment to the precursor Fe. Further optimization of the assay, such as an optimized KCN concentration to avoid excessive damage of the [4Fe-4S] cluster, are necessary.

The next step in the complete assembly of the $\text{Fe}(\text{CN})_2(\text{CO})$ cofactor would be the addition of CO gas to apo-HyoCD(Fe) equipped with CN^- ligands.

Table 12. CN stretching frequencies of KCN-treated HypCD and controls. Samples were treated with KCN and either immediately analyzed by IR (+KCN) or after an additional buffer exchange step using a desalting column (+KCN + desalting). Stretching frequencies are given in cm^{-1} .

Treatment	Sample	CN^-	HCN	Protein-bound CN	Fe(II)-CN	Fe(III)-CN
	$[\text{Fe}(\text{CN})_6]^{4-}$				2037	
	$[\text{Fe}(\text{CN})_6]^{3-}$					2115
	buffer		2093			
+ KCN	BSA		2093	2124		
	apo-HypCD(Fe)	2080	2093	2124	2040	2114
	apo-HypCD		2093	2124	2039	
+ KCN	apo-HypCD(Fe)		2095		2045	2113
+ desalting	apo-HypCD		2095		2046	2113

3.2.3.3. Reconstitution of apo-HypCD with a chemical mimic of the Fe(CN)₂(CO) complex

To investigate whether apo-HypCD accepts a chemical mimic of the Fe(CN)₂(CO) complex, it was reconstituted with the synthetic (PPh₄)[Fe(CO)₂(CN)₂(μ-pdt)K] complex (Li et al. 2005). The complex was synthesized by Siad Wolff, a member of the group of Christian Limberg at HU Berlin. For the reconstitution, apo-HypCD_{strep} was first reduced with NaDT followed by incubation with the synthetic Fe complex. To remove unbound Fe complex, the reconstitution mix was loaded on a Sephadex™ desalting column (see Materials and Methods chapter 2.30). Finally, the eluted HypCD protein was concentrated and subjected to IR spectroscopy. All steps were performed under anoxic conditions. The IR spectrum of the free complex showed two CN stretching vibrations at 2104 and 2083 cm⁻¹, and two CO stretching vibrations at 2034 and 1984 cm⁻¹ (**Figure 23**). The IR spectrum of apo-HypCD_{strep} reconstituted with the Fe complex (HypCD_{strep}(mimic)) exhibited a completely different spectrum with just three bands similar to the spectrum of holo-HypCD. Two broad bands at 2098 and 2073 cm⁻¹ represent CN stretching vibrations, and were shifted by just one wavenumber compared to the corresponding bands in the spectrum of holo-HypCD_{strep}. There was only one broad band in the CO region at 1973 cm⁻¹, whereas holo-HypCD_{strep} showed two CO bands at 1961 and 1952 cm⁻¹ (**Figure 23**). Minor differences in the band positions might be explained by slightly different conformations of the Fe(CN)₂(CO) moiety in HypCD_{strep}(mimic) compared to holo-HypCD_{strep}. Such differences have also been observed for synthetically reconstituted HydF maturase, which delivers the [2Fe] sub-cluster to the apo-form of [FeFe]-hydrogenase (Berggren et al. 2013). Thus, these results indicate that the synthetic Fe complex was successfully integrated into apo-HypCD_{strep}. This conclusion was supported by an enhanced stability of the HypCD-bound Fe-complex compared to the free complex. The IR spectrum of HypCD_{strep}(mimic) remained unchanged after freezing and thawing and after exposure to O₂, whereas the free complex is very unstable and immediately damaged upon O₂ exposure. Comparison of the CN and CO peak integrals of spectra normalized to the protein concentration indicates a cofactor loading of HypCD_{strep}(mimic) of about 65 % compared to native holo-HypCD_{strep}. One possible explanation for only sub-stoichiometric cofactor loading would be that, apo-HypCD is not completely free of the precursor Fe and thus cannot be fully reconstituted with the synthetic Fe complex.

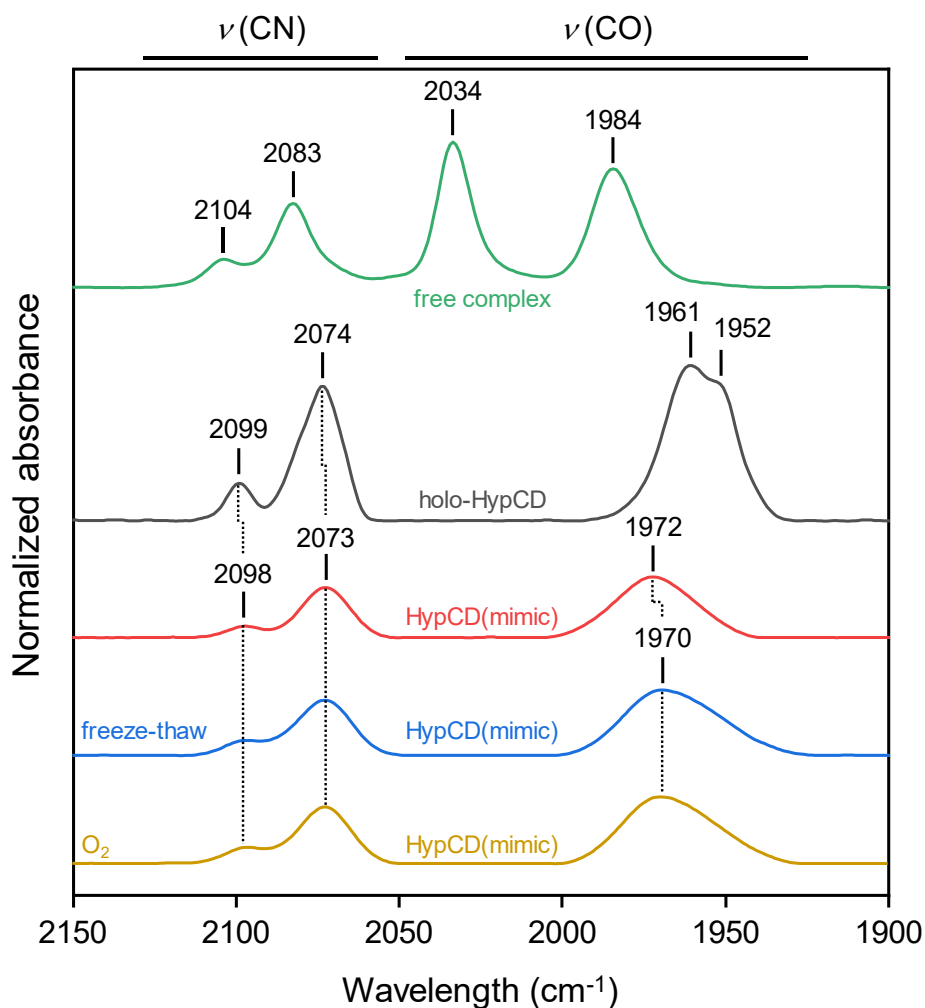


Figure 23. Reconstitution of apo-HypCD_{strep} with a synthetic Fe(CN)₂(CO) moiety mimic. IR spectra of the free complex (green), holo-HypCD_{strep} (grey), HypCD_{strep}(mimic) directly after reconstitution (red), HypCD_{strep}(mimic) after freezing and thawing (blue) and HypCD_{strep}(mimic) after O₂ exposure (yellow). Spectra (except for the free complex) are normalized to the protein concentration.

3.2.4. Enzymatic *in vitro* assembly of the Fe(CN)₂(CO) moiety

An alternative to the chemical maturation of the Fe(CN)₂(CO) moiety is an enzymatic *in vitro* assembly assay using purified HypE, HypF and HypX for the synthesis of the CN⁻ and CO ligands and their transfer to Fe-reconstituted apo-HypCD_{strep}. An advantage of the enzymatic assembly assay might be a higher specificity and efficiency of the enzyme-catalyzed ligand synthesis and attachment compared to the chemical assembly assay.

3.2.4.1. Purification of functional active HypE and HypF

To enable isolation of HypCD_{strep} from an assembly mix containing HypEF and HypX, different affinity tags were used for their purification. While the purification and an activity assay for *R. eutropha* MBP-HypX are described in chapter 3.3.2, purification protocols and activity assays for HypE and HypF first had to be established in our group. Therefore, a hexahistidine tag was fused N-terminally to both HypE and HypF of *E. coli* and the fusion proteins were purified via Ni-NTA affinity chromatography (**Figure 24**). The purification protocols were based on previous published protocols (Blokesch et al. 2004c) and modified as described in Materials and Methods, chapter 2.14.4.

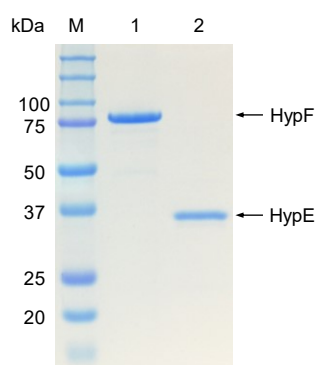


Figure 24. SDS-PAGE gel of HypF and HypE. Purified HypF and HypE were separated on a 12.5 % SDS gel and stained with Coomassie brilliant blue. Lane 1 contains 2 µg HypF with a theoretical molecular mass of 82 kDa, lane 2 contains 2 µg HypE with a theoretical molecular mass of 35 kDa, lane M contains a protein standard. The corresponding molecular masses are indicated.

To probe the functionality of purified HypF and HypE, an activity assay was developed probing the ATP-dependent dehydratase reaction of HypE in a coupled assay with HypF. The PK-LDH couple was used as reporter system (**Figure 25**), and the oxidation of NADH to NAD⁺ was followed at 340 nm.

Results

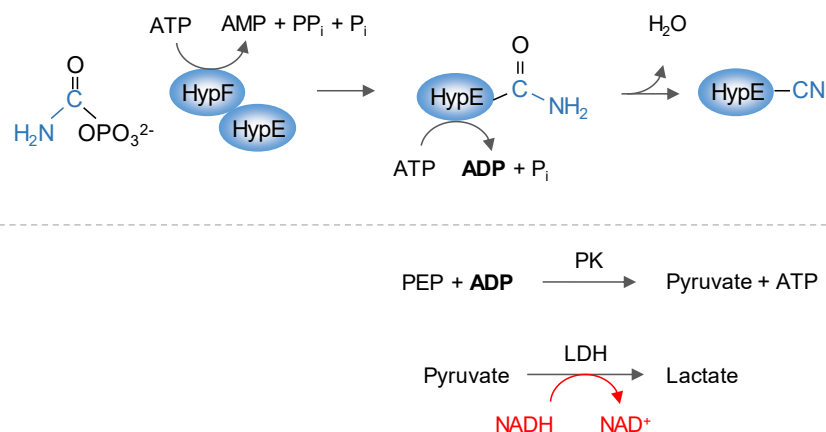


Figure 25. Coupled assay of HypF and HypE to test the ATP-dependent dehydration reaction of HypE. Pyruvate kinase (PK) and lactate dehydrogenase (LDH) are used as reporter system. PK uses ADP produced by HypE and phosphoenolpyruvate (PEP) as substrates to form pyruvate and ATP. LDH uses pyruvate and NADH to produce lactate and NAD⁺.

First, the HypE-dependent ATPase activity without HypF was measured (**Figure 26, Table 13**). It has been shown earlier, that HypE alone hydrolyses ATP to ADP and P_i without any other substrate with a rate of $(0.10 \pm 0.01) \text{ min}^{-1}$ (Blokesch et al. 2004c). The ATPase activity of HypE measured with the PK-LDH assay revealed a rate of 1.09 min^{-1} , which is approximately ten times higher than the one previously reported. This discrepancy might be explained by different experimental set ups and conditions. As described earlier, HypE activity was independent of the presence of carbamoyl phosphate, which is the substrate of HypF (Blokesch 2004a). As the dehydration of thiocarbamate to thiocyanate is ATP-dependent (Reissmann et al. 2003), we expected that the ATPase activity would strictly depend on the presence of the protein-bound thiocarbamate modification as the substrate. If all as-purified HypE molecules carry the thiocarbamate modification, the reaction should stop just after one turnover. This was not the case; in fact, the reaction was continuing in the same rate over many turnovers. Thus, the ATPase activity of HypE does not rely on the presence of the thiocarbamate modification. The reason for this unspecific ATPase activity remains elusive.

Results

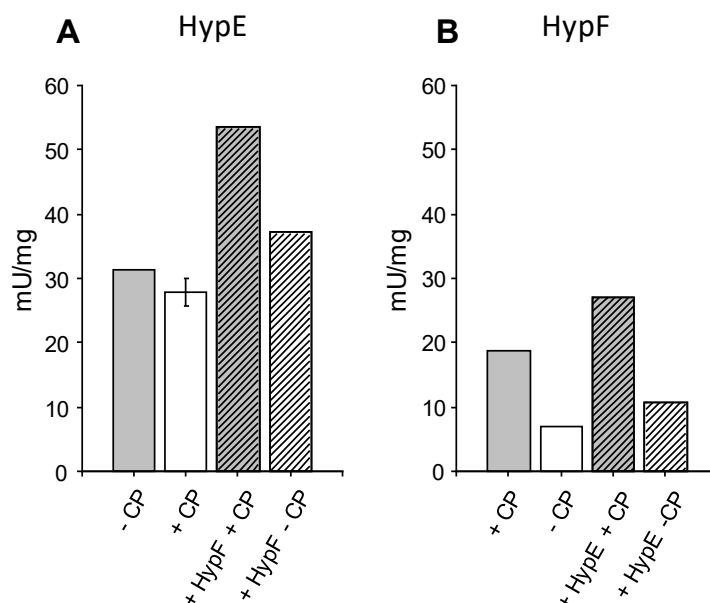


Figure 26. ATPase activity of HypE and HypF measured with the PK-LDH assay. Activities of HypE and HypF alone were tested with carbamoyl phosphate (+ CP) or without carbamoyl phosphate (– CP) in the assay. Activities in coupled assays with HypE and HypF were determined as described in the text. Columns on the left-hand side represent HypE activities indicated below. Columns on the right-hand side correspond to HypF activities as indicated below.

Next, HypF activity alone was tested with the PK-LDH assay. Even though HypF also catalyzes an ATP-dependent reaction, no activity should be detected with the PK-LDH system, since it is reported that HypF does not produce ADP, but cleaves ATP into AMP and PP_i (Reissmann et al. 2003; Paschos et al. 2002b). Surprisingly, purified HypF alone revealed an ATPase activity with a rate of 1.54 min⁻¹ in the presence of its substrate carbamoyl phosphate. Even without carbamoyl phosphate a residual ATPase activity of about 40 % was measured (Table 13, Figure 26).

Hints for the HypF-catalyzed hydrolysis of ATP to ADP have already been obtained from crystal structures of truncated *E. coli* HypF and full-length *Caldanaerobacter subterraneus* HypF. Crystals soaked with an ATP derivative revealed ADP binding in one of the two nucleotide binding sites of HypF (Petkun et al. 2011; Shomura and Higuchi 2012). Moreover, traces of ADP have also been observed by thin layer chromatography after the reaction of HypF with labeled α-³²P-ATP and carbamoyl phosphate (Paschos 2002a). However, compared to the HypF-dependent ATP to AMP hydrolysis which was determined with a rate of 90 min⁻¹ (Paschos 2002a) the ATP to ADP hydrolysis was approximately 60-fold lower (1.54 min⁻¹)

Results

and seems to be a side reaction as it is also detectable without the substrate carbamoyl phosphate.

Table 13. ATPase activities of HypE and HypF measured with the PK-LDH assay. Activities of HypE and HypF alone were tested with carbamoyl phosphate (+ CP) or without carbamoyl phosphate (– CP) in the assay. Activities in coupled assays with HypE and HypF were estimated as described in the text. Relative HypE activities were calculated in relation to the HypE activity without carbamoyl phosphate. Relative HypF activities were calculated in relation to the HypF activity with carbamoyl phosphate.

		Relative activity	Specific activity (mU/mg)	k_{cat} (min ⁻¹)
HypE	– CP	1.0	31.3	1.09
	+ CP	0.9	27.8	0.97
	+ HypF	1.7	53.6	1.88
	+ HypF – CP	1.2	37.2	1.30
HypF	+ CP	1.0	18.0	1.54
	– CP	0.4	7.1	0.58
	+ HypE	1.4	27.1	2.22
	+ HypE – CP	0.6	10.8	0.89

Finally, the HypE and HypF activities were measured in a coupled reaction in the presence and absence of carbamoyl phosphate (**Figure 26, Table 13**). To calculate the HypE activity, the slope of HypF alone was subtracted from the slope of the coupled reaction of HypE and HypF. Conversely, the activity of HypF was calculated by abstracting the slope of HypE alone from the combined slope of the coupled reaction.

Both the HypE and the HypF activity increased when both proteins were present in the assay, even in the absence of carbamoyl phosphate. This suggests that just complex formation of HypE and HypF has a beneficial effect on activity. In the presence of carbamoyl phosphate, however, the activity increase of HypE and HypF was even higher. In summary, the measurements demonstrate that purified HypF and HypE are active and can be employed in the future in an enzymatic *in vitro* assay to assemble the Fe(CN)₂(CO) cofactor on Fe-reconstituted apo-HypCD.

3.2.5. Transfer of the Fe(CN)₂(CO) moiety to the [NiFe]-hydrogenase large subunit

One crucial step in maturation is the transfer of the Fe(CN)₂(CO) complex from HypCD to the apo-form of the [NiFe]-hydrogenase large subunit. To investigate this process in detail, we developed an *in vitro* transfer assay using *E. coli* holo-HypCD and the *R. eutropha* MBH large subunit, HoxG. Purification of isolated HoxG has recently been established in our group, and the maturation intermediate, apo-HoxG, lacking the Fe(CN)₂(CO) moiety, has already been characterized (Hartmann et al. 2018). For the transfer assay we used, however, a modified version of apo-HoxG carrying a Strep-tag on its N-terminus instead of the C-terminus. The corresponding protein was encoded on pGC50. Plasmid pGC50 was transferred to *R. eutropha* HF497, which carries inframe deletions in *hypD*, *hoxH* and *hoxG*. This resulted in the apo-HoxG production strain *R. eutropha* HP68. The absence of the NiFe(CN)₂(CO) moiety, in purified apo-HoxG was verified by IR spectroscopy (**Figure 27 A and B**). To enable separation of apo-HoxG from a transfer reaction mix with HypCD, holo-HypCD and for future chemical reconstitution experiments also apo-HypCD were equipped with a hexa-His tag at the C-terminus of HypC (see Materials and Methods, **Table 2**) and both forms were purified via Ni-NTA affinity chromatography (**Figure 27 A**). The presence or absence of the Fe(CN)₂(CO) moiety in His-tagged HypCD was confirmed by IR spectroscopy (**Figure 27 B**). The transfer assay was set up under anaerobic conditions in an anaerobic workstation. Apo-HoxG was pre-incubated with NaDT before a 5-fold molar excess of holo-HypCD_{His} was added. The transfer mix was incubated for 1 h and subsequently purified via Strep-Tactin affinity chromatography. Apo-HoxG harbored a Strep-tag and remained on the column while His-tagged holo-HypCD did not bind to the Strep-Tactin column and was washed off. In this way, the flow through and washing fractions contained HypCD, whereas the elution fraction contained just apo-HoxG which was verified by SDS-PAGE (**Figure 27 C and D**). Eluted apo-HoxG was then concentrated and subjected to IR analysis. The IR spectrum lacks the characteristic CN/CO bands, showing that the Fe(CN)₂(CO) moiety was not transferred. Additionally, the SDS gel shows no HypC co-eluted with apo-HoxG indicating that there was no stable complex formation between *E. coli* HypC and *R. eutropha* HoxG. The same has also been observed for *R. eutropha* HypC which did not form a stable complex with *R. eutropha* pre-HoxG (Ludwig et al. 2009). Different transfer conditions were tested, none of them were so far successful.

Results

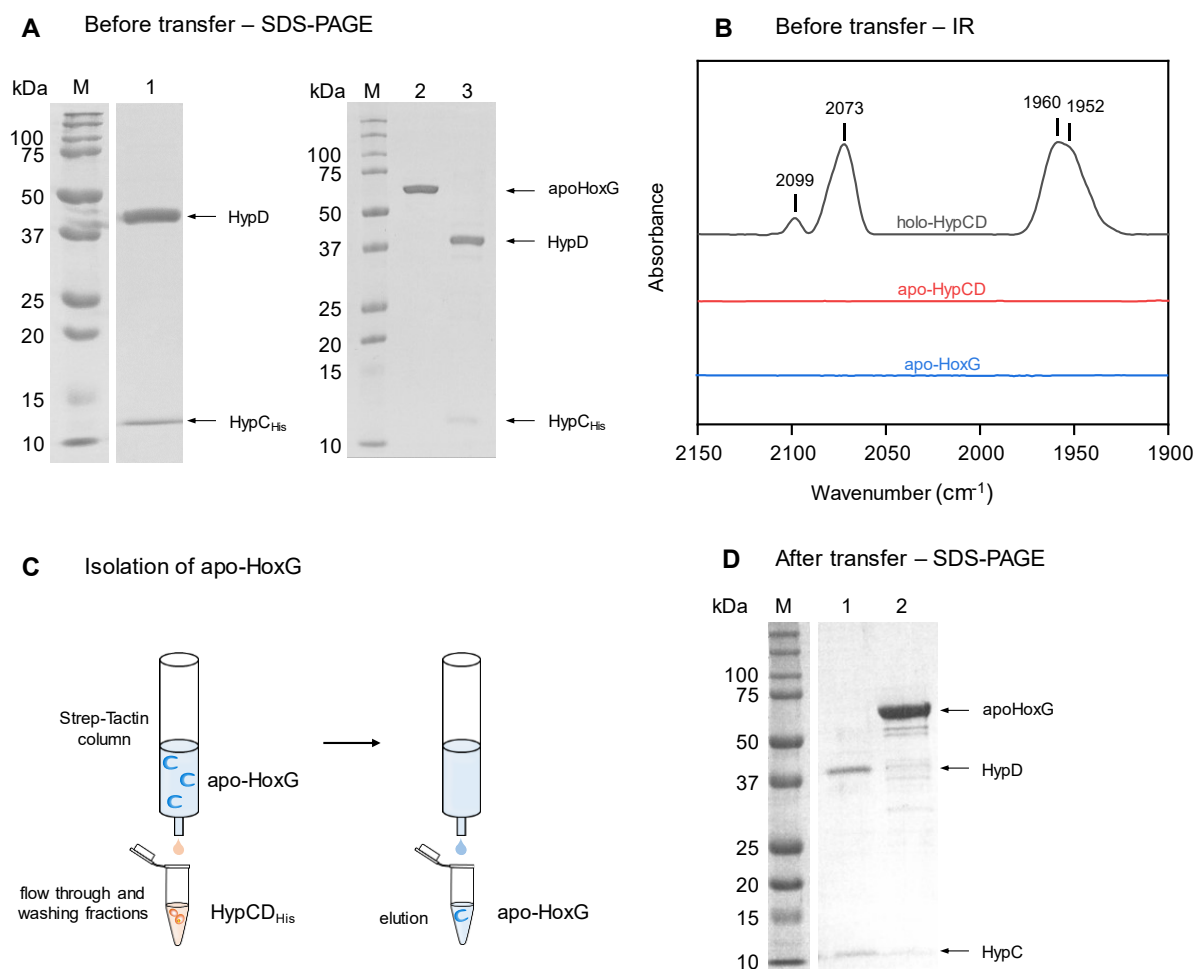


Figure 27. Transfer assay of the $\text{Fe}(\text{CN})_2(\text{CO})$ moiety from holo-HypCD_{His} to apo-HoxG. (A) SDS-PAGE gels of purified apo-HypCD_{His} (4 μg , lane 1), holo-HypCD_{His} (3 μg , lane 3) and apo-HoxG (2 μg , lane 2) before the transfer. (B) IR spectra of holo-HypCD_{His} (grey) and apo-HypCD_{His} (red) before the transfer, (C) cartoon of the isolation procedure of apo-HoxG, (D) SDS-PAGE gel of holo-HypCD_{His} (lane 1) and apo-HoxG (lane 2) after the transfer reaction. All SDS gels were composed of 12.5 % Acrylamide and stained with Coomassie brilliant blue. Lane M contains a protein standard. The corresponding molecular masses are indicated.

3.3. HypX synthesizes the active site CO ligand in O₂-tolerant [NiFe]-hydrogenases

Assembly of the NiFe(CN)₂(CO) active site in [NiFe]-hydrogenases requires the activity of at least six maturation proteins, named HypA-F (Böck et al. 2006). An additional seventh maturation protein, HypX, occurs exclusively in microorganisms synthesizing [NiFe]-hydrogenases under oxic conditions (Buhrke and Friedrich 1998). Previous studies in our group showed that HypX catalyzes the aerobic CO ligand biosynthesis using N¹⁰-formyl-THF as substrate (Bürstel et al. 2016). To obtain detailed insight into the reaction mechanism, purified *R. eutropha* HypX protein was subjected to a comprehensive biochemical analysis in this study. Additionally, thermostable HypX protein from the thermophilic strain *Hydrogenophlius thermoluteolus* was investigated with the aim of protein crystallization.

3.3.1. MBP-HypX is functional *in vivo*

It was shown previously, that HypX from *R. eutropha* can be heterologously produced in *E. coli*. Fusion of a maltose binding protein (MBP) to the N-terminal end of HypX allowed purification of MBP-HypX protein from the soluble cell extract (Bürstel et al. 2016).

The functionality of the MBP-HypX fusion protein was confirmed in *in vivo* growth experiments (**Figure 28**). Plasmid pTS1 containing *malE-hypX*, encoding MBP-HypX, was transferred into the HypX-deficient mutant strain *R. eutropha* HF469 (Buhrke and Friedrich 1998). Deletion of *hypX* resulted in a considerable growth delay of the mutant strain HF469 compared to the wild type *R. eutropha* H16 when grown lithoautotrophically on H₂ and at high O₂ concentrations at which hydrogenase biosynthesis requires HypX for CO ligand synthesis (Bürstel et al. 2016). Therefore, the MBP-HypX fusion protein, encoded on plasmid pTS1, was tested for its ability to restore wild type-like growth of the *hypX* deletion strain under high O₂ concentrations. The strains, *R. eutropha* HP77, carrying the plasmid pEDY309, and *R. eutropha* HP74, carrying plasmid pTS2 encoding untagged HypX, served as controls. Cultures were grown under a gas mixture composed of 4 % H₂, 15 % O₂, 10 % CO₂ and 71 % N₂. Both *hypX* mutant strains, *R. eutropha* HF469 and HP77, showed a considerable lag phase when compared to wild-type *R. eutropha* H16. The presence of plasmid pTS1, encoding MBP-HypX, in the *hypX* deletion strain (*R. eutropha* HP73) significantly reduced the growth delay.

Results

Restoration of wild type-like growth was also observed for strain *R. eutropha* HP74, expressing untagged *hypX*. These results demonstrated that MBP-HypX is functionally active *in vivo*.

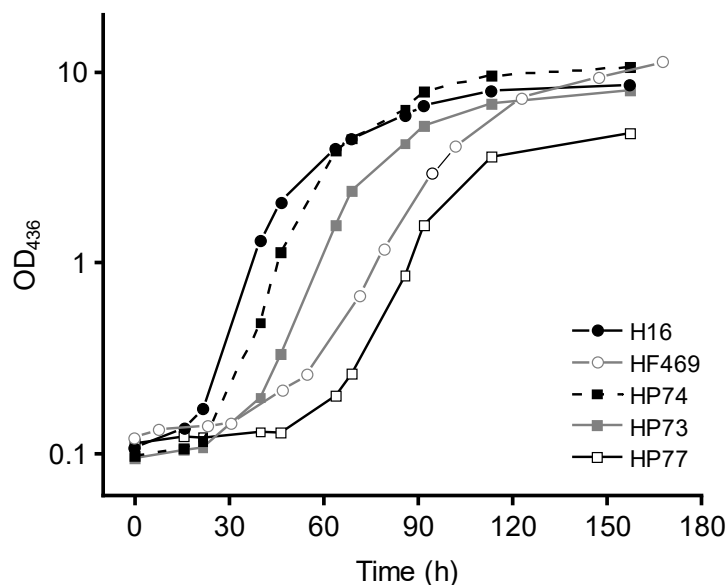


Figure 28. MBP-HypX is functional *in vivo*. The $\Delta hypX$ strain *R. eutropha* HF469 was complemented with plasmids carrying *malE-hypX* (pTS1) and native *hypX* (pTS2). Lithoautotrophic growth of wild-type *R. eutropha* H16, and the recombinant strains HF469 ($\Delta hypX$), HP74 (HF469(pTS2)), HP73 (HF469(pTS1)), and HP77 (HF469(pEDY309)). Main cultures were inoculated to an OD_{436} of 0.1 and then grown in minimal medium under a gas mixture composed of 4 % H_2 , 15 % O_2 , 10 % CO_2 and 71 % N_2 .

3.3.2. MBP-HypX produces CO *in vitro*

Since MBP-HypX was functional *in vivo*, we next sought to analyze the protein *in vitro*. MBP-HypX was purified to homogeneity via affinity chromatography (**Figure 29**). Because purified MBP-HypX showed a slightly brownish color indicating the presence of Fe, the metal content of MBP-HypX was determined by ICP-OES. In contrast to previous results (Bürstel et al. 2016), the new results identified MBP-HypX as a metal-free enzyme (**Table 14**).

Results

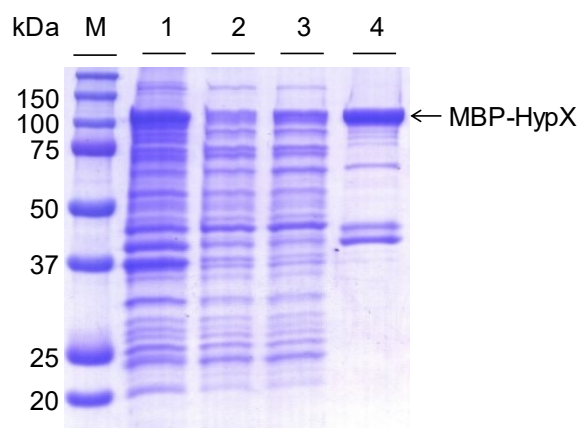


Figure 29. Purification of MBP-HypX visualized on an SDS-PAGE gel. Samples of different purification steps were separated on a 12.5 % SDS-gel, which was stained with Coomassie Brilliant Blue. Samples: 1 μ l soluble extract (lane 1), 1 μ l flow through (lane 2), 10 μ l washing fraction (lane 3) and 6 μ g of the elution fraction after affinity chromatography (lane 4). Lane M contains a protein standard with the corresponding molecular masses indicated. MBP-HypX with a molecular mass of 110 kDa is indicated by an arrow. Impurities at a height of about 44 kDa might correspond to free MBP.

Table 14. Metal content of purified MBP-HypX determined via ICP-OES.

Metal	μ M	Metal per protein
Co	0.072 ± 0.022	0.007 ± 0.002
Zn	0.849 ± 0.003	0.085 ± 0.000
Fe	0.482 ± 0.015	0.048 ± 0.001

According to previous *in vivo* studies, HypX converts the formyl group of N^{10} -formyl-THF into CO (Bürstel et al. 2016). CO production can be monitored spectrophotometrically using deoxyhemoglobin (deoxyHb) as reporter compound (Shepard et al. 2010; Esselborn et al. 2013). DeoxyHb binds CO with high affinity yielding carboxyhemoglobin (HbCO). Formation of HbCO leads to a specific shift of the heme Soret band from 430 nm (deoxyHb) to 419 nm and a corresponding splitting of the absorbance maximum at 555 nm. CO formation by purified HypX was measured as an increase of the absorbance at 419 nm over time. Sequence similarity of the C-terminal HypX module to enoyl-CoA hydratases/isomerases suggested that CoA may be involved in the reaction, which is why HypX activity was tested in the presence and the absence of CoA (**Figure 30**).

Results

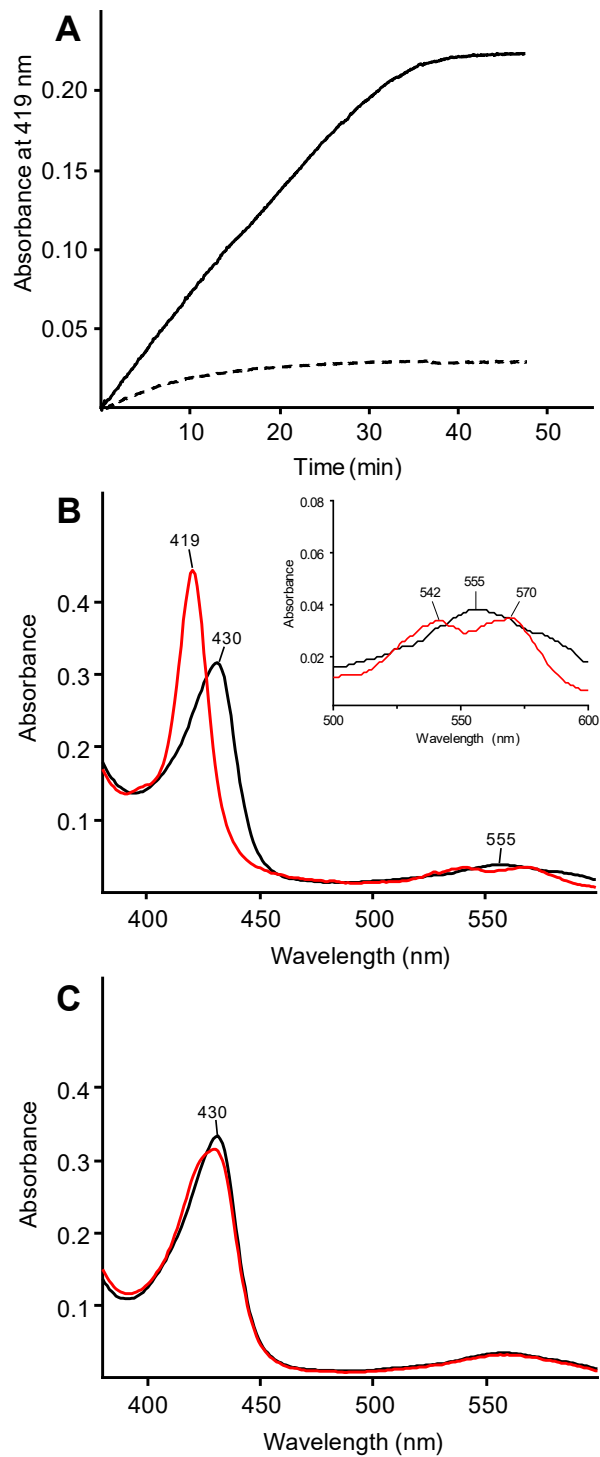


Figure 30. HypX-dependent CO formation *in vitro*. (A) Single-wavelength kinetics at 419 nm showing HbCO formation over time in the presence (solid line) and absence of CoA (dashed line). HbCO formation in the presence (B) and the absence (C) of additional CoA was also verified by the shift of the Soret band from 430 to 419 nm and the splitting of the signal at 555 nm. Black traces, absorption spectra before initiation of the reaction; red traces, absorption spectra after completion of the reaction. The inset in panel B provides a detailed view of the spectra around 550 nm.

Results

In the presence of CoA, single-wavelength kinetics at 419 nm revealed linear HbCO formation with a $k_{\text{cat}} = (1.85 \pm 0.12) \text{ h}^{-1}$ (**Table 15, Figure 30 A**). The corresponding K_{M} value determined for the substrate N^{10} -formyl-THF was $(185 \pm 35) \mu\text{M}$ (**Figure 31**). The steady state reaction proceeded until the deoxyHb in the assay was fully converted into HbCO. UV-Vis spectra taken before and after the reaction revealed a distinct shift of the Soret band and the specific splitting of the 555 nm signal, verifying the formation of HbCO (**Figure 30 B**). Notably, supplementation of the reaction with reductant in the form of mercaptoethanol or dithiothreitol did not affect the CO-releasing activity of HypX (not shown).

In the absence of CoA, only minor activity was detectable. The reaction stopped substantially earlier, and the spectra showed only a slight shift of the Soret peak at 430 nm (**Figure 30 C**).

Table 15. K_{M} and k_{cat} values for N^{10} -formyl-THF and Formyl-CoA

	K_{M} (μM)	k_{cat} (h^{-1})
N^{10} -formyl-THF	185 ± 35	1.85 ± 0.12
Formyl-CoA	107 ± 17	3.56 ± 0.25

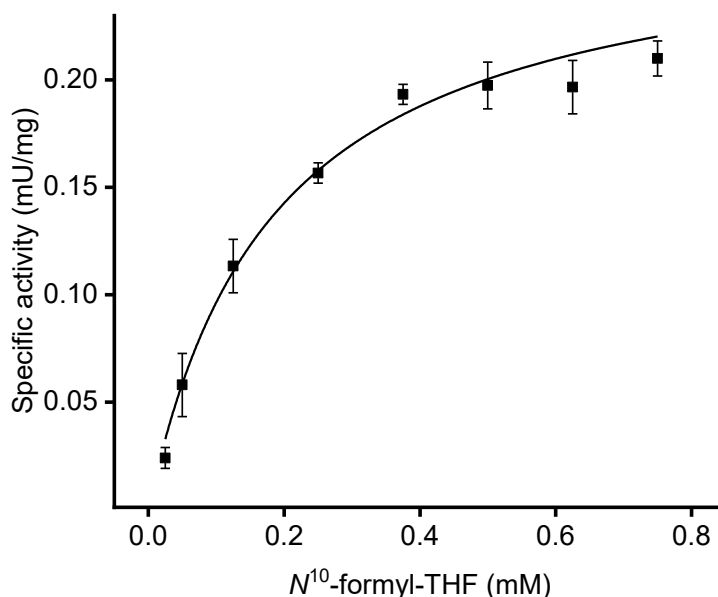


Figure 31. Determination of the K_{M} value for N^{10} -formyl-THF. MBP-HypX-dependent CO production was measured in the presence of $50 \mu\text{M}$ CoA and $0.025 - 0.75 \text{ mM}$ of N^{10} -formyl-THF. The Michaelis constant and the v_{max} value were determined by non-linear regression.

3.3.3. Coenzyme A is required for HypX activity and HypX stabilization

To test whether the residual activity observed in the assay without CoA (**Figure 30 B**) is due to CoA that was co-purified with HypX, the CoA content of the purified enzyme was quantified using a commercial CoA Assay kit specific for free CoA (CoA-SH). Purified HypX was heat-precipitated, and the CoA concentration of the supernatant was determined. As-purified HypX contained $(57 \pm 5) \%$ CoA, which explains the low activity measured in the absence of supplementary CoA. It does not explain, however, why the reaction stopped early (**Figure 30 A**). Assuming that CoA is a required co-substrate, a decreased but continuous reaction would be expected. Strikingly, the HypX activity was not recovered just by adding CoA to the assay, indicating that CoA-depleted HypX loses activity irreversibly under these conditions. Thus, we tested whether CoA confers a stabilizing effect to HypX. As-purified enzyme was incubated at 30 °C in buffer supplemented with either a 5-fold molar excess of CoA or without additional CoA. Samples were taken at different time points, and the CO release was measured in an assay containing 50 μM CoA. HypX incubated without supplementary CoA quickly lost activity, whereas the activity of HypX incubated with CoA remained constant over a period of 90 min (**Figure 32**).

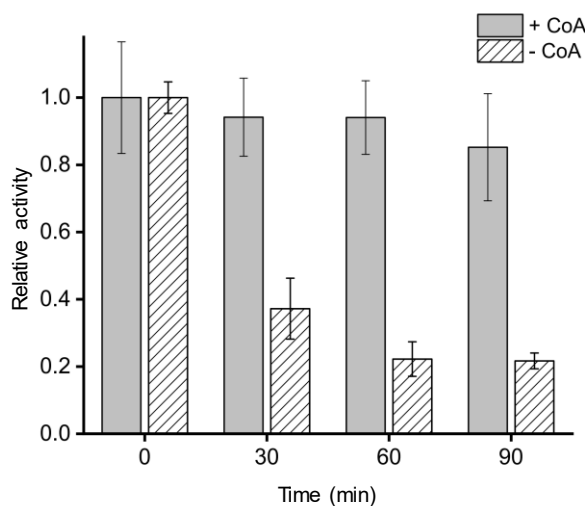


Figure 32. CoA stabilizes HypX. MBP-HypX was incubated at 30 °C without CoA (hatched bars) or with a 5-fold molar excess of CoA (grey bars). The activity was determined at different time points in an activity assay containing 50 μM CoA.

3.3.4. Formyl-CoA is a reaction intermediate

As mentioned above, the N- and C-terminal HypX modules share striking similarities with N^{10} -formyl-THF transferases and members of the enoyl-CoA hydratases/isomerases family, respectively. This fact in addition to the CoA dependence of the *in vitro* activity of HypX suggested a two-step reaction mechanism in which the formyl group of N^{10} -formyl-THF is first transferred to CoA presumably resulting in formyl-CoA as a reaction intermediate. To investigate this hypothesis, we sought to use formyl-CoA as substrate for HypX. Since formyl-CoA is not commercially available, we chemically synthesized formyl-CoA in cooperation with Phillip Pommerening from the group of Martin Oestreich at TU Berlin as described in the Materials and Methods chapter 2.22. Synthesized formyl-CoA was then used as the sole substrate for HypX in an activity assay with deoxyHb as reporter. CO was formed with a k_{cat} of $(3.56 \pm 0.25) \text{ h}^{-1}$ (Table 15). The K_M for formyl-CoA was determined with $(106.6 \pm 16.8) \mu\text{M}$ (Table 15, Figure 33), demonstrating that formyl-CoA is indeed a true reaction intermediate in the conversion of N^{10} -formyl-THF into CO.

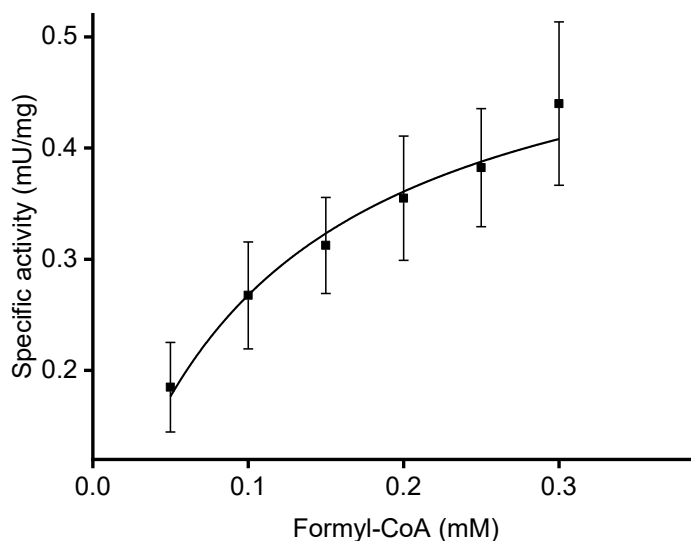


Figure 33. Determination of the K_M value for formyl-CoA. MBP-HypX-dependent CO production was measured with 0.05 – 0.3 mM formyl-CoA. The Michaelis constant and the v_{max} value were determined by non-linear regression.

It must be noted, however, that the chemically synthesized formyl-CoA contained $(66.2 \pm 1.3) \%$ free CoA. Therefore, potential effects of free CoA on the formyl-CoA conversion were investigated. The specific CO formation activity of MBP-HypX was measured at a constant

Results

formyl-CoA concentration in the presence of various amounts of free CoA. Indeed, the HypX activity decreased with increasing CoA concentration demonstrating that free CoA confers an inhibitory effect on formyl-CoA conversion (**Figure 34**). Due to the high similarity of the two molecules, it can be assumed that formyl-CoA and free CoA both bind at the same site within the C-terminal HypX module. Thus, free CoA presumably competitively inhibits formyl-CoA conversion, resulting in an overstated K_M value. Furthermore, due to the high content of free CoA in the formyl-CoA preparation, the true k_{cat} is presumably higher than that determined with the “impure” formyl-CoA. Nonetheless, the apparent k_{cat} and K_M values determined with formyl-CoA are comparable to the corresponding values determined for N^{10} -formyl-THF (**Table 15**). Furthermore, they are in the range of the rates reported for HydG-catalyzed CO production by the [FeFe]-hydrogenase maturation machinery (Shepard et al. 2010).

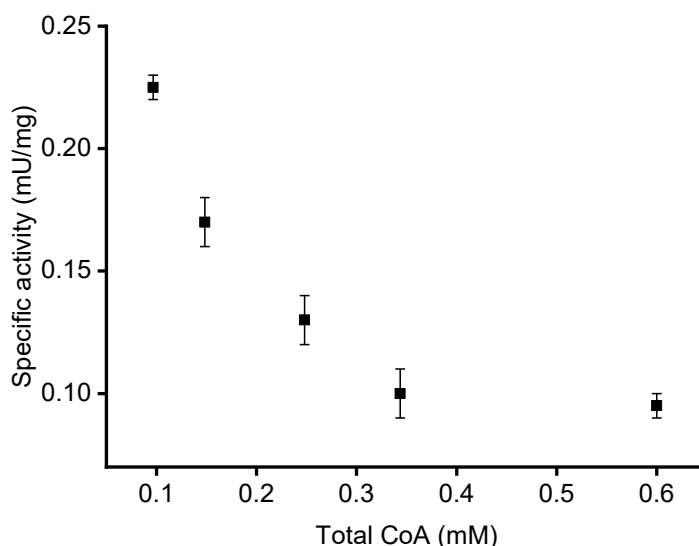


Figure 34. Inhibition of formyl-CoA-dependent CO release by free CoA. Specific HypX activity was measured at constant formyl-CoA concentration (0.05 mM formyl-CoA containing 0.1 mM CoA) and varying CoA concentrations. CoA was added at concentrations between 0 – 0.5 mM resulting in a total CoA concentration of 0.1 – 0.6 mM in the assay.

3.3.5. Glu449 is essential for HypX activity

A sequence alignment of the putative C-terminal CoA binding region of HypX homologues from different organism allowed the identification of invariant amino acids (**Figure 35A**). Based on the recently published crystal structure of HypX from *A. aeolicus*, the authors proposed that the conserved residues Tyr416 and Glu426 in the C-terminal module play an important role in CO release from formyl-CoA (**Figure 35B**) (Muraki et al. 2019). This

Results

proposal is consistent with previous observations that exchanges of the corresponding residues in *R. eutropha* HypX, Tyr439 and Glu449, confer a HypX⁻ phenotype (Bürstel et al. 2016). Thus, the amino acid exchanges Y439F, and E449Q were introduced into MBP-HypX to test their effect on HypX activity in vitro. Furthermore, an S448A variant was constructed. Besides Y439 and E449, S448 is also highly conserved among HypX orthologues (**Figure 35A**), and its exchange revealed the HypX⁻ phenotype (Bürstel et al. 2016).

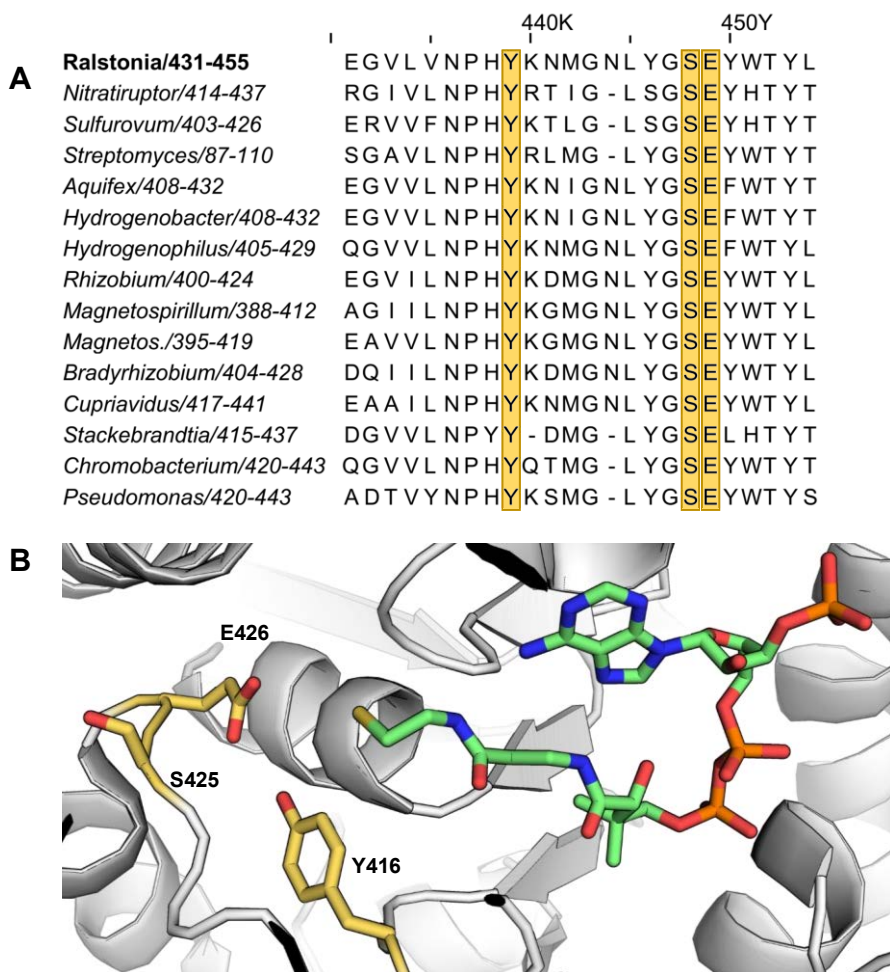


Figure 35. Sequence alignment and structure of the C-terminal Co-A binding region in HypX. (A) Sequence alignment of HypX homologues from the following organisms: *Nitratiruptor* sp. SB155-2, *Sulfurovum* sp. NBC37-1, *Streptomyces avermitilis* MA-4680, *Aquifex aeolicus* VF5, *Hydrogenobacter thermophilus* TK-6, *Hydrogenophilus thermoluteolus* TH-1, *Rhizobium leguminosarum*, *Magnetospirillum gryphiswaldense* MSR-1 (*Magnetospirillum*), *Magnetospirillum magneticum* AMB-1 (*Magentos.*), *Bradyrhizobium diazoefficiens*, *Cupriavidus metallidurans* CH34, *Stackebrandtia nassauensis* DSM 44728, *Chromobacterium violaceum*, *Pseudomonas fluorescens* Pf-5. The amino acid numbering of each sequence is given after the organism name. Conserved amino acids Y439, S448 and E449 (*R. eutropha* numbering) are marked in yellow. (B) Structure of the CoA binding region in *A. aeolicus* HypX (PDB: 6J0P, (Muraki et al. 2019)), conserved amino acid residues E426, S425 and Y416 (E449, S448 and Y439 in *R. eutropha* numbering) are shown in yellow, CoA is shown with green-colored carbon atoms. The figure has been generated using The PyMOL Molecular Graphics System, Version 2.3.3 Schrödinger, LLC.

Results

The three HypX variants were purified, and their CO-releasing activity was assayed with N^{10} -formyl-THF and formyl-CoA as the substrates (**Figure 36**). In case of the E449Q variant of MBP-HypX, BSA was added to the activity assay to prevent precipitation. As control experiment, the activity of native HypX was tested in the presence of BSA. No significant change in activity was observed. The variants Y439F and S448A showed significantly diminished activities for both substrates, ranging from 12 % to 28 % of those of native HypX (**Table 16**). Remarkably, the E449Q variant did not show any CO-releasing activity indicating that E449 is the key catalytic residue in CO synthesis from formyl-CoA.

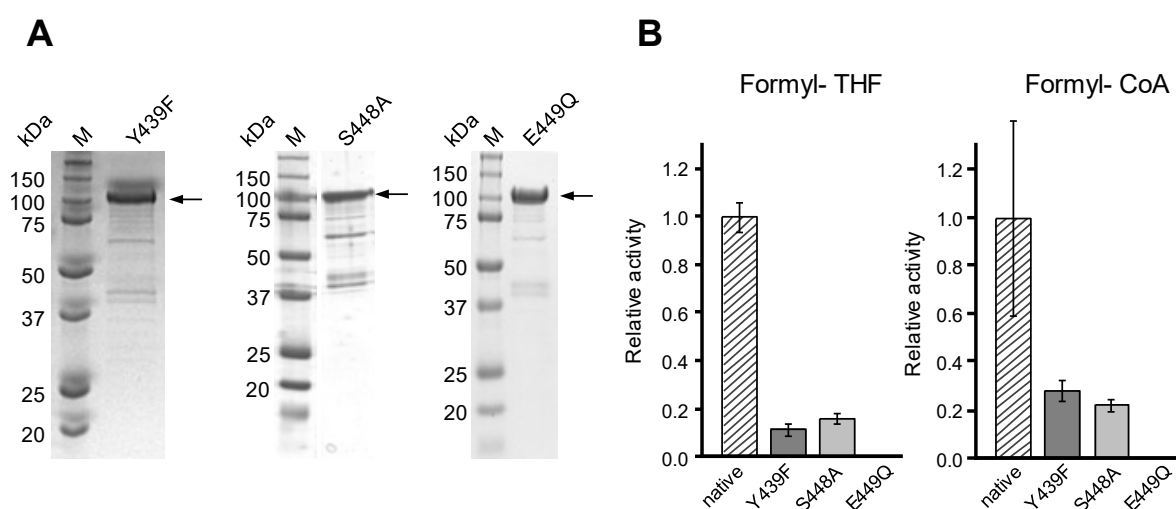


Figure 36. SDS-PAGE gel and CO-releasing activity of purified MBP-HypX variants Y439F, S448A and E449Q. (A) 3 μ g of each MBP-HypX variant were separated on a 12.5 % SDS gel and visualized by Coomassie staining. Lane M contains a protein standard with the corresponding molecular masses indicated. The arrow indicates the position of MBP-HypX variants with a molecular mass of 110 kDa. (B) Activity was measured with the substrates N^{10} -formyl-THF (left) and formyl-CoA (right) and compared to native HypX activity. The E449Q variant was inactive. Absolute activities are listed in **Table 16**.

Table 16. Specific and relative activity of native MBP-HypX and different HypX variants with N^{10} -formyl-THF and formyl-CoA as substrate.

	N^{10} -formyl-THF		Formyl-CoA	
	Specific activity (mU/mg)	Relative activity (%)	Specific activity (mU/mg)	Relative activity (%)
Native	0.22 ± 0.01	100 ± 6	0.35 ± 0.14	100 ± 41
Y439F	0.03 ± 0.01	12 ± 2	0.10 ± 0.02	28 ± 5
S448A	0.04 ± 0.01	16 ± 2	0.08 ± 0.01	22 ± 2
E449Q	inactive	inactive	inactive	inactive

Since the E449Q variant showed no C-terminal HypX activity, it might be used in future studies to accumulate formyl-CoA produced in the N-terminal module to additionally verify the proposed reaction mechanism. Formyl-CoA should be detectable by IR spectroscopy due to specific stretching vibration of the formyl-group. In a first trial, we analyzed the substrate N^{10} -formyl-THF by IR spectroscopy. In doing so, we recognized that very high concentrations in the mM range are required for its detection. We expect that similar concentrations are necessary for the detection of formyl-CoA, which, in turn, would require extremely high protein concentrations. This makes the IR-based experiment essentially not feasible.

3.3.6. Thermostable HypX from *H. thermoluteolus* (*HtHypX*)

As mentioned before, only microorganisms synthesizing [NiFe]-hydrogenases under oxic conditions possess HypX as additional maturase for the aerobic CO ligand synthesis. Besides *R. eutropha*, the moderate thermophilic β -proteobacterium *H. thermoluteolus* harbors a *hypX* gene. The investigation of thermostable HypX from *H. thermoluteolus* (*HtHypX*) is of special interest for protein crystallization attempts. An important factor for protein crystallization is protein stability. Since proteins isolated from thermophilic organisms feature enhanced stability, they are often better suited for protein crystallization than their mesophilic counterparts. A second important factor for protein crystallization is the purity and the conformational homogeneity of the protein. With the aim of protein crystallization, *HtHypX* was purified in two different variants, which were characterized biochemically.

HtHypX was heterologously produced in *E. coli* Rosetta™(DE3) carrying either plasmid pTS5 or pTS6. On plasmid pTS5, the *HthypX* gene is fused to *malE*, encoding an MBP-*HtHypX* fusion protein analogous to MBP-HypX from *R. eutropha*. In plasmid pTS6, the *malE* sequence is replaced by a Strep-tag sequence encoding Strep-*HtHypX* with a Strep-tag fused to the N-terminal end of *HtHypX*. Both *HtHypX* variants yielded soluble protein and were successfully purified via affinity chromatography (**Figure 37**). MBP-*HtHypX* has a theoretical molecular mass of 107 kDa. The SDS gel showed a main band at the corresponding height accompanied by few impurities, whereas the preparation of Strep-*HtHypX* had a higher purity. Only very few impurities were visible directly below the main band corresponding to Strep-*HtHypX* with a molecular mass of 67 kDa.

Results

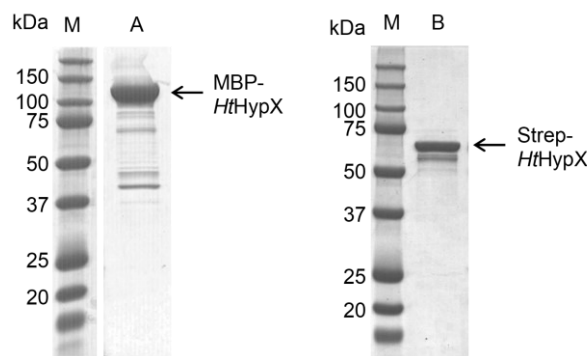


Figure 37. SDS-PAGE gel of purified MBP-*HtHypX* and Strep-*HtHypX*. MBP-*HtHypX* and Strep-*HtHypX* separated on a 12.5 % gel, visualized with Coomassie brilliant blue. Lane A contains 5 μg purified MBP-*HtHypX* with a theoretical molecular mass of 107 kDa, lane B contains 3 μg purified Strep-*HtHypX* with a theoretical molecular mass of 67 kDa, lane M contains a protein standard with the corresponding molecular masses indicated.

The CO-releasing activities of each *HtHypX* variant were measured at 30 and 50 $^{\circ}\text{C}$ with N^{10} -formyl-THF as substrate and in the presence of CoA. Because the molecular masses of the two *HtHypX* variants differ considerably and the activity in mU/mg would hence not be comparable, the apparent k_{cat} ($k_{\text{cat}}^{\text{app}}$) was calculated to allow proper comparison of the respective CO-releasing activities. The average specific activities and the corresponding $k_{\text{cat}}^{\text{app}}$ are listed in **Table 17**.

Table 17. Specific activity and $k_{\text{cat}}^{\text{app}}$ of MBP-*HtHypX* and Strep-*HtHypX*. Activities were measured at 30 and 50 $^{\circ}\text{C}$ with 0.5 mM N^{10} -formyl-THF as substrate in the presence of 50 μM CoA. The $k_{\text{cat}}^{\text{app}}$ was calculated from the average specific activity.

Temperature	MBP- <i>HtHypX</i>		Strep- <i>HtHypX</i>		
	Specific activity (mU/mg)	$k_{\text{cat}}^{\text{app}}$ (h^{-1})	Specific activity (mU/mg)	$k_{\text{cat}}^{\text{app}}$ (h^{-1})	k_{cat} (h^{-1})
30 $^{\circ}\text{C}$	0.20	1.29	0.36 ± 0.06	1.45 ± 0.24	
50 $^{\circ}\text{C}$	5.98	38.6	5.84 ± 0.34	23.52 ± 1.37	38.34 ± 0.88

The $k_{\text{cat}}^{\text{app}}$ values for CO release of MBP-*HtHypX* and Strep-*HtHypX* were very similar to each other at both assay temperatures of 30 $^{\circ}\text{C}$ and 50 $^{\circ}\text{C}$, indicating that the large MBP-tag (44 kDa) has no negative effect on the activity. This is in line with the results of the *in vivo* growth data with an *R. eutropha* ΔhypX strain, where the expression of *R. eutropha* *hypX* fused to *malE*, encoding MBP-HypX, restored a wild type-like phenotype (see chapter 3.3.1). Furthermore, the $k_{\text{cat}}^{\text{app}}$ values determined for MBP-*HtHypX* and Strep-*HtHypX* at 30 $^{\circ}\text{C}$ are

Results

in the same range as the k_{cat} for N^{10} -formyl-THF determined for *R. eutropha* MBP-HypX ($(1.85 \pm 0.12) \text{ h}^{-1}$), see chapter 3.3.2). The $k_{\text{cat}}^{\text{app}}$ calculated from the average activity of *R. eutropha* MBP-HypX with 0.5 mM formyl-THF ($(1.34 \pm 0.07) \text{ h}^{-1}$) is slightly lower than the actual k_{cat} determined from v_{max} and is similar to the $k_{\text{cat}}^{\text{app}}$ of the thermostable HypX variants.

For Strep-*HtHypX*, the k_{cat} for N^{10} -formyl-THF conversion at 50 °C was also deduced from non-linear regression. CO was formed with a maximum rate of $(38.34 \pm 0.88) \text{ h}^{-1}$, which is about 60 % higher than the determined $k_{\text{cat}}^{\text{app}}$ (see **Table 17**). The corresponding K_{M} value for N^{10} -formyl-THF is $(252 \pm 17) \mu\text{M}$ (**Figure 38**), which is slightly higher than the corresponding K_{M} of $(185 \pm 35) \mu\text{M}$ determined for *R. eutropha* MBP-HypX at 30 °C. The higher K_{M} value of Strep-*HtHypX* might be due to the temperature difference at which the two K_{M} values were determined, since the K_{M} value increases at higher temperatures.

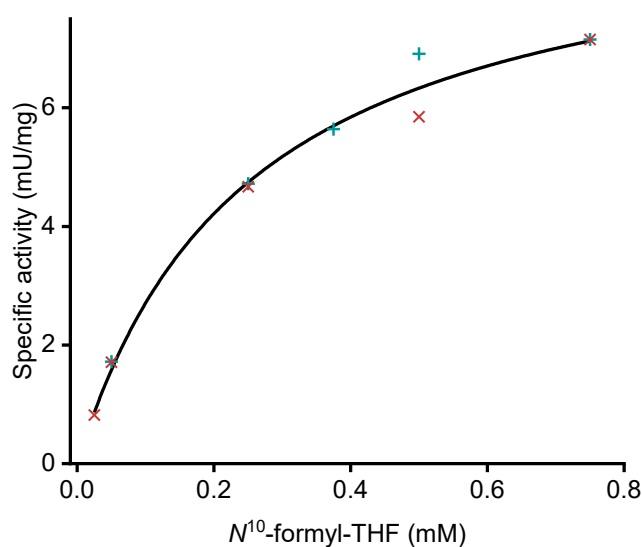


Figure 38. Determination of the Strep-*HtHypX* K_{M} value for N^{10} -formyl-THF. Strep-*HtHypX*-dependent CO production was measured with 0.025 – 0.75 mM N^{10} -formyl-THF at 50 °C. The Michaelis constant and the v_{max} value were determined by non-linear regression. One biological replicate with two technical replicates each were measured except for measurements with 0.025 and 0.375 mM N^{10} -formyl-THF where only one technical replicate was measured. Values of the two replicates are shown with symbols + and x.

Classically, fusion tags used for purification are removed by a specific endopeptidase prior to protein crystallization (Holcomb et al. 2017). MBP-*HtHypX* contains a recognition site for the endopeptidase Factor Xa in the linker region between the MBP-tag and *HtHypX*. It enables the specific cleavage of MBP and its subsequent removal in an additional purification step. Approximately 100 μg MBP-*HtHypX* were incubated at room temperature with 1 μg Factor

Results

Xa. Samples were taken at different time points and analyzed by SDS-PAGE for cleavage into MBP and *HtHypX* (**Figure 39 A**). No significant cleavage was observed even after more than 72 h of incubation. The resistance of some proteins to factor Xa is likely due to steric inaccessibility of the recognition site. In such cases, it is recommended to add 0.005 – 0.05 % (w/v) SDS to the reaction mix to relax the protein structure and make the cleavage site accessible for Factor Xa. SDS was added to the reaction mix in concentrations of 0.005, 0.025 and 0.05 % (w/v) and samples were analyzed by SDS-PAGE after 2, 4, and 6 h and after incubation overnight (**Figure 39 B**). None of the conditions resulted in a sufficient cleavage of the MBP-tag. MBP-*HtHypX* was either cleaved unspecifically resulting in the appearance of many smaller bands on the SDS gel or it was not cleaved at all.

Since Strep-fusion proteins are more commonly used for protein crystallization than MBP-fusions, the subsequent characterization of *HtHypX* was only performed with the Strep-tagged version.

Results

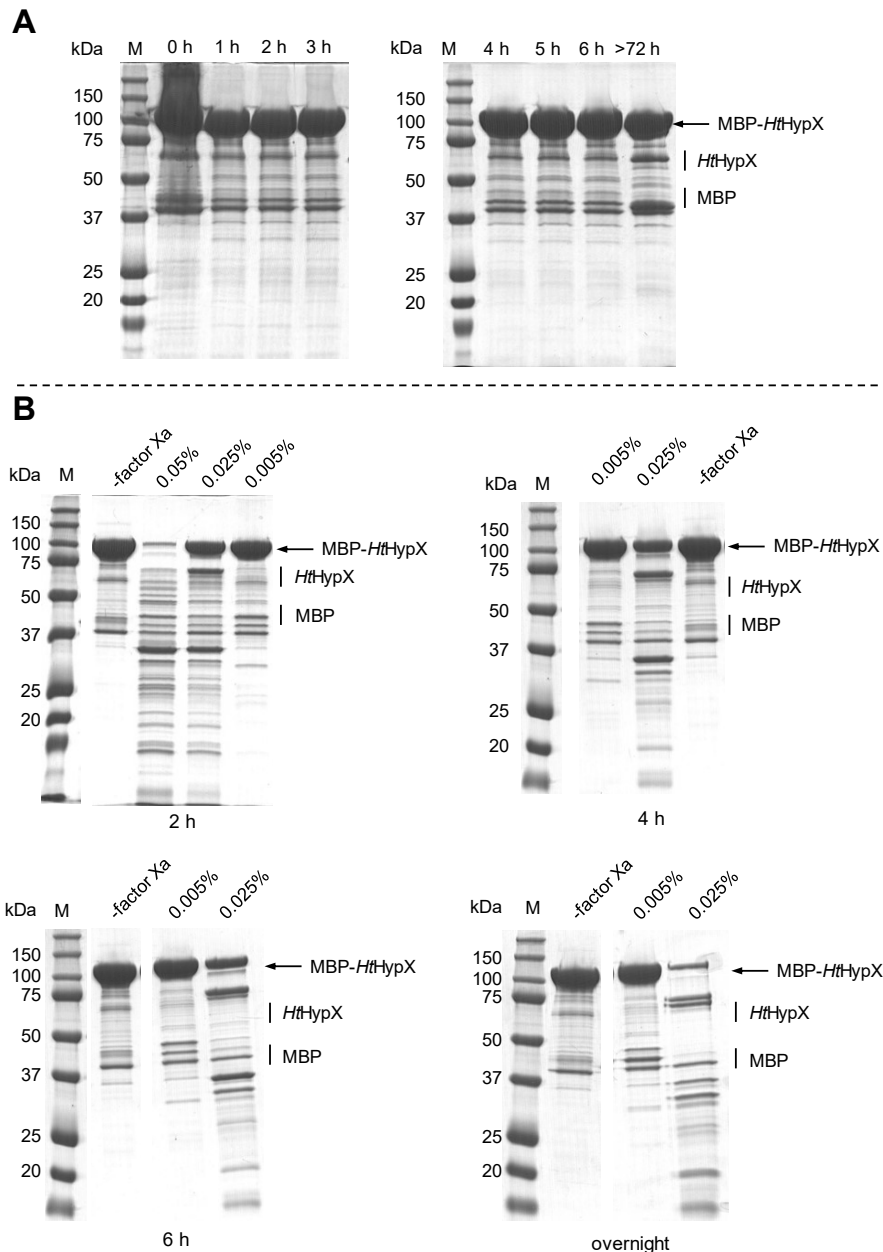


Figure 39. Purified MBP-*HttHypX* incubated with factor Xa. (A) Approximately 100 µg MBP-*HttHypX* protein were incubated at room temperature with 1 µg Factor Xa. Samples of 5 µl were taken every hour in the first six hours and after > 72 h and separated on a 12.5 % SDS gel and stained with Coomassie brilliant blue. The incubation time of each sample is indicated on top of each lane. (B) Modified Factor Xa digest of MBP-*HttHypX* with various SDS concentrations in the reaction mix in the range between 0.005 – 0.05 %. Samples of 5 µl of each digest were taken after 2, 4 and 6 h and overnight incubation and separated on a 12.5 % SDS gel, which was stained with Coomassie brilliant blue. The incubation time is indicated below the gels, SDS concentrations are indicated on top of each lane. As control MBP-*HttHypX* was incubated without factor Xa (lane -factor Xa). The arrows indicate the band corresponding to MBP-*HttHypX*, the lines indicate the height at which *HttHypX* and MBP are expected. Lane M contains a protein standard with the corresponding molecular masses indicated.

To test the CoA dependence of Strep-*HttHypX*, its CO-releasing activity was measured in an assay with or without CoA (**Figure 40, Table 18**). The activity in the presence of CoA was set

Results

as maximum activity of 100 %. In the absence of CoA, Strep-*HtHypX* showed diminished CO production with a rate of 45 %. To test whether the activity in the absence of CoA is due to CoA that was co-purified with HypX, as it was the case with *R. eutropha* HypX (see chapter 3.3.3), the CoA content in as-purified Strep-*HtHypX* was determined. CoA quantification was performed using Ellman's reagent (see Materials and Methods chapter 2.23) and revealed a CoA content of approximately 50 %, which correlates with the lower activity in the absence of CoA. In contrast to *R. eutropha* HypX, which is quickly inactivated in the absence of CoA, Strep-*HtHypX* stayed active and showed linear HbCO formation even in the absence of supplemental CoA. Thus, Strep-*HtHypX* seems to be more stable than *R. eutropha* HypX under these conditions.

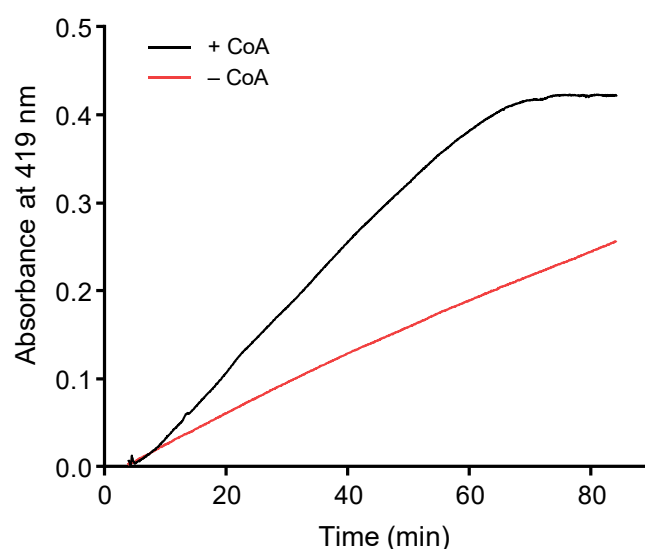


Figure 40. Strep-*HtHypX*-dependent CO formation. Single-wavelength kinetics at 419 nm of Strep-*HtHypX* showing CO formation over time at 30 °C. HypX-dependent CO production from *N*¹⁰-formyl-THF as substrate was measured with 50 μM CoA (black line) and without additional CoA (red line) in the assay.

Table 18. Specific and relative activities of Strep-*HtHypX*. The Strep-*HtHypX*-dependent conversion of *N*¹⁰-formyl-THF to CO was measured at 30 °C with 50 μM CoA (+CoA) or without CoA (- CoA) supplemented in the activity assay.

	Specific activity (mU/mg)	Relative activity (%)
+ CoA	0.42	100
- CoA	0.19	45

Results

Since *H. thermoluteolus* is a moderate thermophile with an optimal growth temperature of 52 °C (Goto et al. 1978), the temperature dependence of Strep-*HtHypX* was tested by measuring the CO release activity in the range of 30 – 65 °C (**Figure 41**). With N^{10} -formyl-THF as the substrate and in the presence of supplemental CoA, the highest activity was measured at 60 °C. It must be noted that the bovine hemoglobin used for CO detection starts to denature at 67 °C (Bull and Breese 1973) and is therefore suboptimal for measurements at high temperatures. Thus, the temperature optimum of *HtHypX* activity might be even higher than 60 °C as the temperature optimum for the thermostable SH from the same organism was at 80 °C (Preissler et al. 2018b).

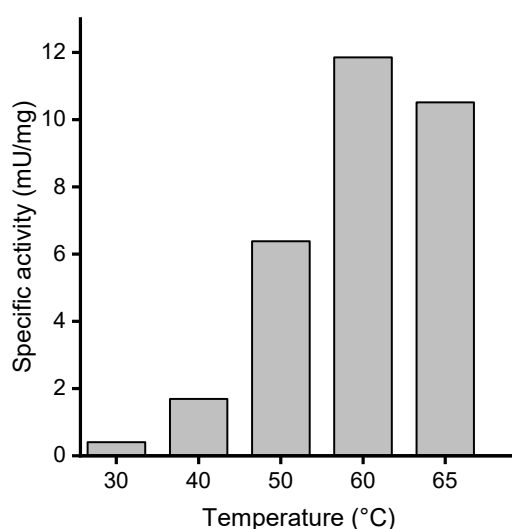


Figure 41. Temperature dependence of the CO-releasing activity of Strep-*HtHypX*. The activities were measured with N^{10} -formyl-THF as substrate and in the presence of 50 μ M CoA.

Besides protein stability, purity of the protein and conformational homogeneity are important factors affecting protein crystallization. For this reason, Strep-*HtHypX* was first isolated by Strep-Tactin affinity chromatography and further purified by size-exclusion chromatography (**Figure 42 A**). Size-exclusion chromatography was performed in CoA-containing buffer to obtain Strep-*HtHypX* in a homogeneous CoA-bound conformation, which might also enhance protein stability. Elution of the protein was followed at 280 nm in addition to 260 nm at which CoA has an absorbance maximum (note that also protein and DNA absorb at this wavelength). The chromatogram showed four absorbance maxima (Peaks 1 – 4, **Figure 42, A**). According to SDS-PAGE analysis, peaks 1 and 4 contained either no or little *HtHypX* and consequently showed no or only very low CO-releasing activity (**Figure 42, D**). However, peaks 2 and 3 both contained *HypX* protein, of which peak 3 showed the highest CO-releasing activity that

Results

was slightly higher (6.32 ± 0.12 mU/mg) than the initial activity after affinity chromatography (5.75 ± 0.36 mU/mg). By comparison with a calibration line, peak 2 and 3 could be identified as possible dimer and monomer of *HtHypX*, respectively (**Figure 42, C**). Dimeric Strep-*HtHypX* has a theoretical molecular mass of 134 kDa. It elutes at 13.6 ml which, based on the calibration line, corresponds to a molecular mass of about 98 kDa. The monomeric form elutes after 15.4 ml, which corresponds to a molecular mass of 43 kDa. The theoretical molecular mass of monomeric Strep-*HtHypX* is 67 kDa (including the Strep-tag). Differences between the theoretical molecular mass and the experimentally determined mass calculated on basis of the elution volume might be explained by a non-globular shape of the protein, which is known to affect the elution properties of proteins. To test whether the monomeric, most active form of *HtHypX* represents a stable oligomerization state, elution fractions corresponding to peak 3 were pooled and concentrated and rerun under identical conditions. Indeed, the chromatogram showed one main peak of monomeric *HtHypX* and almost no *HtHypX* dimer (**Figure 42, B**). Thus, size-exclusion chromatography provided homogeneous monomeric protein but, the purity could not be increased since the difference in size between the monomeric *HypX* protein and the contamination is too small to be separated by size-exclusion chromatography. The SDS gel still showed impurities right below the main band of Strep-*HtHypX* (**Figure 42 D**).

Results

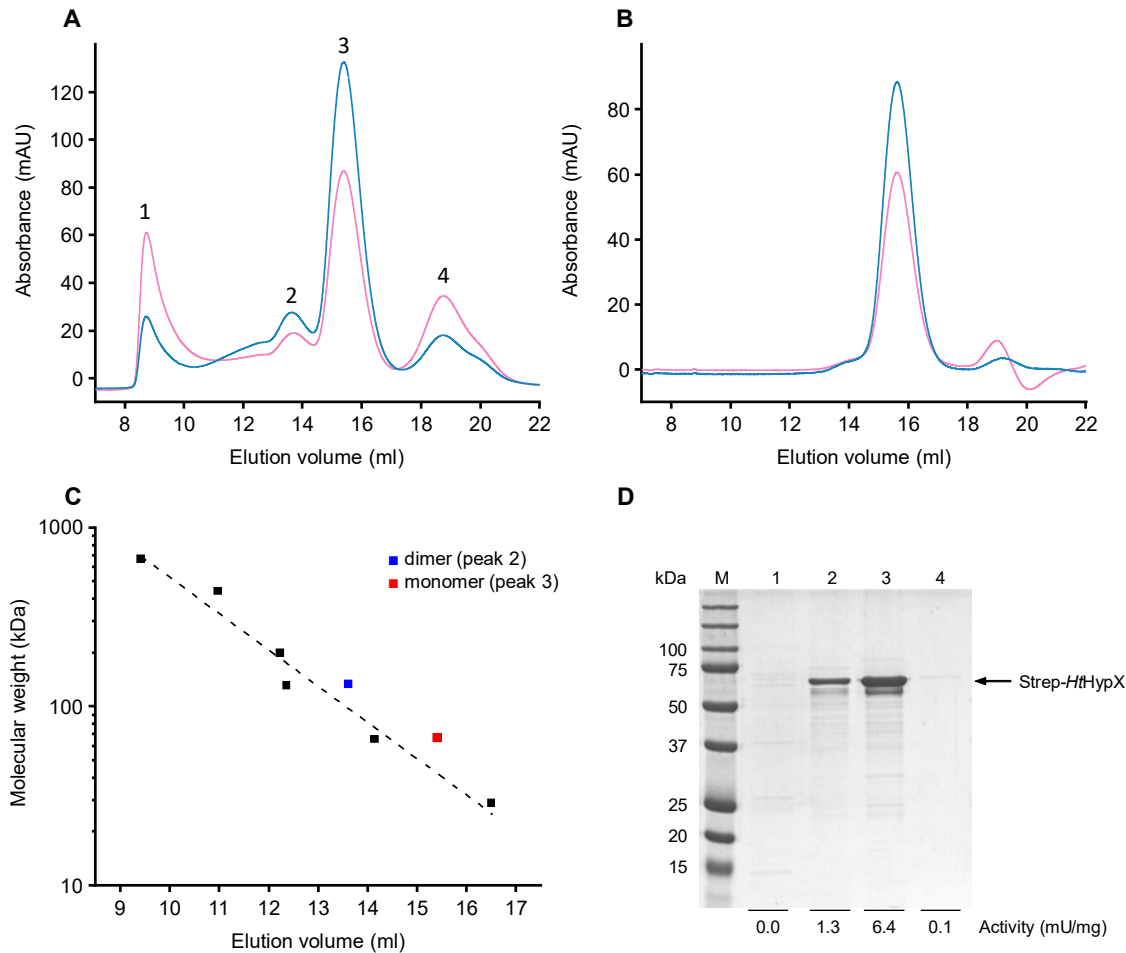


Figure 42. Size-exclusion chromatography (SEC) of Strep-*HtHypX*. SEC was performed in 20 mM Tris-HCl pH 7.4 at 4 °C, 150 mM NaCl and 0.05 mM CoA. Elution of the protein was monitored at 280 nm (blue) and 260 nm (pink). (A) SEC chromatogram of Strep-*HtHypX* after purification via affinity chromatography, (B) rerun of peak 3 containing monomeric Strep-*HtHypX*. (C) Calibration line of six standard proteins with molecular masses between 29 – 670 kDa. Peak 2 and 3 are plotted with the expected sizes of a dimer (■, 134 kDa) and a monomer (■, 67 kDa) against the corresponding elution volume of peak 2 and 3 (D) SDS-PAGE of Strep-*HtHypX* after size-exclusion chromatography. Lane 1 – 4 correspond to peak 1 – 4. 3 µg of each sample were separated on a 12.5 % SDS gel and stained with Coomassie brilliant blue. Lane M contains a protein standard with the corresponding molecular masses indicated. Specific activities measured at 50 °C with *N*¹⁰-formyl-THF as the substrate in the presence of CoA and at 50 °C are indicated below each lane.

To test whether the impurities running right below the main band of Strep-*HtHypX* correspond to proteolytically degraded Strep-*HtHypX*, Western blot analysis was performed with antibodies raised against the Strep-tag (**Figure 43**). Two bands appeared, demonstrating that the impurities indeed originated from the degradation of Strep-*HtHypX*. Since the antibodies can still bind to the N-terminally fused Strep-tag, degradation of the protein must occur at its C-terminus. To inhibit proteolytic degradation, the amount of protease inhibitor cocktail that was added to the resuspension buffer during the purification was doubled and the protein was

Results

purified via affinity chromatography and subsequent size-exclusion chromatography. Fractions including peak 3 were pooled, concentrated and checked for purity by SDS-PAGE (Figure 43, lane 3). Protein purified in this way had a higher purity and was used for crystallization trials, although proteolytic cleavage could not be prevented completely.

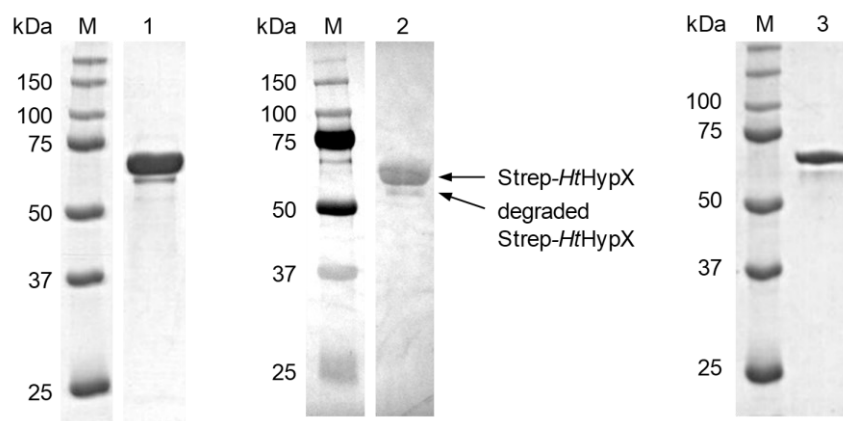


Figure 43. SDS-PAGE gel and immunological detection of purified Strep-*HttHypX*. Protein was purified via affinity chromatography and subsequent size-exclusion chromatography. 3 μg of protein were separated on a 12.5 % SDS gel and either stained with Coomassie brilliant blue (lane 1) or used for Western blotting with an anti-Strep antibody (lane 2). Lane 3 contains 3 μg purified Strep-*HttHypX* used for crystallization trials separated on a 12.5 % SDS-Gel. Lane M contains a protein standard with the corresponding molecular masses

Crystallization screenings were performed in collaboration with Berta Martins from the group of Holger Dobbek at HU Berlin at 10 and 18 $^{\circ}\text{C}$ using freshly purified protein in concentrations between 8 and 18 mg/ml. More than 700 different conditions were tested (see Materials and Methods chapter 2.27), however, none of them resulted in crystal growth.

4. Discussion

4.1. *HtSH* – a thermostable NAD⁺-reducing [NiFe]-hydrogenase

4.1.1. The CO stretching vibration at 1993 cm⁻¹ corresponds to an active site structure with the Glu32 carboxyl group coordinating the Ni

Recently, a thermostable, O₂-tolerant NAD⁺-reducing soluble hydrogenase from the thermophilic organism *H. thermoluteolus* (*HtSH*) has been for the first time biochemically and spectroscopically characterized (Preissler et al. 2018b). The IR spectroscopic analysis of *HtSH* in the oxidized state revealed a CO band with a very high stretching frequency at 1993 cm⁻¹. Such a high CO stretching frequency has so far been unprecedented in [NiFe]-hydrogenases. Almost at the same time, the first crystal structure of *HtSH* was published (Shomura et al. 2017). In the reduced state, the active site shows the standard configuration with Ni being coordinated by two terminal cysteines and two bridging cysteines. In the air-oxidized state, however, the active site of the *HtSH* large subunit HoxH shows an unusual coordination. The Ni is coordinated by three bridging cysteines and the carboxyl group of Glu32 binds to Ni as bidentate ligand, resulting in a six-fold coordination of the Ni.

The observations of the unusual high CO stretching frequency in the IR spectrum and the unprecedented coordination of the active site in the crystal structure raised the question if they can be related to each other. Our results suggest that the 1993 cm⁻¹ species indeed most likely corresponds to the active site configuration with Glu32 coordinating Ni. Furthermore, our results indicate that the bond formation between Glu-Ni is reversible and initiated upon O₂ exposure.

Three *HtSH* variants, each of them carrying another amino acid exchange for Glu32 in HoxH, were investigated by IR spectroscopy with regard to the occurrence of the 1993 cm⁻¹ species. Since this species is only formed in the oxidized state, all spectra discussed in the following were recorded in the as-isolated, aerobic and NAD⁺-oxidized state. The substitution of the Glu32 carboxyl side chain by a methyl or amide side chain of alanine (variant E32A) or glutamine (variant E32Q), respectively, resulted in an IR spectrum lacking the 1993 cm⁻¹ CO band (**Figure 13**). The spectra of both variants were comparable among each other but differed markedly from the spectrum of native *HtSH*. An assignment of the observed bands based on the comparison to native *HtSH* is rather difficult, since it is possible that the exchange of Glu32

Discussion

resulted in a significantly modified active site structure. However, the variant E32D, which also has a carboxyl group side chain, revealed a different spectrum compared to the variants E32A and E32Q. In fact, the spectral pattern of the E32D variant was similar to that of native *HtSH* including a high frequency CO band at 1998 cm^{-1} . The band positions are only slightly shifted with regard to native *HtSH*, probably caused by the shorter side chain of Asp compared to Glu. These results suggest that the active sites in native *HtSH* and the E32D variant are very similar to each other. The presence of a carboxyl group of either glutamate (native *HtSH*) or aspartate (variant E32D) resulted in a high frequency CO stretching vibration around 1993 cm^{-1} , suggesting that the CO stretching frequency at 1993 cm^{-1} observed in native *HtSH* indeed corresponds to the Glu-Ni coordination.

In the *Desulfovibrio fructosovorans* hydrogenase, by contrast, the exchange of Glu with Gln resulted in an IR spectrum that was very similar to that of native enzyme, whereas the spectrum of a Glu-to-Asp variant was substantially changed (Dementin et al. 2004). A similar observation has been made for *Pyrococcus furiosus* SH where the exchange of Glu to Gln had no effect on the spectroscopic properties of the enzyme (recorded only in the reduced state) (Greene et al. 2016). These results are the exact opposite of what we observed for *HtSH*, highlighting the unique role of Glu32 in *HtSH*.

4.1.2. The Ni-Glu configuration might represent a novel O₂ protection mechanism

What is the functional role of Glu32 in *HtSH*? Glu32 is strictly conserved in [NiFe]-hydrogenases and located nearby one of the terminal cysteines (Cys462) coordinating the active site Ni. It is supposed to be involved in the H⁺ transport between active site and the protein surface. During catalysis, the terminal cysteine accepts a proton, which, in a subsequent step, is proposed to be transferred to the conserved glutamate residue. Evidence for its function in H⁺ transfer was obtained from mutational, kinetic and spectroscopic studies (Greene et al. 2016; Dementin et al. 2004). The exchange of the corresponding glutamate residue in several [NiFe]-hydrogenases resulted in a diminished or completely abolished catalytic activity (Greene et al. 2016; Dementin et al. 2004; Gebler et al. 2007). The Glu-to-Gln variants of *D. fructosovorans* and *P. furiosus* hydrogenase, for example, showed a residual H₂ oxidation activity of less than 0.1 % and 19 % compared to native enzyme activity, respectively (Greene et al. 2016; Dementin et al. 2004). Similar effects were observed in the present study for the

Discussion

HtSH variants E32Q, E32A and E32D, which showed residual H₂ oxidation activities of 0.4 to 10 % compared to native *HtSH* activity pointing out the role of Glu32 as H⁺ acceptor. The residual activity of the variants also indicates the presence of a second H⁺ transfer pathway since the activity was not completely abolished. Besides the Cys-Glu pathway, a second H⁺ transfer pathway has been proposed, which involves a conserved arginine in the canopy region of the active site (Evans et al. 2016; Evans et al. 2018; Szóri-Dorogházi et al. 2012).

A second function of Glu32 in *HtSH* was proposed by Shomura and co-workers. The authors suggest that the Glu-mediated coordination of Ni observed in the aerobically oxidized crystals is a protection mechanism against oxidative damage by preventing O₂ from binding to the active site (Shomura et al. 2017). Since the 1993 cm⁻¹ band is reversible and disappeared upon incubation with TCEP, NADH and H₂, it is probably not related to (permanent) oxidative damage (Preissler et al. 2018b). The aerobic oxidation of reduced *HtSH* indicates that the 1993 cm⁻¹ band, and hence the Glu-Ni configuration of the active site, is induced upon O₂ exposure, whereas anaerobic oxidation of *HtSH* with [Fe(CN)₆]⁴⁻ did not lead to the formation of the 1993 cm⁻¹ species (personal communication Catharina Kulka, Charlotte Wiemann). In sum, these observations support the assumption of Shomura et al. that the reversible Ni-Glu coordination represents a novel protection mechanism against irreversibly oxidative inactivation (**Figure 44**). The 1993 cm⁻¹ species might be produced from the Ni_i-SI or Ni_i-B-like states in response to O₂. The six-fold coordination of Ni might thereby prevent binding of O₂ to the active site. This O₂ protection mechanism differs from the strategies of certain O₂-tolerant energy-conserving [NiFe]-hydrogenases that are not based on the prevention of O₂ to bind the active site but on its detoxification. *R. eutropha* MBH and closely related enzymes, for example, possess a novel [3Fe-4S] cluster, which enables O₂ detoxification by supplying additional e⁻ to the active site (Goris et al. 2011; Fritsch et al. 2011). The O₂ detoxification mechanism of *R. eutropha* SH is proposed to involve the formation of sulfoxxygenated active site species (Horch et al. 2015b). A similar mechanism to that of *HtSH* has been described for a [NiFeSe]-hydrogenase from *Desulfovibrio vulgaris* Hildenborough where the NiFeSe active site adopts a Ni-SeCys conformation hindering O₂ to bind to the active site (Marques et al. 2010; Marques et al. 2013) and for [FeFe]-hydrogenases from *Desulfovibrio desulfuricans* where the open coordination site is blocked by a sulfide bound to the distal Fe in the FeFe active site (Rodríguez-Maciá et al. 2020).

Discussion

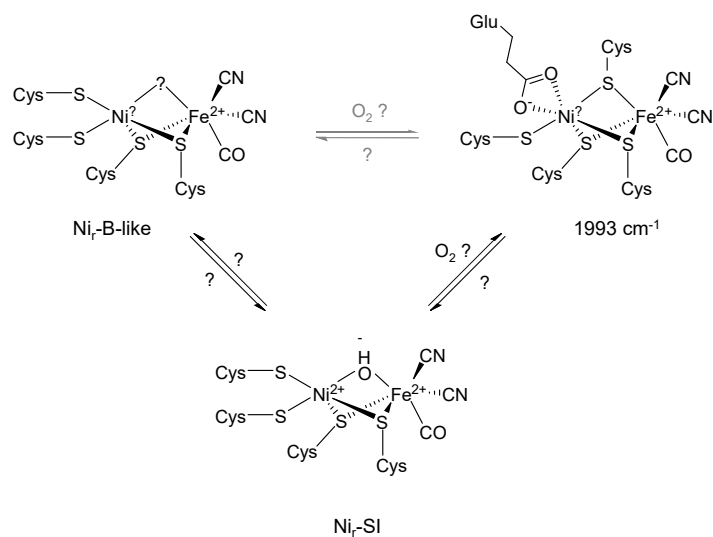


Figure 44. Proposed protection mechanism against irreversible oxidative inactivation of *HtSH*. Oxidation of *HtSH* leads to the formation of the Ni_r-SI state, the Ni_r-B-like state and the 1993 cm⁻¹ species. The 1993 cm⁻¹ species is induced upon O₂ exposure and might be formed by conversion of the Ni_r-SI state into the 1993 cm⁻¹ species. Interconversion between the 1993 cm⁻¹ species and the Ni_r-B-like state might also be possible.

4.2. Synthesis of the Fe(CN)₂(CO) moiety

The second part of this thesis focuses on the maturation of [NiFe]-hydrogenases, especially the synthesis of the Fe(CN)₂(CO) moiety. While the fundamental steps of the maturation and the assembly of the Fe(CN)₂(CO) moiety have been identified, a detailed understanding about some of the key processes still remains elusive. This includes the mechanism of the CN⁻ ligand transfer from HypE to HypCD, the order of ligand attachment and the transfer of the Fe(CN)₂(CO) moiety from HypCD to the apo-large subunit. Additionally, it has recently been shown that HypCD possess an ATPase activity with a yet unknown function (Nutschan et al. 2019).

Only limited information is available about the CO ligand synthesis. At least two pathways are proposed of which one is functional under anaerobic or microaerobic conditions and the other one is functional under aerobic conditions (Bürstel et al. 2011). Aerobic CO ligand synthesis requires an additional Hyp protein, namely HypX. Evidence for HypX-mediated CO ligand synthesis from *N*¹⁰-formyl-THF as substrate was obtained by *in vivo* hydrogenase maturation and ¹³C-labeling experiments (Bürstel et al. 2016). However, so far, no *in vitro* evidence for CO synthesis catalyzed by HypX has been shown.

Here we present preliminary work that forms the basis for following experiments in order to provide a better understanding of the HypCD-dependent maturation processes. Therefore, apo- and holo-HypCD were biochemically and spectroscopically investigated. Assays for the enzymatic and chemical assembly of the Fe(CN)₂(CO) moiety on the basis of apo-HypCD were designed. Apo-HypCD was reconstituted with a synthetic Fe(CN)₂(CO) moiety mimic, yielding artificially matured holo-HypCD.

Furthermore, we present *in vitro* evidence for HypX-mediated CO synthesis from *N*¹⁰-formyl-THF as substrate with formyl-CoA as intermediate. Exchanges of conserved amino acid residues within the active site revealed a glutamate to be essential for catalysis. Based on our results, the recently published crystal structure (Muraki et al. 2019) and sequence similarities of the two HypX modules to *N*¹⁰-formyltetrahydrofolate (*N*¹⁰-formyl-THF) transferases and enoyl-CoA hydratases/isomerases of the crotonase superfamily (Rey et al. 1996), we propose a two-step reaction mechanism.

4.2.1. HypCD - the scaffold for Fe(CN)₂(CO) moiety synthesis

The purification of *E. coli* apo- and holo-HypCD was performed as described previously (Blokesch et al. 2004b). IR spectroscopic analysis confirmed the absence of the Fe(CN)₂(CO) moiety in apo-HypCD and its presence in holo-HypCD. The IR spectrum of holo-HypCD showed two CN bands and two CO bands at similar positions as reported earlier (Bürstel et al. 2012; Soboh et al. 2012). UV-Vis spectroscopy revealed a broad maximum around 410 nm corresponding to the [4Fe-4S] cluster in HypD, which is consistent with previous observations (Soboh et al. 2012). For the first time, the [4Fe-4S] cluster was investigated by resonance Raman (RR) spectroscopy. By comparison of the RR spectra of holo- and apo-HypCD – the latter of which lacks the precursor Fe, as determined by ICP-OES – the observed Fe-S modes could be assigned to the [4Fe-4S] cluster. As already reported earlier (Roseboom et al. 2005), the [4Fe-4S] cluster was not fully reducible by an excess of NaDT ($E^{\circ'} - 660$ mV) although its redox potential was determined with $E^{\circ'} - 260$ mV (Adamson et al. 2017a). Signals attributable to the Fe(CN)₂(CO) moiety were, however, were not observed. Measurements at different excitation wavelengths might reveal features of the Fe(CN)₂(CO) moiety.

4.2.1.1. Chemical maturation of apo-HypCD as a tool to investigate the Fe(CN)₂(CO) moiety

ICP-OES analysis of holo- and apo-HypCD revealed that as-purified apo-HypCD contains one Fe/protein less compared to holo-HypCD. Thus, apo-HypCD lacks presumably the precursor Fe. In order to obtain apo-HypCD carrying the precursor Fe, we reconstituted apo-HypCD with Fe. The successful reconstitution was verified by ICP-OES. Since the Fe content of holo-HypCD was not increasing after Fe-reconstitution, we concluded that the additional Fe in apo-HypCD after Fe-reconstitution is indeed the precursor Fe.

The *in vitro* reconstitution of apo-HypCD with the precursor Fe, enables for the first time the spectroscopic investigation of the precursor Fe. Until now, there is no direct spectroscopic or structural evidence for the presence of the precursor Fe in HypCD. Isothermal titration calorimetry (ITC) analysis revealed only substoichiometric Fe binding to HypCD, but not HypD and HypC alone (Watanabe et al. 2012a). To investigate the coordination of the precursor Fe to HypCD, Resonance Raman spectroscopy could be used. Reconstitution with ⁵⁷Fe would enable the characterization via Mössbauer or nuclear resonance vibrational (NRV)

Discussion

spectroscopy without disturbance by the $[4^{56}\text{Fe}4\text{S}]$ cluster. Mössbauer Spectroscopy could be used to investigate the properties of the Fe species which might reveal valuable information about the chemistry of ligand attachment. Chemical modeling of the transfer of the CN moiety from a thiocyanate to an Fe revealed two possible mechanisms in which either a nucleophilic CN is transferred to an electrophilic Fe or an electrophilic CN is transferred to a nucleophilic Fe (Reissmann et al. 2003). Similar to resonance Raman spectroscopy, NRV spectroscopy could provide information about the coordination of the precursor Fe. These techniques do not only allow for the investigation of the precursor Fe but also of the $\text{Fe}(\text{CN})_2(\text{CO})$ moiety which, so far, has only been investigated by IR spectroscopy.

To study the individual steps of $\text{Fe}(\text{CN})_2(\text{CO})$ moiety synthesis, we aimed to develop an *in vitro* assembly assay using Fe-reconstituted apo-HypCD as scaffold. Two assembly assays were designed using either KCN and CO gas as ligand sources or HypE, HypF and HypX for enzymatic ligand synthesis. Ligand attachment was monitored by IR spectroscopy.

Until now, the enzymatic *in vitro* assembly assay was not tested but all required enzymes were successfully purified and checked for their functionality *in vitro*. Since *E. coli* does not possess HypX, *R. eutropha* HypX will be used. It has previously been shown that HypCD forms a complex with HypX (Muraki et al. 2019). To exclude compatibility problems, between *E. coli* HypCD and *R. eutropha* HypX, complex formation of the three proteins could be tested in advance. In the chemical assembly assay, KCN and CO gas were used as ligands. Fe-CN binding was observed, but the results are not yet conclusive. Incubation with CO gas did not lead to any observable CO binding to Fe-reconstituted apo-HypCD.

Successful *in vitro* assembly of the $\text{Fe}(\text{CN})_2(\text{CO})$ moiety would allow for the detailed investigation of the ligand transfer to HypCD. By incubation of Fe-reconstituted apo-HypCD separately with HypEF or HypX, the order of ligand attachment could be unraveled. Strong indication that CN^- ligation proceeds binding of CO derived from experiments with HypCD matured *in vivo*. Deletion of the CN^- synthesis pathway resulted in apo-HypCD without CN^- or CO ligands, although the CO pathway was not affected (Bürstel et al. 2012). The assumption that CO precedes CN^- ligation is based on IR spectroscopic analysis of holo-HypCD displaying all “typical” CO and CN bands. From an additional CO band at 1927 cm^{-1} , which was not accompanied with additional cyanide bands, the authors inferred that there was a portion of HypCD complex just equipped with CO. They interpreted this with CO being first attached to the complex (Stripp et al. 2014). It is important to mention, however, that until now, there is

no spectroscopic evidence for a “premature” HypCD complex carrying just CN or just CO. This observation and the fact that purified apo-HypCD lacks the precursor iron raises the question if the $\text{Fe}(\text{CN})_2(\text{CO})$ moiety is assembled at all on HypCD. Alternatively, HypCD could receive the fully assembled $\text{Fe}(\text{CN})_2(\text{CO})$ moiety and only serves as temporary carrier which delivers the $\text{Fe}(\text{CN})_2(\text{CO})$ moiety to the hydrogenase apo-large subunit.

In the third assay, we used a synthetic $\text{Fe}(\text{CN})_2(\text{CO})$ moiety mimic for the reconstitution of apo-HypCD. The successful loading of the cofactor mimic on HypCD was verified by IR spectroscopy. To further investigate if this chemically matured HypCD is functional active, it would be interesting to test the transfer of the synthetic $\text{Fe}(\text{CN})_2(\text{CO})$ moiety from HypCD to the hydrogenase apo-large subunit.

4.2.1.2. Transfer of the $\text{Fe}(\text{CN})_2(\text{CO})$ moiety

The detailed mechanism of the $\text{Fe}(\text{CN})_2(\text{CO})$ moiety transfer from holo-HypCD to the hydrogenase apo-large subunit remains still elusive. So far, the *in vitro* transfer of the $\text{Fe}(\text{CN})_2(\text{CO})$ moiety to the large subunit was only performed in an assay containing all Hyp proteins in one reaction mix (Senger et al. 2017). A detailed investigation of the transfer reaction was not possible in this assay. Since it has been shown that HypC and HypC homologues form a complex with the apo-large subunit, they are supposed to be involved in the $\text{Fe}(\text{CN})_2(\text{CO})$ moiety transfer (Drapal and Böck 1998; Magalon and Böck 2000; Blokesch and Böck 2002; Blokesch et al. 2001b).

Here, we tested the $\text{Fe}(\text{CN})_2(\text{CO})$ moiety transfer from holo-HypCD to the large subunit of *R. eutropha* MBH, HoxG. Apo-HoxG was chosen as recipient because its purification in the apo-form without $\text{NiFe}(\text{CN})_2(\text{CO})$ unit was already established in our group (Hartmann et al. 2018). So far, the transfer was not successful. Since it cannot be excluded that the transfer failed due to compatibility problems between *E. coli* HypCD and *R. eutropha* HoxG, a homologous transfer from *E. coli* HypCD to an *E. coli* apo-large subunit might be a more promising approach. Furthermore, the MBH maturation machinery includes two additional maturases, HoxL and HoxV, which are supposed to be involved in the transfer of the $\text{Fe}(\text{CN})_2(\text{CO})$ moiety to HoxG (Ludwig et al. 2009).

4.2.1.3. The recently discovered ATPase activity is independent of the Fe(CN)₂(CO) moiety and seems to depend on reducing purification conditions

Recently, an ATPase activity of the HypCD complex was discovered and to lesser extent also of the individual proteins HypD and HypC as well as the HypC paralogue, HybG, (Nutschan et al. 2019). We observed that the ATPase activity was independent of the Fe(CN)₂(CO) moiety, since apo- and holo-HypCD had the same activity. This is consistent with the results of Nutschan et al. where the ATPase activity of HypCD overproduced in wild-type *E. coli* strain was the same as that of HypCD purified from an *E. coli* $\Delta hypB-E$ mutant. (Nutschan et al. 2019). These results suggest that the ATPase activity is rather not required for the transfer of the Fe(CN)₂(CO) moiety. Furthermore, the disassembly of the HypCD complex into its individual constituents, HypC and HypD, has never been observed (Nutschan et al. 2019).

Nutschan et al. propose that the ATPase activity is involved in anaerobic CO ligand synthesis by reduction of CO₂. ATP hydrolysis would provide the energy to reduce CO₂, since the redox potential of FeS cluster is far too positive for CO₂ reduction. However, the addition of CO₂ seems to have no effect on the ATPase activity (Nutschan et al. 2019).

It is also possible that ATP hydrolysis is involved in the cyanation/carbonylation of HypCD or complex formation of HypCD with, e.g., HypE. Transfer of the CN⁻ group from HypE to HypCD has first been demonstrated via *in vitro* ¹⁴C-labeling experiments (Blokesch et al. 2004b). Interestingly, the transfer was only possible when HypCD was purified under reducing conditions in the presence of DTT (Blokesch et al. 2004b; Blokesch and Böck 2006). These were the same conditions at which the ATPase activity of HypCD was highest. To investigate whether the ATPase activity is required for the CN⁻ ligand transfer, the transfer could be tested *in vitro* with purified HypCD, and HypE-CN in the absence or presence of ATP.

4.2.2. HypX catalyzes the aerobic CO ligand synthesis

Here we present *in vitro* evidence that HypX produces CO from *N*¹⁰-formyl-THF as the substrate. Formyl-CoA is formed as an intermediate. Based on our results, the HypX crystal structure (Muraki et al. 2019), and the similarities of the two HypX modules to *N*¹⁰-formyl-THF transferases and enoyl-CoA hydratases/isomerases of the crotonase superfamily, we propose a two-step reaction mechanism.

Discussion

The first step implies a transfer reaction analogous to that occurring in the N-terminal domain of N^{10} -formyl-THF dehydrogenases (FDH) (Lin et al. 2015; Chumanevich et al. 2004). Full-length FDH converts N^{10} -formyl-THF into THF and CO_2 in the presence of 4'-phosphopantetheine (4'-PP). The CoA precursor 4'-PP is proposed to shuttle the formyl group of N^{10} -formyl-THF between the two catalytic domains of FDH (Donato et al. 2007; Chang et al. 2010; Krupenko 2009). The isolated N-terminal FDH domain requires β -mercaptoethanol for activity and catalyzes the conversion of N^{10} -formyl-THF into THF and formate (Schirch et al. 1994). Based on the crystal structures of the N-terminal domain of zebrafish FDH in complex with the substrate analogue 10-formyl-5,8-dideazafolate as well as with the reaction products THF and formate, a catalytic mechanism has been proposed where the formyl group of N^{10} -formyl-THF is temporarily transferred to the thiol group of β -mercaptoethanol. This transfer process involves conserved His and Asp residues (Lin et al. 2015), which are also present in the N-terminal HypX module (His74 and Asp109), and were found to be functionally important (Bürstel et al. 2016; Buhrke 2002; Muraki et al. 2019).

We propose a catalytic mechanism for HypX (**Figure 45**) where His74 positions the formyl group of N^{10} -formyl-THF by establishing a hydrogen bond between $\text{N}\delta$ of His74 and the formyl group oxygen, while Asp109 activates CoA for nucleophilic attack on the carbonyl C atom of the formyl group. This results in the formation of formyl-CoA and the concomitant release of THF (**Figure 45**, top).

Discussion

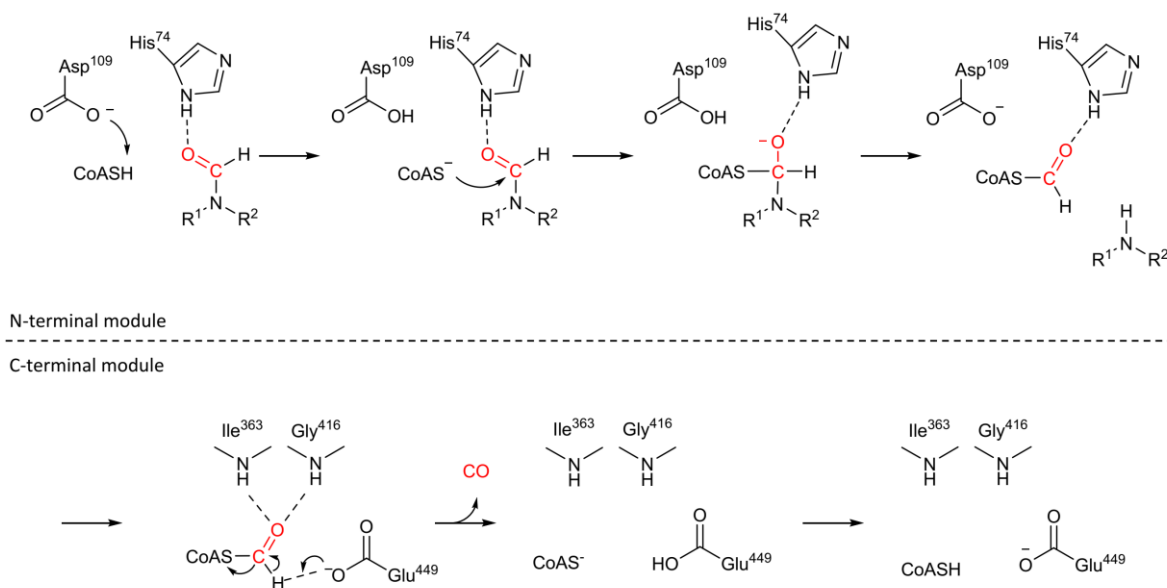


Figure 45. Proposed two-step reaction mechanism catalyzed by HypX. The N-terminal module catalyzes the transfer of the formyl group of N^{10} -formyl-THF to CoA, forming formyl-CoA. His74 positions the formyl group of N^{10} -formyl-THF by hydrogen bonding. Asp109 activates CoA for nucleophilic attack on the carbonyl C of the formyl group, resulting in the formation of formyl-CoA. Formyl-CoA is converted within the C-terminal module to CoA and CO. The backbone amides of the conserved residues Ile363 and Gly416 polarize the formyl group of formyl-CoA, enabling proton abstraction by Glu449 and leading to the formation of CO and CoAS⁻. Protonated Glu449 then reprotonates CoAS⁻, regenerating CoA.

In full-length FDH, the formylated 4'-PP moiety is supposed to swing between the two catalytic centers, thereby transferring the formyl group to the C-terminal dehydrogenase domain (Krupenko 2009). A similar flexibility has been observed for the pantetheine moiety of CoA (without formyl group), which was co-crystallized with *A. aeolicus* HypX (Muraki et al. 2019). Consequently, we propose a role for CoA in transferring the formyl group from the N-terminal module to the C-terminal module of HypX, where the second reaction step is taking place. There, formyl-CoA is converted into CO and free CoA.

The C-terminal module of HypX shares similarity with enzymes of the crotonase superfamily, which catalyze a wide range of reactions, but share common mechanistic features (Hamed et al. 2008). Two conserved backbone amides of the active site form an oxyanion hole, which polarizes the substrate carbonyl group of the CoA thioester. The corresponding oxyanion hole in HypX consists of the backbone amides of the residues Ile363 and Gly416 (Figure 45 bottom) (Bürstel et al. 2016). It presumably positions and polarizes the formyl-CoA-derived formyl group via hydrogen bonding. The polarization increases the acidity of the formyl group hydrogen. Many reactions of crotonase family members involve acid/base catalysis, which is usually facilitated by aspartate or glutamate residues located in the vicinity of the oxyanion

Discussion

hole (Hamed et al. 2008). Indeed, HypX possesses a conserved glutamate, Glu449, which, in its deprotonated form, would enable abstraction of the polarized formyl group hydrogen resulting in the formation of CO and CoA. This is supported by the crystal structure of *A. aeolicus* HypX, where the corresponding Glu426 is located close to the thiol group of CoA (Muraki et al. 2019). In agreement with the importance of Glu449 for the *in vivo* function of *R. eutropha* HypX (Bürstel et al. 2016), our *in vitro* results revealed that the E449Q exchange actually liquidated the CO-releasing activity of HypX. An analogous mechanism has been described for Δ^3 - Δ^2 -enoyl-CoA isomerases, where the carboxyl side group of a conserved glutamate acts as catalytic base abstracting a proton from the C2 carbon atom of the substrate 3-enoyl-CoA and, subsequently, donates the proton back to the C4 carbon atom to form the product 2-enoyl-CoA (Mursula et al. 2001).

To investigate whether the mechanism shown in **Figure 45** is reasonable, preliminary quantum chemical calculations (Grimme et al. 2011; Stephens et al. 1994; Neese 2012) were performed in cooperation with Giovanni Bistoni and Frank Neese from Max Planck Institut für Kohlenforschung in Mülheim an der Ruhr (Schulz et al. 2020). While the reactions proposed for the N-terminal HypX module were energetically reasonable, the first CO-releasing reaction in the C-terminal module was found to be strongly uphill. However, subsequent high-level calculations (Riplinger et al. 2016) incorporating an approximated entropy contribution to the reaction resulted in a significant decrease of the energetics of the two last intermediates with respect to the first one. These results indicate that the predicted reactions catalyzed by the C-terminal module are probably feasible from a thermodynamic point of view, provided that a significant entropic contribution is considered. In fact, such an entropic effect is rather likely because two products emerge from the reaction, one of which is gaseous.

HypX catalyzed CO formation from N^{10} -formyl-THF with a turnover rate of $k_{\text{cat}} = (1.85 \pm 0.07) \text{ h}^{-1}$, which is similar to that of HydG ($(4.10 \pm 0.04) \text{ h}^{-1}$), a radical-SAM-dependent tyrosine lyase responsible for CN^- and CO synthesis of [FeFe]-hydrogenase. The turnover rates of both maturases are rather low. In case of HydG, however, it has been shown that its activity increases in the presence of the two other maturases and apo-enzyme of [FeFe]-hydrogenase (Kuchenreuther et al. 2012). We can therefore speculate that the HypX activity raises in a complex with the HypCD scaffold.

HypX and HydG belong to the small and phylogenetically unrelated family of CO releasing enzymes (Xavier et al. 2018), which includes the acetyl-CoA synthase/CO dehydrogenase complex (Jeoung et al. 2014; Can et al. 2014), heme oxygenase (Kikuchi et al. 2005), several

Discussion

dioxygenases (Oka and Simpson 1971; Bauer et al. 1994; Wray and Abeles 1993), certain enigmatic plant and algal aldehyde decarbonylases (Marsh and Waugh 2013), as well as phosphomethylpyrimidine synthase (Chatterjee et al. 2010). In contrast to all other CO-releasing enzymes known so far, however, HypX represents the only catalyst that produces CO without the aid of transition metals. The overall reaction mechanism qualifies HypX as N^{10} -formyl-THF decarbonylase. The two catalytic centers, however, allow a more detailed description of the reaction. The N-terminal HypX module represents an N^{10} -formyl-THF:CoA formyltransferase, while the C-terminal module acts as formyl-CoA decarbonylase belonging to the subfamily of carbon-sulfur lyases.

It is worth to mention that the distribution of HypX is not restricted to prokaryotes synthesizing O_2 -tolerant [NiFe]-hydrogenases (Bürstel et al. 2016). According to a standard BLASTP search using *R. eutropha* HypX as the query (AAP85774.1) (Altschul et al. 1997), hundreds of HypX copies were identified in fungi including ascomycetes, basidiomycetes, rust fungi and smut fungi. Among them are pathogenic species such as *Ustilago maydis*, *Puccinia sorghi*, *Rhizoctonia solani*, and *Fusarium oxysporum*. It is conceivable that CO production is related to the pathogenicity of these fungi. Moreover, HypX with all its conserved amino acid residues proposed to be involved in catalysis is even encoded in the genomes of higher eukaryotes (Schulz et al. 2020). This includes the spreading earthmoss *Physcomitrella patens* – a model plant –, and the ubiquitous freshwater tardigrade *Hypsibius dujardini*, known for its ability to survive extreme conditions. In addition, there is a number of *hypX*-containing organisms thriving in sea water, such as, e.g., rotifers (*Brachionus plicatilis*), sea cucumber (*Apostichopus japonicus*), and lancelets (*Branchiostoma* spec.), the latter are considered the most primitive chordates. HypX seems to be abundant in genomes of corals (*Orbicella faveolata*, *Pocillopora damicornis*, *Dendronephthya gigantea*), which belong to the phylum Cnidaria. Interestingly, CO makes up a significant proportion (up to 20 %) of the total gas volume in the floats of the Portuguese man-of-war (*Physalia physalis*), whose genome has not been sequenced so far. Deep sea siphonophores can even contain 90% of CO gas in their float (Pickwell et al. 1964). It has been shown that the CO is produced from L-serine in the gas gland of these cnidarians, which is actually rich in folic acid derivatives (Hahn and Eugene Copeland 1966; Wittenberg 1960). Is HypX the responsible biocatalyst?

5. References

- Adamson, Hope; Robinson, Martin; Bond, Paul S.; Soboh, Basem; Gillow, Kathryn; Simonov, Alexandr N. et al. (2017a): Analysis of HypD disulfide redox chemistry via optimization of Fourier transformed ac voltammetric data. In *Anal Chem* 89 (3), pp. 1565–1573. DOI: 10.1021/acs.analchem.6b03589.
- Adamson, Hope; Robinson, Martin; Wright, John J.; Flanagan, Lindsey A.; Walton, Julia; Elton, Darrell et al. (2017b): Retuning the catalytic bias and overpotential of a [NiFe]-hydrogenase via a single amino acid exchange at the electron entry/exit site. In *J Am Chem Soc* 139 (31), pp. 10677–10686. DOI: 10.1021/jacs.7b03611.
- Albareda, Marta; Palacios, Jose-Manuel; Imperial, Juan; Pacios, Luis F. (2013): Computational study of the Fe(CN)₂CO cofactor and its binding to HypC protein. In *J Phys Chem B* 117 (43), pp. 13523–13533. DOI: 10.1021/jp407574n.
- Altschul, S. F.; Madden, T. L.; Schaffer, A. A.; Zhang, J.; Zhang, Z.; Miller, W.; Lipman, D. J. (1997): Gapped BLAST and PSI-BLAST: a new generation of protein database search programs. In *Nucleic Acids Res* 25 (17), pp. 3389–3402. DOI: 10.1093/nar/25.17.3389.
- Antonini, Eraldo; Brunori, Maurizio (1971): Hemoglobin and myoglobin in their reactions with ligands: Amsterdam : North-Holland. Available online at <http://lib.ugent.be/catalog/rug01:001650991>.
- Bagley, K. A.; Duin, E. C.; Roseboom, W.; Albracht, S. P.; Woodruff, W. H. (1995): Infrared-detectable groups sense changes in charge density on the nickel center in hydrogenase from *Chromatium vinosum*. In *Biochemistry* 34 (16), pp. 5527–5535. DOI: 10.1021/bi00016a026.
- Bagley, K. A.; van Garderen, C. J.; Chen, M.; Duin, E. C.; Albracht, S. P.; Woodruff, W. H. (1994): Infrared studies on the interaction of carbon monoxide with divalent nickel in hydrogenase from *Chromatium vinosum*. In *Biochemistry* 33 (31), pp. 9229–9236. DOI: 10.1021/bi00197a026.
- Bai, Liping; Fujishiro, Takashi; Huang, Gangfeng; Koch, Jürgen; Takabayashi, Atsushi; Yokono, Makio et al. (2017): Towards artificial methanogenesis: biosynthesis of the [Fe]-hydrogenase cofactor and characterization of the semi-synthetic hydrogenase. In *Faraday Discuss* 198, pp. 37–58. DOI: 10.1039/c6fd00209a.
- Bauer, Iris; Beyer, Andr  ; Tshisuaka, Barbara; Fetzner, Susanne; Lingens, Franz (1994): A novel type of oxygenolytic ring cleavage: 2,4-oxygenation and decarbonylation of 1H-3-hydroxy-4-oxoquinoline and 1H-3-hydroxy-4-oxoquinoline. In *FEMS Microbiol Lett* 117 (3), pp. 299–304. DOI: 10.1111/j.1574-6968.1994.tb06783.x.
- Begg, Yvonne A.; Whyte, Janette N.; Haddock, Bruce A. (1977): The identification of mutants of *Escherichia coli* deficient in formate dehydrogenase and nitrate reductase activities using dye indicator plates. In *FEMS Microbiol Lett* 2 (1), pp. 47–50. DOI: 10.1111/j.1574-6968.1977.tb00905.x.
- Benvenuti, Manuela; Mangani, Stefano (2007): Crystallization of soluble proteins in vapor diffusion for x-ray crystallography. In *Nat Protoc* 2 (7), pp. 1633–1651. DOI: 10.1038/nprot.2007.198.
- Berggren, Gustav; Adamska, A.; Lambertz, C.; Simmons, T. R.; Esselborn, J.; Atta, M. et al. (2013): Biomimetic assembly and activation of [FeFe]-hydrogenases. In *Nature* 499 (7456), pp. 66–69. DOI: 10.1038/nature12239.
- Bergmeyer, H. U. (1975): Neue Werte f  r die molaren Extinktions-Koeffizienten von NADH und NADPH zum Gebrauch im Routine-Laboratorium. In *Zeitschrift f  r klinische Chemie und klinische Biochemie* 13 (11), pp. 507–508.

References

- Binder, Ursula; Maier, Thomas; Böck, A. (1996): Nickel incorporation into hydrogenase 3 from *Escherichia coli* requires the precursor form of the large subunit. In *Arch Microbiol* 165 (1), pp. 69–72. DOI: 10.1007/s002030050299.
- Blokesch, M.; Magalon, A.; Böck, A. (2001a): Interplay between the specific chaperone-like proteins HybG and HypC in maturation of hydrogenases 1, 2, and 3 from *Escherichia coli*. In *J Bacteriol* 183 (9), pp. 2817–2822. DOI: 10.1128/JB.183.9.2817-2822.2001.
- Blokesch, Melanie (2004a): [NiFe]-Hydrogenasen von *Escherichia coli*: Funktionen der am Metalleinbau beteiligten Proteine. PhD thesis. Ludwig-Maximilians-Universität, München. Fakultät für Biologie.
- Blokesch, Melanie; Albracht, Simon P. J.; Matzanke, Berthold F.; Drapal, Nikola M.; Jacobi, Alexander; Böck, August (2004b): The complex between hydrogenase-maturation proteins HypC and HypD is an intermediate in the supply of cyanide to the active site iron of NiFe-hydrogenases. In *J Mol Biol* 344 (1), pp. 155–167. DOI: 10.1016/j.jmb.2004.09.040.
- Blokesch, Melanie; Böck, August (2002): Maturation of [NiFe]-hydrogenases in *Escherichia coli*: the HypC cycle. In *J Mol Biol* 324 (2), pp. 287–296. DOI: 10.1016/S0022-2836(02)01070-7.
- Blokesch, Melanie; Böck, August (2006): Properties of the [NiFe]-hydrogenase maturation protein HypD. In *FEBS Lett* 580 (17), pp. 4065–4068. DOI: 10.1016/j.febslet.2006.06.045.
- Blokesch, Melanie; Magalon, Axel; Böck, August (2001b): Interplay between the specific chaperone-like proteins HybG and HypC in maturation of hydrogenases 1, 2, and 3 from *Escherichia coli*. In *J Bacteriol* 183 (9), pp. 2817–2822. DOI: 10.1128/JB.183.9.2817-2822.2001.
- Blokesch, Melanie; Paschos, Athanasios; Bauer, Anette; Reissmann, Stefanie; Drapal, Nikola; Bock, August (2004c): Analysis of the transcarbamoylation-dehydration reaction catalyzed by the hydrogenase maturation proteins HypF and HypE. In *Eur J Biochem* 271 (16), pp. 3428–3436. DOI: 10.1111/j.1432-1033.2004.04280.x.
- Böck, August; King, Paul W.; Blokesch, Melanie; Posewitz, Matthew C. (2006): Maturation of hydrogenases. In *Adv Microb Physiol* 51, pp. 1–71. DOI: 10.1016/S0065-2911(06)51001-X.
- Bruschi, Maurizio; Tiberti, Matteo; Guerra, Alessandro; Gioia, Luca de (2014): Disclosure of key stereoelectronic factors for efficient H₂ binding and cleavage in the active site of [NiFe]-hydrogenases. In *J Am Chem Soc* 136 (5), pp. 1803–1814. DOI: 10.1021/ja408511y.
- Buhrke, Thorsten (2002): Der H₂-Sensor von *Ralstonia eutropha*: Struktur-Funktions-Beziehungen einer neuartigen [NiFe]-Hydrogenase. PhD thesis. Humboldt-Universität zu Berlin, Berlin. Institut für Biologie.
- Buhrke, Thorsten; Friedrich, Bärbel (1998): *hoxX (hypX)* is a functional member of the *Alcaligenes eutrophus hyp* gene cluster. In *Arch Microbiol* 170 (6), pp. 460–463. DOI: 10.1007/s002030050667.
- Bull, Henry B.; Breese, Keith (1973): Thermal stability of proteins. In *Arch Biochem Biophys* 158 (2), pp. 681–686. DOI: 10.1016/0003-9861(73)90561-4.
- Bürstel, Ingmar; Hummel, Philipp; Siebert, Elisabeth; Wisitruangsakul, Nattawadee; Zebger, Ingo; Friedrich, Bärbel; Lenz, Oliver (2011): Probing the origin of the metabolic precursor of the CO ligand in the catalytic center of [NiFe] hydrogenase. In *J Biol Chem* 286 (52), pp. 44937–44944. DOI: 10.1074/jbc.M111.309351.
- Bürstel, Ingmar; Siebert, Elisabeth; Frielingsdorf, Stefan; Zebger, Ingo; Friedrich, Bärbel; Lenz, Oliver (2016): CO synthesized from the central one-carbon pool as source for the iron carbonyl in O₂-

References

- tolerant [NiFe]-hydrogenase. In *Proc Natl Acad Sci USA* 113 (51), pp. 14722–14726. DOI: 10.1073/pnas.1614656113.
- Bürstel, Ingmar; Siebert, Elisabeth; Winter, Gordon; Hummel, Philipp; Zebger, Ingo; Friedrich, Bärbel; Lenz, Oliver (2012): A universal scaffold for synthesis of the Fe(CN)₂(CO) moiety of [NiFe] hydrogenase. In *J Biol Chem* 287 (46), pp. 38845–38853. DOI: 10.1074/jbc.M112.376947.
- Cammack, Richard; Frey, M.; Robson, R. (2001): *Hydrogen as a Fuel. Learning from Nature*. New York: Taylor & Francis inc.
- Can, Mehmet; Armstrong, Fraser A.; Ragsdale, Stephen W. (2014): Structure, function, and mechanism of the nickel metalloenzymes, CO dehydrogenase, and acetyl-CoA synthase. In *Chem Rev* 114 (8), pp. 4149–4174. DOI: 10.1021/cr400461p.
- Caserta, Giorgio; Lorent, Christian; Ciaccafava, Alexandre; Keck, Matthias; Breglia, Raffaella; Greco, Claudio et al. (2020): The large subunit of the regulatory [NiFe]-hydrogenase from *Ralstonia eutropha* – a minimal hydrogenase? In *Chem Sci* 11 (21), pp. 5453–5465. DOI: 10.1039/D0SC01369B.
- Chang, Wen-Ni; Lin, Hung-Chang; Fu, Tzu-Fun (2010): Zebrafish 10-formyltetrahydrofolate dehydrogenase is similar to its mammalian isozymes for its structural and catalytic properties. In *Protein Expr Purif* 72 (2), pp. 217–222. DOI: 10.1016/j.pep.2010.04.003.
- Chatterjee, Abhishek; Hazra, Amrita B.; Abdelwahed, Sameh; Hilmey, David G.; Begley, Tadhg P. (2010): A "radical dance" in thiamin biosynthesis: mechanistic analysis of the bacterial hydroxymethylpyrimidine phosphate synthase. In *Angew Chem Int Ed* 49 (46), pp. 8653–8656. DOI: 10.1002/anie.201003419.
- Chumanevich, Alexander A.; Krupenko, Sergey A.; Davies, Christopher (2004): The crystal structure of the hydrolase domain of 10-formyltetrahydrofolate dehydrogenase: mechanism of hydrolysis and its interplay with the dehydrogenase domain. In *J Biol Chem* 279 (14), pp. 14355–14364. DOI: 10.1074/jbc.M313934200.
- Ciaccafava, Alexandre; Tombolelli, Daria; Domnik, Lilith; Fessler, Jochen; Jeoung, Jae-Hun; Dobbek, Holger et al. (2016): When the inhibitor tells more than the substrate: the cyanide-bound state of a carbon monoxide dehydrogenase. In *Chem Sci* 7 (5), pp. 3162–3171. DOI: 10.1039/c5sc04554a.
- Constant, Philippe; Chowdhury, Soumitra Paul; Hesse, Laura; Pratscher, Jennifer; Conrad, Ralf (2011): Genome data mining and soil survey for the novel group 5 [NiFe]-hydrogenase to explore the diversity and ecological importance of presumptive high-affinity H₂-oxidizing bacteria. In *Applied and environmental microbiology* 77 (17), pp. 6027–6035. DOI: 10.1128/AEM.00673-11.
- Dementin, Sébastien; Burlat, Bénédicte; Lacey, Antonio L. De; Pardo, Alejandro; Adryanczyk-Perrier, Géraldine; Guigliarelli, Bruno et al. (2004): A glutamate is the essential proton transfer gate during the catalytic cycle of the [NiFe] hydrogenase. In *J Biol Chem* 279 (11), pp. 10508–10513. DOI: 10.1074/jbc.M312716200.
- Donato, Henry; Krupenko, Natalia I.; Tsybovsky, Yaroslav; Krupenko, Sergey A. (2007): 10-formyltetrahydrofolate dehydrogenase requires a 4'-phosphopantetheine prosthetic group for catalysis. In *J Biol Chem* 282 (47), pp. 34159–34166. DOI: 10.1074/jbc.M707627200.
- Drapal, N.; Böck, A. (1998): Interaction of the hydrogenase accessory protein HypC with HycE, the large subunit of *Escherichia coli* hydrogenase 3 during enzyme maturation. In *Biochemistry* 37 (9), pp. 2941–2948. DOI: 10.1021/bi9720078.

References

- Eadsforth, Thomas C.; Gardiner, Mary; Maluf, Fernando V.; McElroy, Stuart; James, Daniel; Frearson, Julie et al. (2012): Assessment of *Pseudomonas aeruginosa* N⁵,N¹⁰-Methylenetetrahydrofolate Dehydrogenase - Cyclohydrolase as a Potential Antibacterial Drug Target. In *PLoS One* 7 (4), e35973. DOI: 10.1371/journal.pone.0035973.
- Esselborn, Julian; Lambertz, Camilla; Adamska-Venkates, Agnieszka; Simmons, Trevor; Berggren, Gustav; Noth, Jens et al. (2013): Spontaneous activation of [FeFe]-hydrogenases by an inorganic [2Fe] active site mimic. In *Nat Chem Biol* 9 (10), pp. 607–609. DOI: 10.1038/nchembio.1311.
- Evans, Rhiannon M.; Ash, Philip A.; Beaton, Stephen E.; Brooke, Emily J.; Vincent, Kylie A.; Carr, Stephen B.; Armstrong, Fraser A. (2018): Mechanistic exploitation of a self-repairing, blocked proton transfer pathway in an O₂-tolerant [NiFe]-hydrogenase. In *J Am Chem Soc* 140 (32), pp. 10208–10220. DOI: 10.1021/jacs.8b04798.
- Evans, Rhiannon M.; Brooke, Emily J.; Wehlin, Sara A. M.; Nomerotskaia, Elena; Sargent, Frank; Carr, Stephen B. et al. (2016): Mechanism of hydrogen activation by [NiFe] hydrogenases. In *Nat Chem Biol* 12 (1), pp. 46–50. DOI: 10.1038/nchembio.1976.
- Fontecilla-Camps, Juan C.; Amara, Patricia; Cavazza, Christine; Nicolet, Yvain; Volbeda, Anne (2009): Structure-function relationships of anaerobic gas-processing metalloenzymes. In *Nature* 460 (7257), pp. 814–822. DOI: 10.1038/nature08299.
- Forzi, Lucia; Hellwig, Petra; Thauer, Rudolf K.; Sawers, R. Gary (2007): The CO and CN⁻ ligands to the active site Fe in [NiFe]-hydrogenase of *Escherichia coli* have different metabolic origins. In *FEBS Lett* 581 (17), pp. 3317–3321. DOI: 10.1016/j.febslet.2007.06.028.
- Friedrich, C. G. (1982): Depression of hydrogenase during limitation of electron donors and derepression of ribulosebisphosphate carboxylase during carbon limitation of *Alcaligenes eutrophus*. In *J Bacteriol* 149 (1), pp. 203–210.
- Friedrich, C. G.; Friedrich, B.; Bowien, B. (1981): Formation of Enzymes of Autotrophic Metabolism During Heterotrophic Growth of *Alcaligenes eutrophus*. In *Microbiology* 122 (1), pp. 69–78. DOI: 10.1099/00221287-122-1-69.
- Friedrich, C. G.; Friedrich, Bärbel (1983): Regulation of Hydrogenase Formation Is Temperature Sensitive and Plasmid Coded in *Alcaligenes eutrophus*. In *J Bacteriol* 153 (1), pp. 176–181.
- Fritsch, Johannes; Scheerer, P.; Frielingsdorf, Stefan; Kroschinsky, S.; Friedrich, Bärbel; Lenz, O.; Spahn, C. M. (2011): The crystal structure of an oxygen-tolerant hydrogenase uncovers a novel iron-sulphur centre. In *Nature* 479 (7372), pp. 249–252. DOI: 10.1038/nature10505.
- Galván, Ignacio Fdez.; Volbeda, Anne; Fontecilla-Camps, Juan C.; Field, Martin J. (2008): A QM/MM study of proton transport pathways in a [NiFe] hydrogenase. In *Proteins: Struct, Funct, Bioinf* 73 (1), pp. 195–203. DOI: 10.1002/prot.22045.
- Gebler, Antje; Burgdorf, Tanja; Lacey, Antonio L. De; Rüdiger, Olaf; Martinez-Arias, Arturo; Lenz, Oliver; Friedrich, Bärbel (2007): Impact of alterations near the [NiFe] active site on the function of the H₂ sensor from *Ralstonia eutropha*. In *FEBS J* 274 (1), pp. 74–85. DOI: 10.1111/j.1742-4658.2006.05565.x.
- Germer, Frauke; Zebger, Ingo; Saggiu, Miguel; Lendzian, Friedhelm; Schulz, Rüdiger; Appel, Jens (2009): Overexpression, isolation, and spectroscopic characterization of the bidirectional [NiFe] hydrogenase from *Synechocystis* sp. PCC 6803. In *J Biol Chem* 284 (52), pp. 36462–36472. DOI: 10.1074/jbc.M109.028795.

References

- Gibson, Daniel G.; Young, Lei; Chuang, Ray-Yuan; Venter, J. Craig; Hutchison, Clyde A.; Smith, Hamilton O. (2009): Enzymatic assembly of DNA molecules up to several hundred kilobases. In *Nat Methods* 6 (5), pp. 343–345. DOI: 10.1038/nmeth.1318.
- Goris, T.; Wait, Annemarie F.; Saggi, M.; Fritsch, Johannes; Heidary, N.; Stein, M. et al. (2011): A unique iron-sulfur cluster is crucial for oxygen tolerance of a [NiFe]-hydrogenase. In *Nat Chem Biol* 7 (5), pp. 310–318. DOI: 10.1038/nchembio.555.
- Goto, Eiji; Kodama, Tohru; Minoda, Yasuji (1978): Growth and taxonomy of thermophilic hydrogen bacteria. In *Agric Biol Chem* 42 (7), pp. 1305–1308. DOI: 10.1080/00021369.1978.10863157.
- Greene, Brandon L.; Vansuch, Gregory E.; Wu, Chang-Hao; Adams, Michael W. W.; Dyer, R. Brian (2016): Glutamate gated proton-coupled electron transfer activity of a [NiFe]-hydrogenase. In *J Am Chem Soc* 138 (39), pp. 13013–13021. DOI: 10.1021/jacs.6b07789.
- Greene, Brandon L.; Wu, Chang-Hao; McTernan, Patrick M.; Adams, Michael W. W.; Dyer, R. Brian (2015): Proton-coupled electron transfer dynamics in the catalytic mechanism of a [NiFe]-hydrogenase. In *J Am Chem Soc* 137 (13), pp. 4558–4566. DOI: 10.1021/jacs.5b01791.
- Greening, C.; Biswas, A.; Carere, C. R.; Jackson, C. J.; Taylor, M. C.; Stott, M. B. et al. (2015): Genomic and metagenomic surveys of hydrogenase distribution indicate H₂ is a widely utilised energy source for microbial growth and survival. In *ISME J*. DOI: 10.1038/ismej.2015.153.
- Grimme, Stefan; Ehrlich, Stephan; Goerigk, Lars (2011): Effect of the damping function in dispersion corrected density functional theory. In *J Comput Chem* 32 (7), pp. 1456–1465. DOI: 10.1002/jcc.21759.
- Guiral M.; Tron, P.; Valérie Belle; Aubert C.; Léger, C.; Guigliarelli, B.; Giudici-Ortoni, M. T. (2006): Hyperthermostable and oxygen resistant hydrogenases from a hyperthermophilic bacterium *Aquifex aeolicus*: Physicochemical properties. In *Int J Hydrogen Energ* 31 (11), pp. 1424–1431. DOI: 10.1016/j.ijhydene.2006.06.007.
- Hahn, William E.; Eugene Copeland, D. (1966): Carbon monoxide concentrations and the effect of aminopterin on its production in the gas bladder of *Physalia Physalis*. In *CBP* 18 (1), pp. 201–207. DOI: 10.1016/0010-406X(66)90344-6.
- Hamed, R. B.; Batchelar, E. T.; Clifton, I. J.; Schofield, C. J. (2008): Mechanisms and structures of crotonase superfamily enzymes - How nature controls enolate and oxyanion reactivity. In *Cell Mol Life Sci* 65 (16), pp. 2507–2527. DOI: 10.1007/s00018-008-8082-6.
- Happe, R. P.; Roseboom, W.; Pierik, A. J.; Albracht, S. P.; Bagley, K. A. (1997): Biological activation of hydrogen. In *Nature* 385 (6612), p. 126. DOI: 10.1038/385126a0.
- Happe, Randolph P.; Roseboom, Winfried; Egert, Gabriele; Friedrich, Cornelius G.; Massanz, Christian; Friedrich, Bärbel; Albracht, Simon P.J. (2000): Unusual FTIR and EPR properties of the H₂-activating site of the cytoplasmic NAD-reducing hydrogenase from *Ralstonia eutropha*. In *FEBS Lett* 466 (2-3), pp. 259–263. DOI: 10.1016/S0014-5793(99)01799-8.
- Hartmann, Sven; Frielingsdorf, Stefan; Ciaccafava, Alexandre; Lorent, Christian; Fritsch, Johannes; Siebert, Elisabeth et al. (2018): O₂-tolerant H₂ activation by an isolated large subunit of a [NiFe] hydrogenase. In *Biochemistry* 57 (36), pp. 5339–5349. DOI: 10.1021/acs.biochem.8b00760.
- Hayashi, N. R.; Ishida, T.; Yokota, A.; Kodama, T.; Igarashi, Y. (1999): *Hydrogenophilus thermoluteolus* gen. nov., sp. nov., a thermophilic, facultatively chemolithoautotrophic, hydrogen-oxidizing bacterium. In *Int J Syst Evol Micr* 49 Pt 2, pp. 783–786. DOI: 10.1099/00207713-49-2-783.

References

- Holcomb, Joshua; Spellmon, Nicholas; Zhang, Yingxue; Doughan, Maysaa; Li, Chunying; Yang, Zhe (2017): Protein crystallization: Eluding the bottleneck of X-ray crystallography. In *AIMS Biophys* 4 (4), pp. 557–575. DOI: 10.3934/biophy.2017.4.557.
- Horch, M.; Hildebrandt, P.; Zebger, I. (2015a): Concepts in bio-molecular spectroscopy: vibrational case studies on metalloenzymes. In *Phys Chem Chem Phys* 17 (28), pp. 18222–18237. DOI: 10.1039/c5cp02447a.
- Horch, M.; Lauterbach, L.; Lenz, O.; Hildebrandt, P.; Zebger, I. (2012): NAD(H)-coupled hydrogen cycling – structure–function relationships of bidirectional [NiFe] hydrogenases. In *FEBS Lett* 586 (5), pp. 545–556. DOI: 10.1016/j.febslet.2011.10.010.
- Horch, M.; Lauterbach, Lars; Saggu, M.; Hildebrandt, P.; Lenzian, F.; Bittl, R. et al. (2010): Probing the active site of an O₂-tolerant NAD⁺-reducing [NiFe]-hydrogenase from *Ralstonia eutropha* H16 by in situ EPR and FTIR spectroscopy. In *Angew Chem Int Ed* 49 (43), pp. 8026–8029. DOI: 10.1002/anie.201002197.
- Horch, Marius; Lauterbach, Lars; Mroginski, Maria Andrea; Hildebrandt, Peter; Lenz, Oliver; Zebger, Ingo (2015b): Reversible active site sulfoxxygenation can explain the oxygen tolerance of a NAD⁺-reducing [NiFe] hydrogenase and its unusual infrared spectroscopic properties. In *J Am Chem Soc* 137 (7), pp. 2555–2564. DOI: 10.1021/ja511154y.
- Horch, Marius; Schoknecht, Janna; Mroginski, Maria Andrea; Lenz, Oliver; Hildebrandt, Peter; Zebger, Ingo (2014): Resonance Raman spectroscopy on [NiFe] hydrogenase provides structural insights into catalytic intermediates and reactions. In *J Am Chem Soc* 136 (28), pp. 9870–9873. DOI: 10.1021/ja505119q.
- Hube, Michaela; Blokesch, Melanie; Böck, August (2002): Network of hydrogenase maturation in *Escherichia coli*: role of accessory proteins HypA and HybF. In *J Bacteriol* 184 (14), pp. 3879–3885. DOI: 10.1128/JB.184.14.3879-3885.2002.
- Jeoung, Jae-Hun; Fessler, Jochen; Goetzl, Sebastian; Dobbek, Holger (2014): Carbon monoxide. Toxic gas and fuel for anaerobes and aerobes: carbon monoxide dehydrogenases. In *Met Ions Life Sci* 14, pp. 37–69. DOI: 10.1007/978-94-017-9269-1_3.
- Jones, Anne K.; Lenz, Oliver; Strack, Angelika; Buhrke, Thorsten; Friedrich, Bärbel (2004): NiFe hydrogenase active site biosynthesis: identification of Hyp protein complexes in *Ralstonia eutropha*. In *Biochemistry* 43 (42), pp. 13467–13477. DOI: 10.1021/bi048837k.
- Kalms, Jacqueline; Schmidt, Andrea; Frielingsdorf, Stefan; Utesch, Tillmann; Gotthard, Guillaume; Stetten, David von et al. (2018): Tracking the route of molecular oxygen in O₂-tolerant membrane-bound [NiFe] hydrogenase. In *Proc Natl Acad Sci USA* 115 (10), E2229–E2237. DOI: 10.1073/pnas.1712267115.
- Kalms, Jacqueline; Schmidt, Andrea; Frielingsdorf, Stefan; van der Linden, Peter; Stetten, David von; Lenz, Oliver et al. (2016): Krypton derivatization of an O₂-tolerant membrane-bound [NiFe] hydrogenase reveals a hydrophobic tunnel network for gas transport. In *Angew Chem Int Ed* 55 (18), pp. 5586–5590. DOI: 10.1002/anie.201508976.
- Khorasani-Motlagh, Mozghan; Noroozifar, Meissam; Kerman, Kagan; Zamble, Deborah B. (2019): Complex formation between the *Escherichia coli* [NiFe]-hydrogenase nickel maturation factors. In *BioMetals* 32 (3), pp. 521–532. DOI: 10.1007/s10534-019-00173-9.
- Kikuchi, Goro; Yoshida, Tadashi; Noguchi, Masato (2005): Heme oxygenase and heme degradation. In *Biochem Biophys Res Commun* 338 (1), pp. 558–567. DOI: 10.1016/j.bbrc.2005.08.020.

References

- Kleihues, L.; Lenz, O.; Bernhard, M.; Buhrke, T.; Friedrich, Bärbel (2000): The H₂ sensor of *Ralstonia eutropha* is a member of the subclass of regulatory [NiFe] hydrogenases. In *J Bacteriol* 182 (10), pp. 2716–2724.
- Krupenko, Sergey A. (2009): FDH: An aldehyde dehydrogenase fusion enzyme in folate metabolism. In *Chem Biol Interact* 178 (1-3), pp. 84–93. DOI: 10.1016/j.cbi.2008.09.007.
- Kubas, G. J. (2007): Fundamentals of H₂ binding and reactivity on transition metals underlying hydrogenase function and H₂ production and storage. In *Chem Rev* 107 (10), pp. 4152–4205. DOI: 10.1021/cr050197j.
- Kuchenreuther, Jon M.; Britt, R. David; Swartz, James R. (2012): New insights into [FeFe] hydrogenase activation and maturase function. In *PloS One* 7 (9), e45850. DOI: 10.1371/journal.pone.0045850.
- Kuchenreuther, Jon M.; Myers, William K.; Stich, Troy A.; George, Simon J.; Nejatyjahromy, Yaser; Swartz, James R.; Britt, R. David (2013): A radical intermediate in tyrosine scission to the CO and CN⁻ ligands of FeFe hydrogenase. In *Science* 342 (6157), pp. 472–475. DOI: 10.1126/science.1241859.
- Kuila, Debasish; Schoonover, Jon R.; Dyer, R. Brian; Batic, Christopher J.; Ballou, David P.; Fee, James A.; Woodruff, William H. (1992): Resonance Raman studies of Rieske-type proteins. In *BBA - Bioenerg* 1140 (2), pp. 175–183. DOI: 10.1016/0005-2728(92)90007-O.
- Lacasse, Michael J.; Zamble, Deborah B. (2016): [NiFe]-Hydrogenase Maturation. In *Biochemistry* 55 (12), pp. 1689–1701. DOI: 10.1021/acs.biochem.5b01328.
- Laurinavichene, T. V.; Tsygankov, A. A. (2001): H₂ consumption by *Escherichia coli* coupled via hydrogenase 1 or hydrogenase 2 to different terminal electron acceptors. In *FEMS Microbiol Lett* 202 (1), pp. 121–124. DOI: 10.1111/j.1574-6968.2001.tb10790.x.
- Lauterbach, Lars; Lenz, Oliver; Vincent, Kylie A. (2013): H₂-driven cofactor regeneration with NAD(P)⁺-reducing hydrogenases. In *FEBS J* 280 (13), pp. 3058–3068. DOI: 10.1111/febs.12245.
- Lenz, Oliver; Lauterbach, Lars; Frielingsdorf, Stefan; Friedrich, Bärbel (2015): Oxygen-tolerant hydrogenases and their biotechnological potential. In Matthias Rögner (Ed.): *Biohydrogen*. Berlin, Boston: Walter de Gruyter GmbH & Co. KG, pp. 61–88.
- Li, Zilong; Ohki, Yasuhiro; Tatsumi, Kazuyuki (2005): Dithiolato-bridged dinuclear iron-nickel complexes [Fe(CO)₂(CN)₂(μ-SCH₂CH₂CH₂S)Ni(S₂CNR₂)]⁻ modeling the active site of [NiFe] hydrogenase. In *J Am Chem Soc* 127 (25), pp. 8950–8951. DOI: 10.1021/ja051590.
- Lin, Chien-Chih; Chuankhayan, Phimonphan; Chang, Wen-Ni; Kao, Tseng-Ting; Guan, Hong-Hsiang; Fun, Hoong-Kun et al. (2015): Structures of the hydrolase domain of zebrafish 10-formyltetrahydrofolate dehydrogenase and its complexes reveal a complete set of key residues for hydrolysis and product inhibition. In *Acta Crystallogr D* 71 (Pt 4), pp. 1006–1021. DOI: 10.1107/S1399004715002928.
- Lubitz, Wolfgang; Ogata, Hideaki; Rüdiger, Olaf; Reijerse, Edward (2014): Hydrogenases. In *Chem Rev* 114 (8), pp. 4081–4148. DOI: 10.1021/cr4005814.
- Ludwig, M.; Schubert, T.; Zebger, Ingo; Wisitruangsakul, N.; Saggi, M.; Strack, A. et al. (2009): Concerted action of two novel auxiliary proteins in assembly of the active site in a membrane-bound [NiFe] hydrogenase. In *J Biol Chem* 284 (4), pp. 2159–2168.

References

- Lukey, Michael J.; Parkin, Alison; Roessler, Maxie M.; Murphy, Bonnie J.; Harmer, Jeffrey; Palmer, Tracy et al. (2010): How *Escherichia coli* is equipped to oxidize hydrogen under different redox conditions. In *J Biol Chem* 285 (6), pp. 3928–3938. DOI: 10.1074/jbc.M109.067751.
- Magalon, Axel; Böck, August (2000): Analysis of the HypC-HycE complex, a key intermediate in the assembly of the metal center of the *Escherichia coli* hydrogenase 3. In *J. Biol. Chem.* 275 (28), pp. 21114–21120. DOI: 10.1074/jbc.M000987200.
- Marques, Marta C.; Coelho, Ricardo; Lacey, Antonio L. De; Pereira, Ines A. C.; Matias, Pedro M. (2010): The three-dimensional structure of [NiFeSe] hydrogenase from *Desulfovibrio vulgaris* Hildenborough: a hydrogenase without a bridging ligand in the active site in its oxidised, "as-isolated" state. In *J Mol Biol* 396 (4), pp. 893–907. DOI: 10.1016/j.jmb.2009.12.013.
- Marques, Marta C.; Coelho, Ricardo; Pereira, Inês A.C.; Matias, Pedro M. (2013): Redox state-dependent changes in the crystal structure of [NiFeSe] hydrogenase from *Desulfovibrio vulgaris* Hildenborough. In *Int J Hydrogen Energ* 38 (21), pp. 8664–8682. DOI: 10.1016/j.ijhydene.2013.04.132.
- Marsh, E. Neil G.; Waugh, Matthew W. (2013): Aldehyde decarboxylases: enigmatic enzymes of hydrocarbon biosynthesis. In *ACS Catal* 3 (11), pp. 2515–2521. DOI: 10.1021/cs400637t.
- Marx, Christopher J.; Lidstrom, Mary E. (2001): Development of improved versatile broad-host-range vectors for use in methylotrophs and other Gram-negative bacteria. In *Microbiology* 147 (8), pp. 2065–2075. DOI: 10.1099/00221287-147-8-2065.
- Montet, Y.; Amara, P.; Volbeda, A.; Vernede, X.; Hatchikian, E. C.; Field, M. J. et al. (1997): Gas access to the active site of Ni-Fe hydrogenases probed by X-ray crystallography and molecular dynamics. In *Nat Struct Biol* 4 (7), pp. 523–526. DOI: 10.1038/nsb0797-523.
- Muraki, Norifumi; Ishii, Kentaro; Uchiyama, Susumu; Itoh, Satoru G.; Okumura, Hisashi; Aono, Shigetoshi (2019): Structural characterization of HypX responsible for CO biosynthesis in the maturation of NiFe-hydrogenase. In *Commun Biol* 2 (1), pp. 1–12. DOI: 10.1038/s42003-019-0631-z.
- Mursula, A. M.; van Aalten, D. M.; Hiltunen, J. K.; Wierenga, R. K. (2001): The crystal structure of Δ^3 - Δ^2 -enoyl-CoA isomerase. In *J Mol Biol* 309 (4), pp. 845–853. DOI: 10.1006/jmbi.2001.4671.
- Nakamura, Kanji; Ishida, Hiroaki; Iizumi, Taro (2000): Constitutive trichloroethylene degradation led by *tac* promoter chromosomally integrated upstream of phenol hydroxylase genes of *Ralstonia* sp. KN1 and its nucleotide sequence analysis. In *J Biosci Bioeng* 89 (1), pp. 47–54. DOI: 10.1016/S1389-1723(00)88049-4.
- Neese, Frank (2012): The ORCA program system. In *WIREs Comput Mol Sci* 2 (1), pp. 73–78. DOI: 10.1002/wcms.81.
- Nutschan, Kerstin; Golbik, Ralph P.; Sawers, R. Gary (2019): The iron-sulfur-containing HypC-HypD scaffold complex of the [NiFe]-hydrogenase maturation machinery is an ATPase. In *FEBS Open Bio* 9 (12), pp. 2072–2079. DOI: 10.1002/2211-5463.12743.
- Ogata, Hideaki; Krämer, Tobias; Wang, Hongxin; Schilter, David; Pelmeshnikov, Vladimir; van Gastel, Maurice et al. (2015a): Hydride bridge in [NiFe]-hydrogenase observed by nuclear resonance vibrational spectroscopy. In *Nat Commun* 6 (1), pp. 1–8. DOI: 10.1038/ncomms8890.
- Ogata, Hideaki; Nishikawa, Koji; Lubitz, Wolfgang (2015b): Hydrogens detected by subatomic resolution protein crystallography in a [NiFe] hydrogenase. In *Nature* 520 (7548), pp. 571–574. DOI: 10.1038/nature14110.

References

- Oka, T.; Simpson, F. J. (1971): Quercetinase, a dioxygenase containing copper. In *Biochem Biophys Res Commun* 43 (1), pp. 1–5. DOI: 10.1016/S0006-291X(71)80076-1.
- Pandelia, Maria Eirini; Fourmond, Vincent; Tron-Infossi, Pascale; Lojou, E.; Bertrand, Patrick; Léger, C. et al. (2010): Membrane-bound hydrogenase I from the hyperthermophilic bacterium *Aquifex aeolicus*: enzyme activation, redox intermediates and oxygen tolerance. In *J Am Chem Soc* 132 (20), pp. 6991–7004. DOI: 10.1021/ja910838d.
- Pandelia, Maria-Eirini; Lubitz, Wolfgang; Nitschke, Wolfgang (2012): Evolution and diversification of Group 1 [NiFe] hydrogenases. Is there a phylogenetic marker for O₂-tolerance? In *BBA - Bioenerg* 1817 (9), pp. 1565–1575. DOI: 10.1016/j.bbabi.2012.04.012.
- Paschos, Athanasios (2002a): Biosynthese des Metallzentrums von [NiFe]-Hydrogenasen aus *E. coli*: Analyse zweier Reifungsenzyme. PhD Thesis. Ludwig-Maximilians-Universität, München.
- Paschos, Athanasios; Bauer, Anette; Zimmermann, Anja; Zehelein, Eva; Böck, August (2002b): HypF, a carbamoyl phosphate-converting enzyme involved in [NiFe] hydrogenase maturation. In *J Biol Chem* 277 (51), pp. 49945–49951. DOI: 10.1074/jbc.M204601200.
- Petkun, Svetlana; Shi, Rong; Li, Yunge; Asinas, Abdalin; Munger, Christine; Zhang, Linhua et al. (2011): Structure of hydrogenase maturation protein HypF with reaction intermediates shows two active sites. In *Structure* 19 (12), pp. 1773–1783. DOI: 10.1016/j.str.2011.09.023.
- Pickwell, G. V.; Barham, E. G.; Wilton, J. W. (1964): Carbon monoxide production by a Bathypelagic Siphonophore. In *Science* 144 (3620), pp. 860–862. DOI: 10.1126/science.144.3620.860.
- Pierik, Antonio J.; Roseboom, Winfried; Happe, Randolph P.; Bagley, Kimberly A.; Albracht, Simon P. J. (1999): Carbon monoxide and cyanide as intrinsic ligands to iron in the active site of [NiFe]-hydrogenases. NiFe(CN)₂CO, biology's way to activate H₂. In *J. Biol. Chem.* 274 (6), pp. 3331–3337. DOI: 10.1074/jbc.274.6.3331.
- Preissler, Janina (2018a): Funktion, Modifikation und Anwendung von O₂-toleranten, NAD(P)⁺-reduzierenden [NiFe]-Hydrogenasen. Ph.D. Thesis. Technische Universität Berlin, Berlin.
- Preissler, Janina; Wahlefeld, Stefan; Lorent, Christian; Teutloff, Christian; Horch, Marius; Lauterbach, Lars et al. (2018b): Enzymatic and spectroscopic properties of a thermostable [NiFe]-hydrogenase performing H₂-driven NAD⁺-reduction in the presence of O₂. In *BBA - Bioenerg* 1859 (1), pp. 8–18. DOI: 10.1016/j.bbabi.2017.09.006.
- Rangarajan, Erumbi S.; Asinas, Abdalin; Proteau, Ariane; Munger, Christine; Baardsnes, Jason; Iannuzzi, Pietro et al. (2008): Structure of [NiFe] hydrogenase maturation protein HypE from *Escherichia coli* and its interaction with HypF. In *J Bacteriol* 190 (4), pp. 1447–1458. DOI: 10.1128/JB.01610-07.
- Reissmann, Stefanie; Hochleitner, Elisabeth; Wang, Haofan; Paschos, Athanasios; Lottspeich, Friedrich; Glass, Richard S.; Böck, August (2003): Taming of a poison: biosynthesis of the NiFe-hydrogenase cyanide ligands. In *Science* 299 (5609), pp. 1067–1070. DOI: 10.1126/science.1080972.
- Rey, L.; Fernández, D.; Brito, B.; Hernando, Y.; Palacios, J.-M.; Ruiz-Argüeso, T.; Imperial, J. (1996): The hydrogenase gene cluster of *Rhizobium leguminosarum* bv. *viciae* contains an additional gene (*hypX*), which encodes a protein with sequence similarity to the N₁₀-formyltetrahydrofolate-dependent enzyme family and is required for nickel-dependent hydrogenase processing and activity. In *Molec Gen Genet* 252 (3), pp. 237–248. DOI: 10.1007/BF02173769.

References

- Riplinger, Christoph; Pinski, Peter; Becker, Ute; Valeev, Edward F.; Neese, Frank (2016): Sparse maps—A systematic infrastructure for reduced-scaling electronic structure methods. II. Linear scaling domain based pair natural orbital coupled cluster theory. In *J Chem Phys* 144 (2), p. 24109. DOI: 10.1063/1.4939030.
- Rodríguez-Maciá, Patricia; Galle, Lisa M.; Bjornsson, Ragnar; Lorent, Christian; Zebger, Ingo; Yoda, Yoshitaka et al. (2020): Caught in the H_{inact}: crystal structure and spectroscopy reveal a sulfur bound to the active site of an O₂-stable state of [FeFe] hydrogenase. In *Angewandte Chemie (International ed. in English)*. DOI: 10.1002/anie.202005208.
- Roseboom, Winfried; Blokesch, Melanie; Böck, August; Albracht, Simon P. J. (2005): The biosynthetic routes for carbon monoxide and cyanide in the Ni-Fe active site of hydrogenases are different. In *FEBS Lett* 579 (2), pp. 469–472. DOI: 10.1016/j.febslet.2004.12.013.
- Saggu, M.; Teutloff, C.; Ludwig, M.; Brecht, M.; Pandelia, M. E.; Lenz, O. et al. (2010): Comparison of the membrane-bound [NiFe] hydrogenases from *R. eutropha* H16 and *D. vulgaris* Miyazaki F in the oxidized ready state by pulsed EPR. In *Phys Chem Chem Phys* 12 (9), pp. 2139–2148. DOI: 10.1039/b922236g.
- Saggu, M.; Zebger, Ingo; Ludwig, M.; Lenz, O.; Friedrich, Bärbel; Hildebrandt, P.; Lenzian, F. (2009): Spectroscopic insights into the oxygen-tolerant membrane-associated [NiFe] hydrogenase of *Ralstonia eutropha* H16. In *J Biol Chem* 284 (24), pp. 16264–16276. DOI: 10.1074/jbc.M805690200.
- Sanger, F.; Nicklen, S.; Coulson, A. R. (1977): DNA sequencing with chain-terminating inhibitors. In *Proc Natl Acad Sci USA* 74 (12), pp. 5463–5467. DOI: 10.1073/pnas.74.12.5463.
- Schirch, D.; Villar, E.; Maras, B.; Barra, D.; Schirch, V. (1994): Domain structure and function of 10-formyltetrahydrofolate dehydrogenase. In *J Biol Chem* 269 (40), pp. 24728–24735. Available online at <http://www.jbc.org/content/269/40/24728.full.pdf>.
- Schlegel, H. G.; Kaltwasser, H.; Gottschalk, G. (1961): A submersion method for culture of hydrogen-oxidizing bacteria: growth physiological studies. In *Arch Microbiol* 38, pp. 209–222.
- Schulz, Anne-Christine; Frielingsdorf, Stefan; Pommerening, Phillip; Lauterbach, Lars; Bistoni, Giovanni; Neese, Frank et al. (2020): Formyltetrahydrofolate decarbonylase synthesizes the active site CO ligand of O₂-tolerant [NiFe] hydrogenase. In *J Am Chem Soc* 142 (3), pp. 1457–1464. DOI: 10.1021/jacs.9b11506.
- Schwartz, Edward; Fritsch, Johannes; Friedrich, Bärbel (2013): H₂-metabolizing prokaryotes. In Eugene Rosenberg, Edward F. DeLong, Stephen Lory, Erko Stackebrandt, Fabiano Thompson (Eds.): *The Prokaryotes*: Springer Berlin Heidelberg, pp. 119–199.
- Senger, Moritz; Stripp, Sven T.; Soboh, Basem (2017): Proteolytic cleavage orchestrates cofactor insertion and protein assembly in [NiFe]-hydrogenase biosynthesis. In *J Biol Chem* 292 (28), pp. 11670–11681. DOI: 10.1074/jbc.M117.788125.
- Shepard, Eric M.; Duffus, Benjamin R.; George, Simon J.; McGlynn, Shawn E.; Challand, Martin R.; Swanson, Kevin D. et al. (2010): [FeFe]-hydrogenase maturation: HydG-catalyzed synthesis of carbon monoxide. In *J Am Chem Soc* 132 (27), pp. 9247–9249. DOI: 10.1021/ja1012273.
- Shomura, Y.; Taketa, M.; Nakashima, H.; Tai, H.; Nakagawa, H.; Ikeda, Y. et al. (2017): Structural basis of the redox switches in the NAD⁺-reducing soluble [NiFe]-hydrogenase. In *Science* 357 (6354), pp. 928–932. DOI: 10.1126/science.aan4497.

References

- Shomura, Yasuhito; Higuchi, Yoshiki (2012): Structural basis for the reaction mechanism of S-carbamoylation of HypE by HypF in the maturation of [NiFe]-hydrogenases. In *J. Biol. Chem.* 287 (34), pp. 28409–28419. DOI: 10.1074/jbc.M112.387134.
- Shomura, Yasuhito; Komori, Hirofumi; Miyabe, Natsuko; Tomiyama, Masamitsu; Shibata, Naoki; Higuchi, Yoshiki (2007): Crystal structures of hydrogenase maturation protein HypE in the Apo and ATP-bound forms. In *J Mol Biol* 372 (4), pp. 1045–1054. DOI: 10.1016/j.jmb.2007.07.023.
- Siebert, E.; Horch, M.; Rippers, Y.; Fritsch, Johannes; Frielingsdorf, Stefan; Lenz, O. et al. (2013): Resonance Raman spectroscopy as a tool to monitor the active site of hydrogenases. In *Angew Chem Int Ed* 52 (19), pp. 5162–5165. DOI: 10.1002/anie.201209732.
- Simon, R.; Priefer, U.; Pühler, A. (1983): A broad host range mobilization system for *in vivo* genetic engineering: transposon mutagenesis in gram negative bacteria. In *Nat Biotechnol* 1 (9), pp. 784–791. DOI: 10.1038/nbt1183-784.
- Soboh, Basem; Stripp, Sven T.; Bielak, Claudia; Lindenstrauß, Ute; Braussemann, Mario; Javaid, Mahwish et al. (2013): The [NiFe]-hydrogenase accessory chaperones HypC and HybG of *Escherichia coli* are iron- and carbon dioxide-binding proteins. In *FEBS Lett* 587 (16), pp. 2512–2516. DOI: 10.1016/j.febslet.2013.06.055.
- Soboh, Basem; Stripp, Sven T.; Muhr, Enrico; Granich, Claudia; Braussemann, Mario; Herzberg, Martin et al. (2012): [NiFe]-hydrogenase maturation: isolation of a HypC-HypD complex carrying diatomic CO and CN⁻ ligands. In *FEBS Lett* 586 (21), pp. 3882–3887. DOI: 10.1016/j.febslet.2012.09.019.
- Stephens, P. J.; Devlin, F. J.; Chabalowski, C. F.; Frisch, M. J. (1994): *Ab initio* calculation of vibrational absorption and circular dichroism spectra using density functional force fields. In *J Phys Chem* 98 (45), pp. 11623–11627.
- Stripp, Sven T.; Lindenstrauß, Ute; Granich, Claudia; Sawers, R. Gary; Soboh, Basem (2014): The influence of oxygen on [NiFe]-hydrogenase cofactor biosynthesis and how ligation of carbon monoxide precedes cyanation. In *PloS One* 9 (9), e107488. DOI: 10.1371/journal.pone.0107488.
- Stripp, Sven T.; Lindenstrauß, Ute; Sawers, R. Gary; Soboh, Basem (2015): Identification of an isothiocyanate on the HypEF complex suggests a route for efficient cyanyl-group channeling during [NiFe]-hydrogenase cofactor generation. In *PloS One* 10 (7), e0133118. DOI: 10.1371/journal.pone.0133118.
- Stripp, Sven T.; Soboh, Basem; Lindenstrauß, Ute; Braussemann, Mario; Herzberg, Martin; Nies, Dietrich H. et al. (2013): HypD is the scaffold protein for Fe-(CN)₂CO cofactor assembly in [NiFe]-hydrogenase maturation. In *Biochemistry* 52 (19), pp. 3289–3296. DOI: 10.1021/bi400302v.
- Szöri-Dorogházi, E.; Maróti, G.; Szöri, M.; Nyilasi, A.; Rakhély, G.; Kovács, K. L. (2012): Analyses of the large subunit histidine-rich motif expose an alternative proton transfer pathway in [NiFe] hydrogenases. In *PloS One* 7 (4), pp. e34666. DOI: 10.1371/journal.pone.0034666.
- Tai, Hulin; Nishikawa, Koji; Higuchi, Yoshiki; Mao, Zong-wan; Hirota, Shun (2019): Cysteine SH and glutamate COOH contributions to [NiFe] hydrogenase proton transfer revealed by highly sensitive FTIR spectroscopy. In *Angew. Chem.* 131 (38), pp. 13419–13424. DOI: 10.1002/ange.201904472.
- Tamagnini, Paula; Axelsson, Rikard; Lindberg, Pia; Oxelfelt, Fredrik; Wunschiers, Robbe; Lindblad, Peter (2002): Hydrogenases and hydrogen metabolism of cyanobacteria. In *Microbiol Mol Biol Rev* 66 (1), 1-20, table of contents. DOI: 10.1128/mmbr.66.1.1-20.2002.

References

- Tamagnini, Paula; Leitão, Elsa; Oliveira, Paulo; Ferreira, Daniela; Pinto, Filipe; Harris, David James et al. (2007): Cyanobacterial hydrogenases: diversity, regulation and applications. In *FEMS Microbiol Rev* 31 (6), pp. 692–720. DOI: 10.1111/j.1574-6976.2007.00085.x.
- Teixeira, Vitor H.; Soares, Cláudio M.; Baptista, António M. (2008): Proton pathways in a [NiFe]-hydrogenase: A theoretical study. In *Proteins: Struct, Funct, Bioinf* 70 (3), pp. 1010–1022. DOI: 10.1002/prot.21588.
- Thauer, Rudolf K.; Kaster, Anne-Kristin; Goenrich, Meike; Schick, Michael; Hiromoto, Takeshi; Shima, Seigo (2010): Hydrogenases from methanogenic archaea, nickel, a novel cofactor, and H₂ storage. In *Annu Rev Biochem* 79, pp. 507–536. DOI: 10.1146/annurev.biochem.030508.152103.
- Thiemermann, S.; Dervedde, J.; Bernhard, M.; Schroeder, W.; Massanz, C.; Friedrich, B. (1996): Carboxyl-terminal processing of the cytoplasmic NAD-reducing hydrogenase of *Alcaligenes eutrophus* requires the *hoxW* gene product. In *J Bacteriol* 178 (8), pp. 2368–2374.
- Todorovic, Smilja; Teixeira, Miguel (2018): Resonance Raman spectroscopy of Fe-S proteins and their redox properties. In *J Biol Inorg Chem* 23 (4), pp. 647–661. DOI: 10.1007/s00775-018-1533-0.
- van der Linden, Eddy; Burgdorf, Tanja; Lacey, Antonio L. De; Buhrke, Thorsten; Scholte, Marcel; Fernandez, Victor M. et al. (2006): An improved purification procedure for the soluble [NiFe]-hydrogenase of *Ralstonia eutropha*: new insights into its (in)stability and spectroscopic properties. In *Journal of biological inorganic chemistry : JBIC : a publication of the Society of Biological Inorganic Chemistry* 11 (2), pp. 247–260. DOI: 10.1007/s00775-005-0075-4.
- Vignais, P. M.; Billoud, B. (2007): Occurrence, classification, and biological function of hydrogenases. an overview. In *Chem Rev* 107 (10), pp. 4206–4272. DOI: 10.1021/cr050196r.
- Vignais, P. M.; Billoud, B.; Meyer, J. (2001): Classification and phylogeny of hydrogenases. In *FEMS Microbiol Rev* 25 (4), pp. 455–501. DOI: 10.1111/j.1574-6976.2001.tb00587.x.
- Volbeda, Anne; Garcin, Elsa; Piras, Claudine; Lacey, Antonio L. De; Fernandez, Victor M.; Hatchikian, E. Claude et al. (1996): Structure of the [NiFe] hydrogenase active site: evidence for biologically uncommon Fe ligands. In *J Am Chem Soc* 118 (51), pp. 12989–12996. DOI: 10.1021/ja962270g.
- Watanabe, Satoshi; Matsumi, Rie; Arai, Takayuki; Atomi, Haruyuki; Imanaka, Tadayuki; Miki, Kunio (2007): Crystal structures of [NiFe] hydrogenase maturation proteins HypC, HypD, and HypE: insights into cyanation reaction by thiol redox signaling. In *Mol Cell* 27 (1), pp. 29–40. DOI: 10.1016/j.molcel.2007.05.039.
- Watanabe, Satoshi; Matsumi, Rie; Atomi, Haruyuki; Imanaka, Tadayuki; Miki, Kunio (2012a): Crystal structures of the HypCD complex and the HypCDE ternary complex: transient intermediate complexes during [NiFe] hydrogenase maturation. In *Structure* 20 (12), pp. 2124–2137. DOI: 10.1016/j.str.2012.09.018.
- Watanabe, Satoshi; Sasaki, Daisuke; Tominaga, Taiga; Miki, Kunio (2012b): Structural basis of [NiFe] hydrogenase maturation by Hyp proteins. In *Biol Chem* 393 (10), pp. 1089–1100. DOI: 10.1515/hsz-2012-0197.
- Wittenberg, Jonathan B. (1960): The source of carbon monoxide in the float of the Portuguese man-of-war, *Physalia physalis* L. In *J Exp Biol* 37 (4), pp. 698–705.
- Wray, J. W.; Abeles, R. H. (1993): A bacterial enzyme that catalyzes formation of carbon monoxide. In *J Biol Chem* 268 (29), pp. 21466–21469.

References

Xavier, Joana C.; Preiner, Martina; Martin, William F. (2018): Something special about CO-dependent CO₂ fixation. In *FEBS J* 285 (22), pp. 4181–4195. DOI: 10.1111/febs.14664.

Yanisch-Perron, Celeste; Vieira, Jeffrey; Messing, Joachim (1985): Improved M13 phage cloning vectors and host strains: nucleotide sequences of the M13mpl8 and pUC19 vectors. In *Gene* 33 (1), pp. 103–119. DOI: 10.1016/0378-1119(85)90120-9.

Zorin, Nikolay A.; Zabelin, Alexey A.; Shkuropatov, Anatoly Ya; Tsygankov, Anatoly A. (2017): Interaction of HydSL hydrogenase from *Thiocapsa roseopersicina* with cyanide leads to destruction of iron-sulfur clusters. In *J Inorg Biochem* 177, pp. 190–197. DOI: 10.1016/j.jinorgbio.2017.09.016.

6. Table of Tables

Table 1. Bacterial strains used in this study.	29
Table 2. Plasmids used in this study.	30
Table 3. Oligonucleotides used in this study.....	32
Table 4. Mineral salts medium for cultivation of <i>R. eutropha</i>	34
Table 5. Antibiotics used for cultivation.	34
Table 6. Composition of the assembly master mix for Gibson assembly.	38
Table 7. Composition of a denaturing SDS gel.....	44
Table 8. Antibodies used in this study	46
Table 9. H ₂ -oxidation activities of HtSH variants carrying exchanges for Glu32 in the large subunit HoxH.....	62
Table 10. Metal determination via ICP-OES of apo- and holo-HypCD _{strep}	69
Table 11. Metal determination via ICP-OES of Fe-reconstituted (Fe) apo- and holo-HypCD _{strep}	73
Table 12. CN stretching frequencies of KCN-treated HypCD and controls.	77
Table 13. ATPase activities of HypE and HypF measured with the PK-LDH assay.	83
Table 14. Metal content of purified MBP-HypX determined via ICP-OES.	88
Table 15. K_M and k_{cat} values for N^{10} -formyl-THF and Formyl-CoA	90
Table 16. Specific and relative activity of native MBP-HypX and different HypX variants with N^{10} -formyl-THF and formyl-CoA as substrate.....	95
Table 17. Specific activity and k_{cat}^{app} of MBP-HtHypX and Strep-HtHypX.....	97
Table 18. Specific and relative activities of Strep-HtHypX.....	101

7. Table of Figures

Figure 1. Schematic representation of the active sites of [NiFe]-, [FeFe]- and [Fe]-hydrogenase.	9
Figure 2. Catalytic cycle of [NiFe]-hydrogenases.	13
Figure 3. Subunit and cofactor composition of <i>HtSH</i>	16
Figure 4. IR spectra of <i>HtSH</i> recorded under different redox conditions.	17
Figure 5. Structure of the NiFe active site of <i>HtSH</i>	18
Figure 6. Model of the assembly of the NiFe(CN) ₂ (CO) active site in [NiFe]-hydrogenases under aerobic conditions.	20
Figure 7. Model of the Fe binding site of HypCD.	22
Figure 8. CN ⁻ ligand synthesis catalyzed by HypF and HypE.	24
Figure 9. Proposed cyanation mechanism in the HypCDE complex.	25
Figure 10. SDS gel of <i>HtSH</i> purified via size-exclusion chromatography.	56
Figure 11. Aerobic oxidation of reduced <i>HtSH</i> over time.	58
Figure 12. SDS-PAGE gel of purified <i>HtSH</i> variants E32D, E32A and E32Q.	59
Figure 13. IR spectra of native <i>HtSH</i> (red) and <i>HtSH</i> variants E32D (blue), E32A (green) and E32Q (grey).	60
Figure 14. H ₂ -oxidation activity of Glu32 variants.	61
Figure 15. SDS-PAGE analysis and immunological detection of apo-HypCD and holo-HypCD purified from aerobically or anaerobically grown recombinant <i>E. coli</i> cells harboring plasmids pThypDCstrep or pThypDEFCstrep.	64
Figure 16. IR spectra of apo-HypCD (red spectrum), holo-HypCD (grey spectrum) and holo-HypCD treated with NaDT (blue spectrum).	65
Figure 17. UV-Vis spectra of holo- and apo-HypCD _{strep}	66
Figure 18. Size-exclusion chromatography of apo-HypCD _{strep}	68
Figure 19. Resonance Raman spectra of holo- and apo-HypCD.	70
Figure 20. ATPase activity of different HypCD _{strep} preparations.	72
Figure 21. Treatment of apo-HypCD(Fe) with CO gas.	74
Figure 22. Treatment of apo-HypCD(Fe) with KCN.	76
Figure 23. Reconstitution of apo-HypCD _{strep} with a synthetic Fe(CN) ₂ (CO) moiety mimic.	79
Figure 24. SDS-PAGE gel of HypF and HypE.	80

Table of Figures

Figure 25. Coupled assay of HypF and HypE to test the ATP-dependent dehydration reaction of HypE.....	81
Figure 26. ATPase activity of HypE and HypF measured with the PK-LDH assay.	82
Figure 27. Transfer assay of the Fe(CN) ₂ (CO) moiety from holo-HypCD _{His} to apo-HoxG.	85
Figure 28. MBP-HypX is functional in vivo.....	87
Figure 29. Purification of MBP-HypX visualized on an SDS-PAGE gel.	88
Figure 30. HypX-dependent CO formation in vitro.....	89
Figure 31. Determination of the K_M value for N^{10} -formyl-THF.	90
Figure 32. CoA stabilizes HypX.	91
Figure 33. Determination of the K_M value for formyl-CoA.....	92
Figure 34. Inhibition of formyl-CoA-dependent CO release by free CoA.	93
Figure 35. Sequence alignment and structure of the C-terminal Co-A binding region in HypX.....	94
Figure 36. SDS-PAGE gel and CO-releasing activity of purified MBP-HypX variants Y439F, S448A and E449Q.	95
Figure 37. SDS-PAGE gel of purified MBP- <i>Ht</i> HypX and Strep- <i>Ht</i> HypX.	97
Figure 38. Determination of the Strep- <i>Ht</i> HypX K_M value for N^{10} -formyl-THF.	98
Figure 39. Purified MBP- <i>Ht</i> HypX incubated with factor Xa.	100
Figure 40. Strep- <i>Ht</i> HypX-dependent CO formation.....	101
Figure 41. Temperature dependence of the CO-releasing activity of Strep- <i>Ht</i> HypX.	102
Figure 42. Size-exclusion chromatography (SEC) of Strep- <i>Ht</i> HypX.....	104
Figure 43. SDS-PAGE gel and immunological detection of purified Strep- <i>Ht</i> HypX.....	105
Figure 44. Proposed protection mechanism against irreversible oxidative inactivation of <i>Ht</i> SH.	110
Figure 45. Proposed two-step reaction mechanism catalyzed by HypX.....	117

8. Appendix

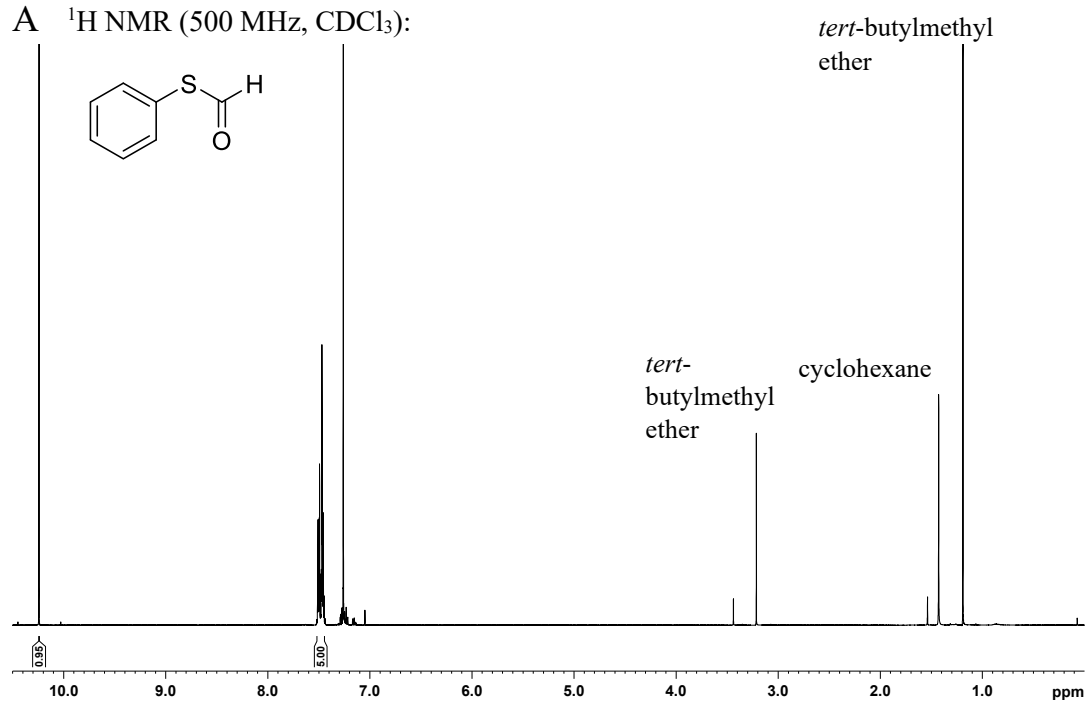
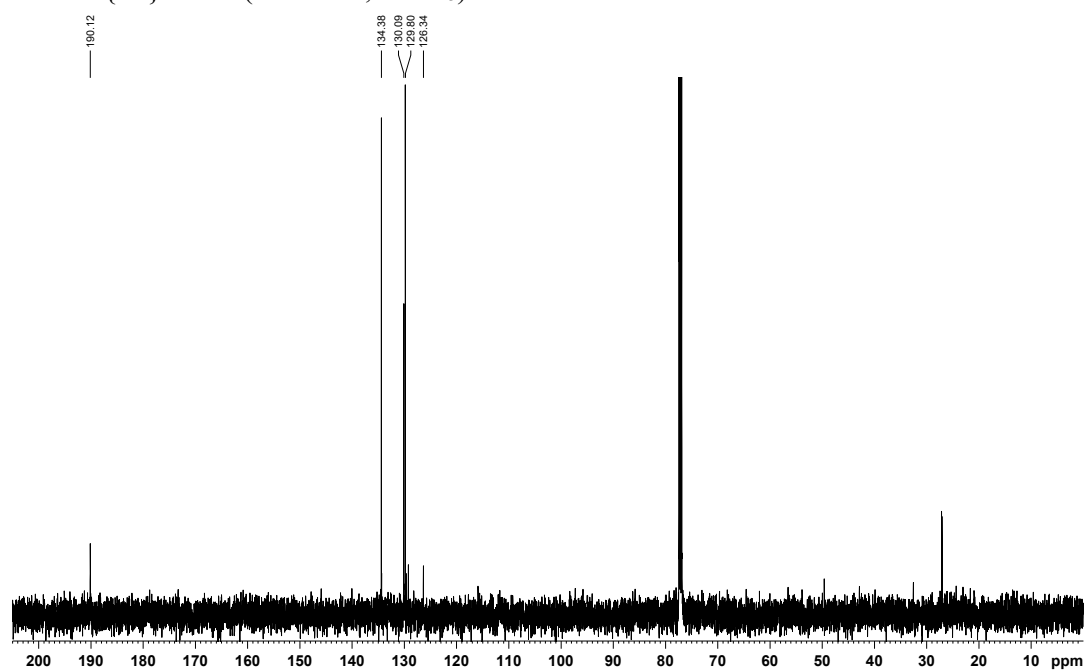
S-Phenyl methanethioateA ^1H NMR (500 MHz, CDCl_3):B $^{13}\text{C}\{^1\text{H}\}$ NMR (126 MHz, CDCl_3):

Figure A1. ^1H NMR and $^{13}\text{C}\{^1\text{H}\}$ spectra of *S*-phenyl methanethioate. (A) ^1H NMR (500 MHz, CDCl_3) spectrum of *S*-phenyl methanethioate. (B) $^{13}\text{C}\{^1\text{H}\}$ NMR (126 MHz, CDCl_3) spectrum of *S*-phenyl methanethioate.

Formyl-Coenzyme A

^1H NMR (700 MHz, D_2O):

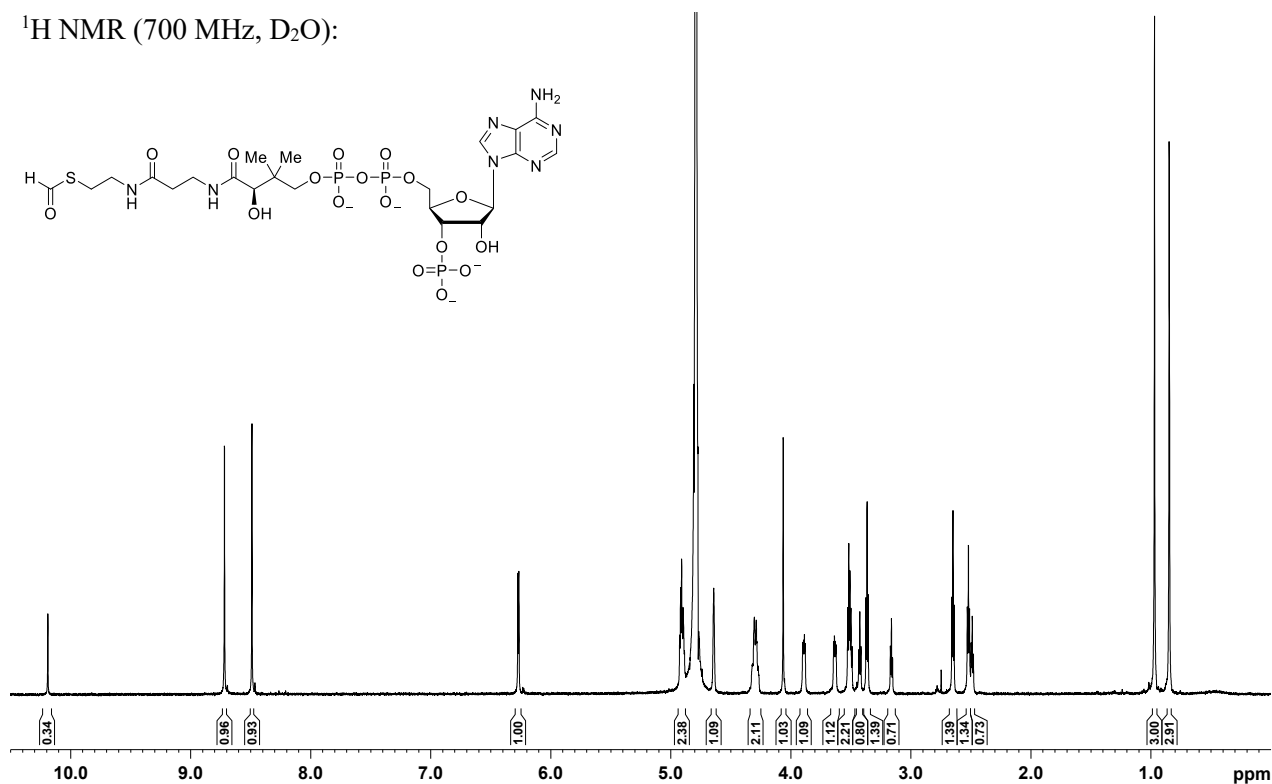


Figure A2. ^1H NMR (700 MHz, D_2O) spectra of formyl-CoA. Product formation is evidenced by the proton signal of the formyl group at $\delta/\text{ppm} = 10.19$.